Electron Transport in Hall Thrusters

by

Michael Sean McDonald

A dissertation submitted in partial fulfillment
of the requirements for the degree of
Doctor of Philosophy
(Applied Physics)
in The University of Michigan
2012

Doctoral Committee:

Professor Alec D. Gallimore, Chair
Professor John E. Foster
Professor Yue Y. Lau
Richard R. Hofer, Jet Propulsion Laboratory

For Carolyn, who kept me sane on the journey

ACKNOWLEDGEMENTS

In 1924, Louis De Broglie published his 127-page doctoral dissertation, *Researches on the Quantum Theory.* His committee, puzzled by the work, passed it on to Albert Einstein, whose praise enabled Louis to make his friends call him Dr. Louis at the bar that evening. Five years later, in 1929, he would receive the Nobel Prize in Physics for that work, forever setting the bar much too high for graduate students following in his stead.

A more humble fate awaits this work, but even so I couldn't have approached these past five years without a great deal of assistance. Research doesn't just happen in a vacuum, even when it *does* happens in a vacuum... chamber. And a really, really big vacuum chamber at that.

First and foremost thanks go to my advisor, Alec Gallimore. Over the past twenty years Alec has assembled a remarkable facility manned by some truly outstanding scientists and engineers, and I have been privileged to work here among them. Nowhere else could I have done work of the same quality and scale as I have laid down in these pages. Alec has created a fertile ground where his students can do great, relevant science, and amazingly they can do it for the most part without worrying about how much it costs.

I owe a tremendous debt to my predecessors, who inherited the unenviable job of teaching me everything I know about Hall thrusters, plasma, machining, plumbing, circuitry, the art of the "kludge" and all the other dirty, grimy bits of research that

you only learn from doing. I barely knew how to turn a wrench when I stepped into PEPL five years ago; today I'm a passably competent experimentalist and I've even dabbled in modeling. I wouldn't have gotten far without the help of now Drs. Bryan Reid, Robert Lobbia, Tom Liu, Kristina Lemmer and Dan Brown. You don't know the joys of research until you've seen Bryan's antics during a successful test. Robbie taught me about op-amps, stray capacitance, and all the other arcanum in the black art of time-resolved measurements, and hosted some really great movie nights along the way. Tom is the single most productive (and yet still overworked) person I know, and a constant inspiration when I feel overwhelmed. I just ask myself, WWTLD? (What Would Tom Liu Do?) I'm sorry to say Kristina taught me my most important lesson: when you mess up a colleague's experiment, any worthwhile apology must involve beer. Also, beware of tripping circuit breakers unless you know *everything* on that circuit. Dan and I didn't get to work together much, but he holds the distinction of being the first person to cite me in a conference paper, back when I was a wet-behind-the-ears third year, and also the first to buy me a drink at a conference. His insights on low-voltage thruster operation inspired my inquiry into spoke impacts on thruster efficiency in this work.

To my contemporaries, Drs. Rohit Shastry and David Huang, with whom I shared a special bond that only forms when three theses focus on the same piece of hardware (a 6-kW thruster whose name we only now dare speak), I can only apologize for all the times my laboratory cleanliness fell short of your high bar. I like to think I kept you on your toes. Rohit taught me more about sheaths than I ever wanted to know, while David convinced me I really, really don't have the patience to work with lasers. Long live Rosheng.

To those still around a little while longer, including Ray Liang, Adam Shabshelowitz, Roland Florenz and Laura Spencer, good luck and enjoy it. Ray's borderline pathological attention to detail in his craftsmanship, as well as his overall organization and thoroughness, is inspiring. Like David, Adam has shown me another experimental arena I dare not enter, the field of RF plasmas. If David showed me lasers require the patience of a stone, Adam has me half-convinced that RF matching networks require blood sacrifice. Roland has taught me so many colorful new phrases in other languages I hardly know where to begin, phrases usually inspired by his Herculean (Sisyphean?) struggles designing the world's biggest Hall thruster, and if I refrain from printing them here it is only for fear of offending the sensibilities of anyone passingly familiar with Italian, Russian, Chinese, or a host of other tongues. Laura has given countless demonstrations of the melting point and other useful properties of quartz, and in the process extended my admiration for those who work in RF plasmas to include microwave plasmas as well, and to be thankful that those brave souls have left the comparatively simple DC Hall thruster to lesser lights like myself. She is also a wizard of baked goods, and we are all grateful to be guinea pigs for her culinary (though not microwave) experiments.

Finally to the new arrivals: Chris Durot, Kim Trent, Mike Sekerak and Chris Bellant – I hope you all come to realize, if you don't already, how lucky you are to be working here, and what a magical place it is. Make the most of it. Perspective will be hard to maintain late at night, when you can't find anything in our entropy-rich toolboxes, or your probes break / the motion tables seize up / your lines lose continuity and the only thing keeping thoughts of arson at bay is the sure knowledge LVTF would survive unscathed. These moments will come, but it's still an amazing thing to step back and contemplate the freedom you will be given to solve important problems as you see fit. One of Alec's great strengths is finding significant problems for his students to work on, picking students who are capable of doing them, and having the patience to let them do it. I look forward to seeing what you all discover.

The quality of this document owes a great deal to my committee, possibly the only individuals who will ever read this work in its entirety. It is easy to lose sight of the forest for the trees while writing a dissertation, and I appreciate their welcome perspective and insightful comments. Any flaws remaining are entirely my own. Particular thanks go to Dr. Richard Hofer of the Jet Propulsion Laboratory, one of our alumni who has often shared his wisdom and experience over the past few years, and who was integral in supporting ongoing investigations of rotating spokes and electron transport in Ray's X2 Hall thruster. Rich has more than once waded through my fumbles at electron modeling to separate the gold from the dross, and if what remains is often still only a tantalizing shimmer of dust instead of a gleaming nugget, the fault is entirely my own and any credit is shared.

The electric propulsion community is a small one, but to a person I have found my colleagues at other institutions to be unfailingly helpful in reaching this point. In particular, Dr. Dan Goebel of Jet Propulsion Laboratory has taught me almost everything I know about cathodes, and guided me through my own successful effort to build one myself. It is a humbling experience to ask Dan a question, only to realize he has not only already considered the issue in depth but that he has usually already published a paper on it – before you were born. Dr. Andrew Smith, whose work on electron trajectory modeling inspired my own, has been gracious in helping me to understand his work as I have followed in his footsteps. While we have achieved different results I suspect that may be as much due to our different thrusters as anything, especially given our still-hazy understanding of the electron transport picture as a whole. The thoroughness of his work is at a very high level that I hope to reach myself. Dr. Yevgeny Raitses and his students Jeff Parker and Lee Ellison have been investigating rotating spokes for about as long as I have, and for much of that period we were mutually ignorant of one another's efforts. It is a testament to their good character that in spite of our unfortunate, uncoordinated presentation of near-identical results from a segmented anode in consecutive time slots at a conference, we have since had an excellent relationship with fruitful discussion on the nature of rotating spokes in Hall thrusters. To these and to all those who have shared e-mails, discussions at conferences, or offered feedback on my work, thank you.

That covers the professional side of my life the past few years, which is to say, the less important side. To my wife Carolyn, thank you a thousand times. I wouldn't have finished this thesis or this five-year adventure in discovering "how to do research" without your support and, more importantly, your patience. You were the reason I stayed in Ann Arbor for graduate school, and it was the best decision I've ever made. Set beside that the work of the rest of these pages is just a happy afterthought. Thank you, and for the record, now that the thesis is done my excuse for not doing the dishes has officially run out. Not a moment too soon.

Michael McDonald

Ann Arbor, MI

January 2012

TABLE OF CONTENTS

CHAPTER

LIST OF FIGURES

Figure

LIST OF TABLES

Table

LIST OF APPENDICES

Appendix

CHAPTER I

Introduction

"Earth is the cradle of humanity, but one cannot live in the cradle forever."

Konstantin Tsiolkovsky, 1909

1.1 Scope

The Hall thruster today is a mature space flight technology in the 1600-3000 second specific impulse range, with peak flight power levels demonstrated at 4.5 kW to date on the BPT-4000 and ground units tested with nominal power levels up to 50 kW.[1,9] Over 200 thrusters have flown in space since 1971, performing a variety of missions from north-south satellite stationkeeping to LEO-GEO orbit raising. However, despite this high level of maturity and long flight heritage, computer models of the device remain dependent on empirical inputs and a large part of thruster development to date has been heavily experimental in nature. This empirical approach will become increasingly unsustainable in the coming years as high-power thrusters tax existing ground test facilities and more exotic thruster designs stretch and strain the boundaries of existing design experience.

The fundamental obstacle preventing predictive modeling of Hall thruster plasma properties and channel erosion is the lack of a first-principles description of electron transport across the strong magnetic fields between the cathode and anode. It is no exaggeration to say that electron dynamics in the Hall thruster plume affect nearly every aspect of thruster operation: the ease of electron transport across magnetic field lines sets equipotentials that guide ion acceleration and focusing, determining beam divergence and affecting channel erosion patterns; the extent to which they heat or cool during transport alters ionization and excitation cross-sections and influences propellant utilization efficiencies; and the ease with which the cathode electrons couple into the plume and set the cathode potential relative to the far-field plasma potential (the so-called cathode coupling voltage) determines the maximum attainable ion acceleration voltage, driving the largest part of losses in the voltage utilization efficiency. So long as Hall thruster models are governed by *ad hoc* transport coefficients derived more from empirical data matching than *a priori* physical principles, there can be no truly predictive Hall thruster model. At present, in spite of an abundance of proposed mechanisms, accurate assessments of the magnitude of electron current due to any one mechanism are scarce, and comparative studies of their relative influence on a single thruster platform simply do not exist. Lacking a clear idea of what mechanism(s) are primarily responsible for transport, it is understandably difficult for the electric propulsion scientist to focus their theoretical and computational tools on the right targets.

This work presents a primarily experimental investigation of Hall thruster electron transport mechanisms, supported where appropriate by electron trajectory simulations, in an attempt to provide a comparative study of different classes of electron transport mechanisms. This work also attempts to address the lack outlined above and to offer guidance to future modeling and experimental efforts.

1.2 Organization

Chapter 2 delves into the specific operating principles of Hall thrusters and in particular explores the current state of the electron transport problem. Chapter 3 describes the experimental equipment used in this work, including the H6 Hall thruster testbed. Chapter 4 examines collisional transport mechanisms in the plume through the development of an electron trajectory model tracking electrons from their birth at the centrally mounted cathode. Chapter 5 is devoted to investigations of a particular form of plasma turbulence called a rotating spoke instability by high-speed camera and through the construction of an azimuthally segmented anode for the H6. Chapter 6 presents the conclusions of this work, namely that it has not been possible to demonstrate near-field collisional transport in the electron model but that the rotating spoke instability conclusively carries cross-field electron current in the channel and is a promising candidate for near-field investigation in future work.

1.3 The rocket equation

Rocket propulsion is the most common form of space propulsion, applying Newton's third law of action and equal, opposite reaction for navigation by the directed expulsion of onboard propellant mass.[1] In 1897 Russian rocketry pioneer Konstantin Tsiolkovsky derived the fundamental relationship between rocket mass, propellant and payload capability; published in 1903, *The Exploration of Cosmic Space by Means of Reaction Devices* laid out what is now known as the Tsiolkovsky rocket equation, or simply *the* rocket equation. The rocket equation forms the basis for the motivation for the study of electric propulsion, and is worth examination here to lay

---

[1] Other techniques are possible but less widespread, including propellantless propulsion technologies like solar and magnetic sails, or electromagnetic tethers taking advantage of the Lorentz force on a current-carrying line moving through Earth's magnetic field.

that groundwork.

1.3.1 Derivation and Interpretation

Tsiolkovsky's rocket equation expresses the maximum payload mass a device can accelerate to a desired final velocity by reaction against an expelled propellant stream. It is purely a consequence of the conservation of linear momentum. Consider a rocket of mass m, which expels an infinitely small unit of fuel dm at an exhaust velocity v_e. Conservation of momentum requires that the spacecraft experience a small change in velocity dv, such that

$$m\,dv = dm\,v_e \tag{1.1}$$

As the rocket expends fuel m decreases, and the same expulsion of propellant dm at velocity v_e produces an ever larger dv. The exhaust velocity v_e is typically considered a constant, fixed property of the propellant. This equation is separable and integrable, and setting appropriate bounds in mass and velocity yields

$$\int_{m_0}^{m_f} \frac{dm}{m} = \frac{1}{v_e} \int_{v_i}^{v_f} dv$$

$$\frac{m_f}{m_i} = e^{-\frac{(v_f - v_i)}{v_e}} \tag{1.2}$$

where m_i and m_f are the initial (wet) and final (dry) masses of the rocket, and v_i and v_e are the initial and final velocities. Physically, the left hand side of the equation is the upper limit to the payload ratio, the amount of useful mass that can fit on the rocket compared to the generally much larger propellant mass. The inverse exponent on the right hand side means that to achieve a reasonable payload fraction, say on the order of 10%, the exhaust velocity of the propellant needs to be of about the same order of magnitude as the velocity increment $\Delta v \equiv v_f - v_i$ for the mission. This exponential behavior reflects that a higher Δv requires more propellant, raising the total mass slightly and so requiring yet another smaller addition of propellant, and so on *ad infinitum.*

For a variety of reasons the exhaust velocity is often specified in terms of the specific impulse I_{sp} defined as

$$I_{sp} \equiv \frac{\int_0^t F dt}{g \int_0^t \dot{m} dt}$$

where F is the rocket thrust force, $\dot{m}$ is the mass flow rate, g is the gravitational acceleration 9.81 m/s^2 and the I_{sp} has units of seconds.[2] For the case of a constant mass flow rate $\dot{m}$ the thrust is also constant as $F = \dot{m} v_e$, where v_e is the exhaust velocity as above, and the specific impulse simplifies to $I_{sp} = v_e/g$. The rocket equation is then recast as

$$\frac{m_f}{m_i} = e^{-\frac{\Delta v}{g\, I_{sp}}} \tag{1.3}$$

The I_{sp} is an efficiency measure for a propellant, with higher values being better. Physically, the specific impulse represents how long an infinitesimal amount of propellant dm can accelerate an equal amount of mass at the gravitational acceleration g; practically, it is a performance metric that applies whether you work in pounds or kilograms.

---

[2] A “specific impulse” might properly be thought of as an impulse per unit mass, but as defined it is in fact an impulse per unit weight, specifically the weight at the surface of the earth where $g =$ 9.81 m/s^2. If this seems strange, consider the convenience of the result: dividing by the gravitational acceleration makes it immaterial whether thrust is measured in SI or Imperial units – the I_{sp} is always in seconds. Defining the I_{sp} in this manner also gives more easily understood values, often in the low hundreds of seconds for chemical rockets. The German rocket community in the 1930s used the inverse of the specific impulse as a performance metric with units of 1/seconds, producing inconvenient values like .0056 s^{-1} or similar.[13]

The derivation of the rocket equation makes no assumptions about the nature of the propellant acceleration, making it equally applicable to either chemical or electric propulsion systems. As a result, the rocket equation and the specific impulse make a useful lens to compare the two technologies.

1.3.2 Propellant chemistry and limits on the specific impulse

Chemical propulsion uses combustion to liberate energy stored in chemical bonds and accelerate the resulting hot gases through a nozzle, converting chemical energy to kinetic energy and creating thrust. The ideal chemical propellant has an extremely high energy density, but is at the same time stable and safe to handle. These two requirements conflict, and in practice the increased risk of ever higher energy density propellants to suddenly and unpredictably release that energy (e.g., explode) places an upper limit on the achievable specific impulse in real chemical systems. Hydrazine, a good rocket monopropellant, has a specific impulse of 220 seconds; hydrazine variants such as monomethylhydrazine (MMH) are used as fuels with nitrogen tetroxide (N_2O_4) as an oxidizer in bipropellant systems such as the Space Shuttle Orbital Maneuvering System, with a specific impulse of 313 seconds.

Tsiolkovsky calculated that liquid hydrogen and liquid oxygen (two relatively new substances at the turn of the century) were a nearly ideal bipropellant combination, and indeed these would later power the space shuttle main engine (SSME). The SSME is, or rather was, an excellent example of the extreme upper performance limits of a chemical rocket system, with a specific impulse at vacuum of about 450 seconds or an exhaust velocity of about 4.5 km/s. For comparison, the Δv to reach earth orbit is on the order of 10 km/s, and to reach one of the outer planets such as Jupiter is about 50 km/s. Chemical systems relatively routinely access low-earth orbit (LEO) and even geosynchronous orbit (GEO), but for missions to other planets or for some particularly demanding earth-orbit missions of long duration, for example satellite stationkeeping, or of medium duration at moderate thrust, such as orbit-raising, higher specific impulse options are far more well-suited.

1.4 The Case for Electric Propulsion

Electric propulsion systems decouple propellant chemistry from performance by using electrical power for propellant acceleration. Jahn conceptually divided electric propulsion into three families: electrothermal, electrostatic and electromagnetic propulsion.[2] Briefly, electrothermal systems use electrical power to heat a working fluid to high temperature, either through a resistive wire (resistojets) or directly through an arc (arcjets), before accelerating the hot gases through a nozzle. Electromagnetic systems such as the magnetoplasmadynamic (MPD) thruster use the interaction of a current in a plasma with the applied magnetic field to create thrust through the Lorentz $j \times B$ force.

The third family of electric propulsion device is the electrostatic accelerator, including gridded ion and Hall thrusters. In both thrusters an inert gas propellant, typically xenon or krypton, is ionized through inelastic electron collisions and accelerated through an electric field. In the gridded ion thruster the electric field is formed between two closely spaced perforated grids, while in Hall thrusters the electric field is maintained without grids through the action of the applied magnetic field on the plasma.

The H6 Hall thruster examined in this dissertation has a nominal operating power level of 6 kW, with a thrust of 397 mN and an anode specific impulse of 2000 s.[16] At some operating conditions the thruster approaches 3000 seconds of specific impulse.

To give an example of the benefits of high specific impulse, to transport a single kilogram of payload to Jupiter ($\Delta v \sim 40$ km/s) on a very high-performance chemical rocket system like the space shuttle main engine ($I_{sp} = 450$ s) would require about 5000 kilograms of propellant. To accomplish the same mission with a high specific impulse Hall thruster ($I_{sp} = 3000$ s) would require a little less than four kilograms of propellant. Still, while EP makes appreciable payload fractions possible even for high Δv, it is not a panacea. There are still limits, mainly due to available electrical power.

1.4.1 Power as a constraint on an electric rocket

Electric propulsion effectively trades constraints on the energy density of propellants for constraints on the specific power of onboard electric sources. These constraints are more amenable to technological advances – the price per watt of solar panels has dropped by a factor of 6 since 1980 from \$22/W to less than \$4/W, for instance[11] – but they limit the types of missions suitable for electric propulsion.

In an electric propulsion device, the fundamental design constraint is the available electrical power for propellant acceleration. Consider the kinetic energy of a mass of propellant in the exhaust stream, given by the usual expression ${}^1\!/\!{}_2 m v_e^2$ where as before v_e is the exhaust velocity. The power P associated with maintaining this exhaust stream is the time derivative of the kinetic energy imparted to the exhaust, often called the jet power:

$$P = {}^1\!/\!{}_2 \dot{m} v_e^2 \tag{1.4}$$

where $\dot{m}$ is shorthand for the mass flow rate of the rocket dm/dt and the constant exhaust velocity is unaffected by the differentiation. From Newton's first law, the thrust force T of the rocket is the time rate of change of the momentum p. Taking the right hand side of Eqn. 1.1 as dp,

$$T = \frac{dp}{dt} = \dot{m} v_e \tag{1.5}$$

Recalling the simplified expression for the specific impulse $I_{sp} = {}^{v_e}/_{g}$, it is apparent that the power, thrust and specific impulse of an electric propulsion system are related as

$$P \propto T \, I_{sp} \tag{1.6}$$

Thus, for the typical case of fixed electrical power aboard a spacecraft, there is a potential tradeoff between thrust and specific impulse. Given a power level, the thruster can in theory be operated for high thrust or high specific impulse at will. In practice modern Hall thrusters often operate at different conditions along a throttling table designed to trade off between these quantities, but at either extreme the thruster efficiency begins to suffer.

Returning to an advanced chemical system, the vacuum thrust and specific impulse of a single SSME (the shuttle had three) are 2.1 kN and 450 s, for a jet power of approximately 4.6 gigawatts (GW). While the specific impulse of the Hall thruster is several times that of the shuttle, the nearly six orders of magnitude difference in power level between the systems relegates the H6 and all electric propulsion systems of the foreseeable future to very small thrust levels. Electrical power on the chemical scale simply cannot fly, not when the largest utility scale power generation facilities on Earth barely break into the gigawatts. The Hoover Dam on the Colorado River has an installed power generation capacity of 2.1 GW, and the largest nuclear reactors in the world only reach about 1.5 GW each. For the few brief minutes when

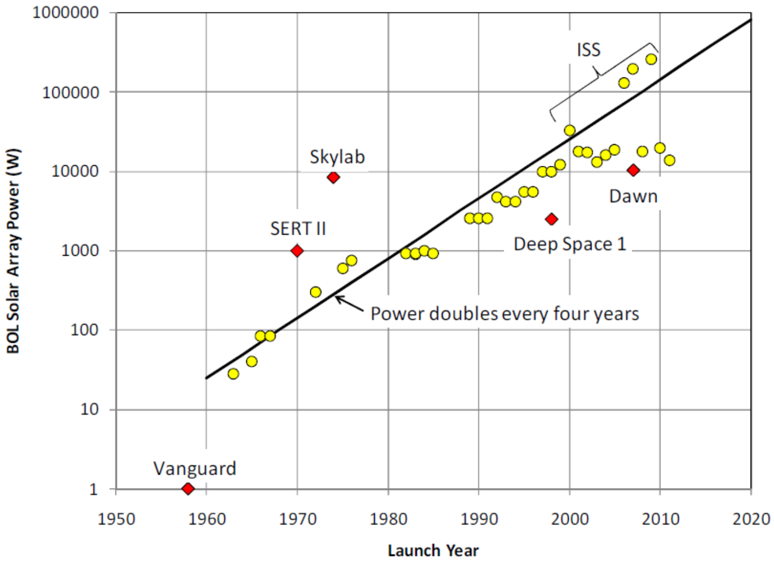

Figure 1.1. Solar power availability on space missions over the last half-century, demonstrating a doubling of available power approximately every four years.

the space shuttle launched, it became the most powerful object on earth; the H6 is matched by five dozen 100 W light bulbs.

1.5 Upward trends in thruster power and cost

While power levels for electric propulsion are small, they are rising. The main source for space power continues to be solar, though nuclear reactors have been proposed and continue to be a part of some design studies.[10] Advances in solar panel technology over recent decades have led to a Moore's law-type exponential growth trajectory in spaceborne solar power generation capability, first described by Brophy, with power levels doubling about every four years since 1970 (Figure 1.1).[6] "Brophy's Law" predicts onboard power levels to reach 1 MW by 2020.

Following the increased availability of onboard power, Hall thruster design power levels are also rising. The first Hall thruster to fly in space, a Fakel SPT-60 in 1971, had a power level of about 300 W. By the mid-1990s, the SPT-100 had demonstrated a power level of 1.35 kW in space, and in 2010 the Aerojet BPT-4000 launched with a design power level of 4.5 kW. In the Hall thruster field the definition of a "high-power" laboratory model thruster tends by observation to track approximately with the peak power level demonstrated in space. For example, in the 1990s any Hall thruster in excess of 1 kW could credibly have been called high-power; today it is unlikely that any thruster not in the 5-10 kW range could credibly claim the title.

In the next decade laboratory model thruster designs on the order of 100 kW are likely to become far more commonplace. Already several designs of 20 kW or greater have been reported, including the NASA 300M,[7] 400M[3] and 457M[3,12], the Busek BHT-20K[15] and others. Above around 50 kW trade studies suggest that nested Hall thrusters come into their own[14]; a sub-power technology demonstrator dual nested Hall thruster with a 10 kW design level called the X2 has already been built and tested at the University of Michigan,[5] with a 80-kW class triple nested Hall thruster currently under development.[14]

1.5.1 Voltage and Current as control knobs in electric propulsion

In electrical terms high power might apply equally to high voltage or high current, but in Hall thrusters it generally refers to high-current operation. Hall thrusters typically operate at a specific impulse (I_{sp}) in the 1000-3000 second range, corresponding to exhaust velocities in the tens of kilometers per second. This is an applicable range for the Δv of most missions of interest in the solar system (see Fig. **??**) and in particular the common operation in the mid 1000-second range has been shown to be near optimum for pairing with chemical launch systems for orbit raising, based on the relation to typical chemical launch system I_{sp} values and other efficiency factors.[17] By conservation of energy, a singly charged ion of mass m_i falling through a voltage drop V will attain velocity v given by

$$v = \sqrt{\frac{2eV}{m_i}} \tag{1.7}$$

which for a xenon atom translates to a theoretical relation between specific impulse and voltage for a perfectly efficient thruster

$$I_{sp} = 123\sqrt{V}\,[sec] \tag{1.8}$$

Assuming reasonable voltage utilization on the order of 80-90%, the 1000-3000 second desirable specific impulse range for Hall thrusters above corresponds to a desirable voltage range between 100-800 V. Even taking the upper extreme of this voltage range, anticipated power levels on the order of 100 kW correspond to over 100 A; in fact, common design voltages in Hall thrusters tend to be more like 300 V, and the current in these devices will be correspondingly higher.

The drive for increased power in Hall thrusters then is really a drive for increased current to raise thrust levels. From Eqn. 1.5, thrust can be increased with either increased mass flow or increased exhaust velocity. Each unit of mass can only be accelerated by charging it first, so increased mass flow for thrust varies linearly with current. On the other hand, velocity only goes as the square root of voltage, so while doubling power via current actually doubles thrust, doubling power via voltage only increases thrust by a factor of $\sqrt{2}$. This is also the motivation for using heavy gases like xenon or krypton (or, recently, even iodine[18]) for Hall thruster propellants – heavier atoms equate to more mass flow for the same discharge current.

1.5.2 Financial constraints on testing at high power

Cost of Hall thruster testing may be divided into facility costs, personnel costs, and propellant costs. The largest of these costs may be either the facility cost or the propellant cost, depending on thruster power level and the prevailing price of xenon.

Xenon propellant is expensive due to its scarcity in the atmosphere, only occurring naturally at about one part in 10 million. A typical price in 2011 is on the order of \$5/L, where 1 L of xenon at standard temperature and pressure corresponds to a mass of about 6 grams. At this rate the nominal mass flowrate of 20 mg/s on the H6 thruster costs about \$60/hr. For the X3 triple NHT discussed by Florenz[14], anticipated flowrates will reach in excess of 100 mg/s or \$300/hr. While these costs are not insurmountable, they have already started to form a significant enough part of thruster testing budgets to make xenon recovery systems cost-effective. The volatility of xenon pricing can also be a factor in testing schedules; as recently as 2009 the price of xenon spiked tenfold to near \$50/L.

Facility costs are appreciable since Hall thrusters are space propulsion devices and experimental work must take place in vacuum chambers to simulate the space environment. In particular, since thrust is intimately linked to mass flow and current, vacuum chambers for high power thruster testing require extremely high pumping speeds. Randolph outlined a criterion that background pressure in test facilities begins to affect thruster operation at about 10^{-5} Torr,[8] and vacuum facilities capable of maintaining this level of high vacuum in the face of mass flowrates in the range of 10 - 100 mg/s become increasingly rare.

One such facility is NASA's Tank 5 at Glenn Research Center, which costs about \$15000/week to rent for external, i.e., non-NASA, use as of 2009.[4] The rental cost for the Large Vacuum Test Facility (see Section 3.1) at the University of Michigan for external use is comparable. These facility costs can roughly be divided into overhead, support personnel, and consumables. Overhead and personnel, while non-negligible, are not a strong function of thruster power level, but the consumables are.

The two main consumables (excepting xenon, which has already been discussed) for Hall thruster testing are liquid nitrogen and electricity. Liquid nitrogen (LN2) cools cryopumps to maintain the chambers at high vacuum; the LVTF consumes about 1000 L / day of liquid nitrogen at a unit cost of about \$ 0.10-0.20 / L for a cost of a few hundred dollars per day. With higher power thrusters comes an increased heat load on the cryosurfaces and a greater need for cooling. The LN2 cost can be reduced with well-insulated supply lines and, in some cases, by closed-cycle systems at the cost of high installation costs, but already the pressure of higher power thrusters on existing facilities is motivating the development of new cryopumping technology.

The main electrical power draws are the thruster itself and the cryopumping equipment. By conservation of energy the cryopumping power must at least equal the discharge power, less radiative cooling of the hot chamber under ion bombardment. In fact the cryopumping power may be a multiple of the discharge power. The LVTF is cooled by 7 cryopumps drawing about 5 kW each for maximum cryopump power load of 35 kW. This level of cryopumping is sufficient to maintain the H6 thruster under nominal 300 V, 20 mg/s operation at a 10^{-5} Torr vacuum, corrected for xenon. Approximating 1 mg/s xenon $\approx$ 1 A discharge current, this corresponds to 35 kW of cryocooling to keep a 6 kW thruster at vacuum or a factor of 6 between thruster power and cryopumping power. Leaving room for improvement in cryopumping efficiency by assuming a factor of 3, a 100 kW Hall thruster may be estimated to require another 300 kW of cooling to operate at vacuum. Given an electricity cost of \$0.12 per kilowatt-hour, the electrical cost of testing such a thruster is \$50/hr or about \$1000 / day.

[1] de Grys, K., Mathers, A., Welander, B., and Khayms, V., "Demonstration of 10,400 Hours of Operation on 4.5 kW Qualification Model Hall Thruster," AIAA 2010-6698, Nashville, TN, July 2010.

[2] Jahn, R. G., *Physics of electric propulsion*, Dover Publications, Inc., May 2006.

[3] Jacobson, D., Manzella, D., Hofer, R., and Peterson, P., "NASA's 2004 Hall Thruster Program," July 2004.

[4] Sommerville, J., *Hall-Effect Thruster-Cathode Coupling*, Ph.D. thesis, Michigan Technological University, Houghton, MI, 2009.

[5] Liang, R. and Gallimore, A., "Far-Field Plume Measurements of a Nested-Channel Hall-Effect Thruster," *49th AIAA Aerospace Sciences Meeting*, AIAA-2011-1016, Jan. 2011.

[6] Brophy, J., Gershman, R., Strange, N., Landau, D., Merrill, R., and Kerslake, T., "300-kW Solar Electric Propulsion System Configuration for Human Exploration of Near-Earth Asteroids," July 2011.

[7] Kamhawi, H., Haag, T., Jacobson, D., and Manzella, D., "Performance Evaluation of the NASA-300M 20 kW Hall Thruster," July 2011.

[8] Randolph, T., Kim, V., Kaufman, H. R., Kozubsky, K. N., Zhurin, V. V., and Day, M., "Facility Effects on Stationary Plasma Thruster Testing," *23rd International Electric Propulsion Conference*, IEPC-1993-93, Seattle, WA, 1993.

[9] Manzella, D., Jankovsky, R., and Hofer, R., "Laboratory Model 50 kW Hall Thruster," July 2002.

[10] Donahue, B., "Solar Electric and Nuclear Thermal Propulsion Architectures for Human Mars Missions Beginning in 2033," July 2010.

[11] (NREL), N. R. E. L., "2008 Solar Technologies Market Report: January 2010," Tech. Rep. NREL Report TP-6A2-46025; DOE/GO-102010-2867, 2010.

[12] Jankovsky, R., Jacobson, D., Sarmiento, C., Pinero, L., Manzella, D., Hofer, R., and Peterson, P., "NASA's Hall Thruster Program 2002," July 2002.

[13] Clark, J. D., *Ignition!: An informal history of liquid rocket propellants*, Rutgers University Press, 1972.

[14] Florenz, R. F. and Gallimore, A. D., "Developmental Status of a 100-kW Class Laboratory Nested channel Hall Thruster," *32nd International Electric Propulsion Conference*, IEPC-2011-246, Wiesbaden, Germany, 2011.

[15] Szabo, J., Pote, B., Hruby, V., Byrne, L., Tadrake, R., Kolencik, G., Kamhawi, H., and Haag, T., "A Commercial One Newton Hall Effect Thruster for High Power In-Space Missions," July 2011.

[16] Reid, B., *The Influence of Neutral Flow Rate in the Operation of Hall Thrusters*, Ph.D. thesis, University of Michigan, Ann Arbor, MI, 2009.

[17] Oh, D., Randolph, T., Kimbrel, S., and Martinez-Sanchez, M., "End-to-End Optimization of Chemical-Electric Orbit-Raising Missions," *Journal of Spacecraft and Rockets*, Vol. 41, No. 5, 2004, pp. 831–839.

[18] Szabo, J., Pote, B., Paintal, S., Robin, M., Kolencik, G., Hillier, A., Branam, R., and Huffman, R., "Performance Evaluation of an Iodine Vapor Hall Thruster," July 2011.

CHAPTER II

The Electron Transport Problem

"...the yeoman's work in any science, and especially physics, is done by the experimentalist, who must keep the theoreticians honest."

Michio Kaku

"Electrons are like cockroaches. They get everywhere."

Alec Gallimore

The detailed physical mechanisms of cross-field electron transport in Hall thrusters and many other plasma devices remain poorly understood and as a result difficult to predictively model. Lacking an analytical description of this transport, Hall thruster models often turn to experimental data for model inputs to supply what theory cannot in order to produce accurate results. Obtaining this data results can be expensive and time-consuming, slowing thruster design evolution. This chapter explains the basic operating principles of the Hall thruster, describes the current state of the electron transport problem, and points out the features of the problem that motivate the work in this dissertation.

The theory of classical transport and the phenomenon of Bohm mobility are explained in Section 2.2. Bohm mobility is an empirically derived expression for electron transport that is valid for many plasmas given appropriate experimentally derived coefficients, and is often used to model anomalous transport mechanisms. Section 2.3 describes the two main classes of anomalous transport mechanisms, collisional and turbulent transport. Section 2.4 outlines the most common methods of Hall thruster modeling, hybrid-PIC (particle-in-cell) and kinetic or full PIC, in particular noting how experimental results are incorporated into hybrid-PIC models through the Bohm mobility framework. This section also touches on a third modeling technique, the direct simulation of individual electron trajectories through experimentally measured fields. This technique is not intended to supplant or replace the others as a predictive tool, but it is useful for investigating the plausibility of different transport mechanisms in the experimentally measured regions of the thruster plasma. This technique is applied to the H6 Hall thruster in Chapter IV. Finally, Section 2.5 reviews the evidence from Hall parameter measurements and modeling calculations that the thruster near field, i.e., the region within 1-2 characteristic thruster lengths downstream of the exit plane, is the critical region where the largest amount of anomalous transport must be invoked in current models to reproduce experimental results. This chapter closes by discussing how this state of affairs motivates the near-field plume modeling of Chapter IV and the investigation of low-frequency turbulent transport mechanisms in Chapter V.

2.1 Hall Thruster Operating Principles

The Hall thruster is a type of electric propulsion device using electric and magnetic fields to accelerate ions and produce thrust. The thruster has four basic components: anode, cathode, discharge channel and magnetic circuit (see Figure 2.1). In a typical thruster the cathode supplies electrons to the bulk of the thruster plasma in an annular discharge chamber, where crossed electric and magnetic fields induce a strong azimuthal drift known as the Hall current. The anode rests at the rear of the discharge chamber where it doubles as the neutral propellant gas distributor.

Arguably the most important part of the Hall thruster is the magnetic circuit, since it is the principal influence on the electron dynamics in the thruster discharge. The circuit is composed of inner and outer solenoids with iron cores and connected by iron poles. Screens are also often used outside the discharge channel to prevent strong magnetic fields from extending into the rear of the channel. These components are generally designed in finite element simulation software and the radial magnetic field profile is shaped to peak near the exit plane of the discharge channel. The electric field is strongest at the region of peak magnetic field, where the axial electron mobility is most strongly suppressed. This is thus also the region of the fastest $\mathbf{E}\times\mathbf{B}$ drift, creating the eponymous Hall current. Inelastic collisions between Hall current electrons and neutral propellant atoms create ions which, too massive to be caught in the magnetic field, accelerate through the electric field reaching speeds of tens of kilometers per second.

This explanation, and the purposefully simplified diagrams of Figure 2.1, are only first approximations to the far more complex time-varying processes that take place inside the Hall thruster. In particular, the detailed function of the thruster depends critically on the manner in which electrons travel from the cathode to the anode; it is this complicated and poorly understood process that forms the subject of this dissertation. The Hall thruster depiction in Figure 2.2 by Lobbia, which simply shows the cloud of electrons emitted from the cathode without indicating exactly how they pass into the discharge channel, reflects the ambiguity of this coupling process.

It is clear from measurements of the thruster ion beam current and simple con-

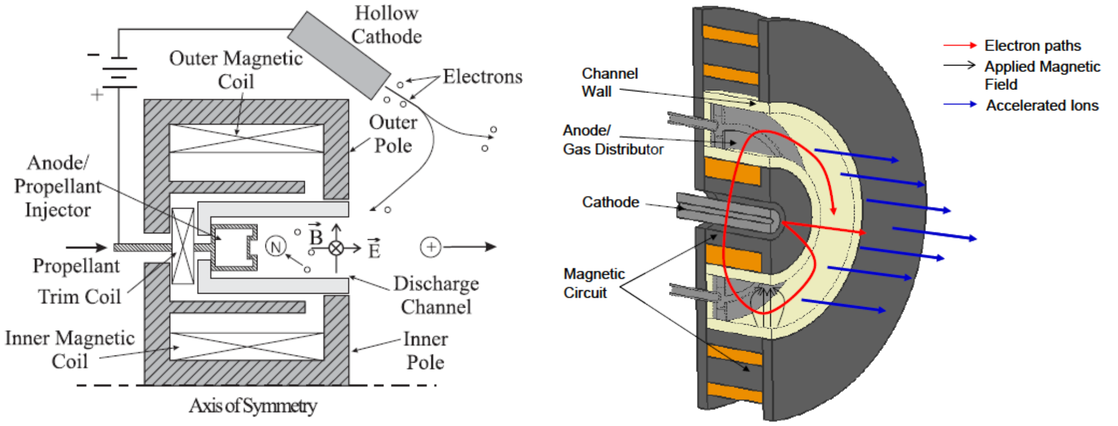

Figure 2.1. Two diagrams of Hall thrusters, from Linnell[35] at left and Shastry[70] at right. Linnell's depiction shows an external cathode angled to send electrons into the thruster channel and into the plume; Shastry's shows an internal cathode also launching electrons smoothly out to the plume and in to an azimuthal drift in the channel. The real electron motion is far more complicated, and in many respects unknown.

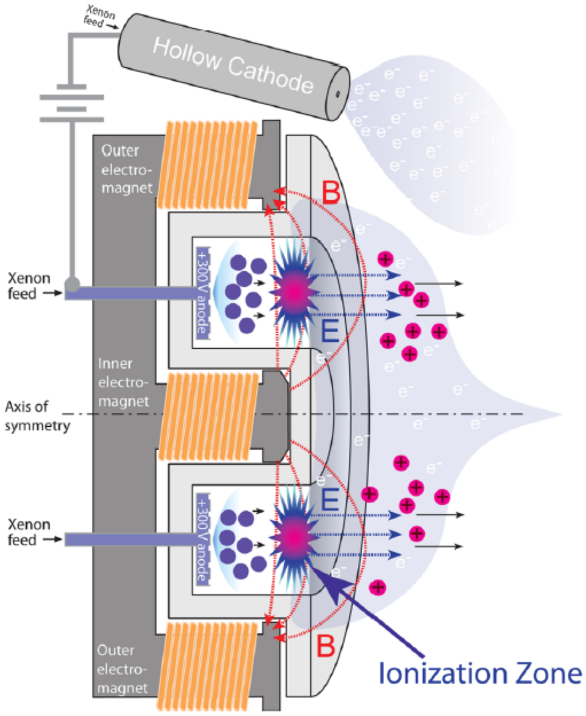

Figure 2.2. Another depiction of a Hall thruster, by Lobbia[66], reflects the current state of understanding of electron transport in the Hall thruster near-field by neglecting to specify an electron path between the cathode and discharge channel.

tinuity arguments that about 80% of the electrons emitted from the cathode depart to the far-field plume to neutralize the ion beam, while about 20% couple back into the channel and sustain the discharge. These 20% of electrons form the largest part of the inefficiency in modern Hall thrusters since they contribute to the discharge current (and thus overall power) but not to the thrust. For a more detailed discussion of Hall thruster efficiency architecture, see Brown.[26] These are the electrons whose anomalous transport across magnetic field lines makes the thruster as a whole so challenging to predictively model.

A naive picture of an ideal Hall thruster might be to imagine a discharge sustained by a single "golden electron" emitted from the cathode toward the anode, triggering an ionization cascade and sustaining the discharge in perpetuity while the remainder of the cathode-born electrons exit to the thruster far field to neutralize the ion beam. Such a configuration would have a current utilization efficiency of unity, but this picture is too simple; the influence of backstreaming electron current on thruster operation is not black and white. To see why, consider an electron emitted in a 300 V discharge in xenon, with an ionization potential of approximately 12 eV. In a best-case scenario if the electron ionized neutrals repeatedly as it fell through the discharge potential, it would have enough energy to create 25 ions expending 12 eV of energy each time before reaching 300 V. If each ionization-born electron did the same, a single electron could produce a large (2^{25} or ~10^{10}), but not infinite, number of electrons to sustain the discharge. Thus, even in principle the golden electron is not enough and some fraction (however small) of cathode-born electrons are continuously required to sustain the discharge.

In practice the fraction is much larger, not the 1 in 2^{25} of this implausible scenario but in fact more like the 1 in 4-5 noted previously. This is because each electron does not create an ion each time it acquires exactly one ionization potential's worth of energy (in fact, the ionization cross-section is about 10 times larger at 30 eV than it is at the 12 eV threshold), some electrons will not produce any ions at all, some electrons lose energy in inelastic excitation collisions with neutrals, some energy is expended in self-heating of the cathode insert through ion bombardment to maintain thermionic emission, some energy is deposited into the anode by electrons arriving with non-zero temperature, some energy is deposited into the insulating walls in the discharge channel, and many other loss mechanisms besides. Nevertheless, there is a fundamental limit on the beam current fraction achievable at a given discharge voltage, and it is important to remember that some amount of backstreaming electron current is required for a thruster to operate. From an efficiency standpoint, it is desirable to make that fraction as small as possible while maintaining discharge stability.

2.1.1 The Need for Predictive Models and Predictive Physics

The Hall thruster of today stands at one end of nearly a half-century of development. The first devices were tested in the United States in the early 1960s,[14,18,19,32,38,49,55,77] and soon after experimental work began in the Soviet Union, where the bulk of thruster development over the next three decades would take place. Hall thruster development has largely been guided by heavily iterative design cycles, but this technique has been successful in bringing the early, relatively inefficient devices of the 1960s and 1960s up to 70% total efficiency[41] with demonstrated ground-based life tests in excess of 10,000 hours and total impulse ratings of several meganewton-seconds (MN-s).[2] Today it is relatively straightforward to design a new Hall thruster of moderate power with greater than 50% efficiency by careful adherence to well-tested rules of thumb, but the experience gained over the past five decades has largely led to a design point for a single channel thruster with a narrow range of exit plane current densities. It is not clear how well this design experience will extend to more esoteric designs such as the nested-channel Hall thruster, where two, three or more channels are packed concentrically and share a magnetic circuit, or whether it is possible to create multi-mode thrusters that can maintain high efficiency across an extended I_{sp} envelope while avoiding excessive thruster self-erosion from high-energy ion bombardment.

The increasing availability of onboard electrical power and corresponding development of higher power Hall thrusters have prompted mission studies for ever more demanding tasks, including cargo transfer to Mars,[10] manned missions to asteroids[20] or even capturing and returning an asteroid to Earth orbit.[31] However, the financial constraints discussed in Section 1.5.2 make heavily iterative thruster design at high power challenging and potentially unsustainable. An ideal alternative and the holy grail of Hall thruster research would be the development of a fully predictive Hall thruster model, a “numerical Hall thruster” like the numerical tokamak in the magnetic confinement fusion community, enabling rapid design iteration and accelerating the overall thruster development process. “Fully” predictive is a misleading term since experimental verification will always be part of the flight thruster development cycle, but an improved predictive capability able to shift the balance of the experimental workload from development to verification could significantly reduce development costs.

The foremost challenge in developing more predictive Hall thruster modeling is an incomplete understanding of the physics of electron transport across the magnetic field. Electrons, due to their small mass, ought to be tightly confined along magnetic (**B**) field lines, even when an electric (**E**) field is applied to drive them across the magnetic field. In the absence of collisions this plays out as a cycloidal path perpendicular to both **E** and **B** known as the $\mathbf{E} \times \mathbf{B}$ drift. In the partially ionized gas of the Hall thruster, collisions with background neutrals reset the phase of the cycloid, permitting incremental cross-field transport with each collision. The resultant motion can be described analytically (see Section 2.2.1) and cross-field electron current due to collisions, the so-called "classical transport", is well-understood. However, classical transport has been known for nearly 50 years to account for $< 1\%$ of experimentally observed cross-field electron currents in Hall thrusters, a deficit still observed today.[11]

Two types of mechanisms are generally proposed to explain anomalous (e.g., non-classical) cross-field electron transport in Hall thrusters: collisional transport via electron impact with thruster surfaces and turbulent transport via fluctuating azimuthal electric fields. Within the thruster channel the first mechanism is known as near-wall conductivity (NWC) and was first studied in the early Russian development of the Hall thruster.[29] More recently direct electron trajectory modeling has suggested that surface collisions in the near-field with the thruster pole pieces also play a role.[58] The Hall thruster plasma has a rich spectrum of characteristic oscillations,[43] and a wealth of different plasma instabilities have been proposed as turbulent transport mechanisms, with frequencies ranging from the few kilohertz up to several megahertz.[7,9,11,13,24,27,34,39,40,42,48,56,63,68,76,80] The proposed mechanisms number far greater than the quantitative assessments of transport due to any particular mechanism, and there is no clear picture of which mechanisms are dominant under which operating conditions.

Without a clear candidate mechanism, most Hall thruster models treat anomalous electron transport by artificially inflating the collision frequency with semi-empirical transport coefficients to match experimental results. As Mikellides notes, "*the variation of [these coefficients] from one thruster simulation to another is not based on first principles, which presents the biggest obstacle in advancing such models to fully predictive design tools for Hall thrusters.*"[46] The dominant electron transport mechanisms may well vary in type and magnitude throughout the plume, but lacking a first principles description the simulation domain has often been divided into regions where the coefficients are assigned different constant values. In recent simulations by Hofer et. al., the largest of these simulation domains is in the near-field plume bridging the cathode to the exit plane, a region whose unexpectedly high electron mobility Hofer describes as *"overlooked in the literature and [deserving of] significantly more scrutiny."*[69]

An ultimate goal of any investigation into electron transport must be to describe the electron transport mechanisms in the near-field region. The present work does not pretend to solve the Hall thruster electron transport problem, but it does represent progress especially through characterization of an omnipresent rotating spoke instability linked to turbulent transport. The electron model developed in Chapter IV focuses on collisional transport mechanisms in the near field, using an electron trajectory modeling technique introduced in Section 2.4.2.2. The main experimental investigation of turbulent transport in Chapter V, dealing with the aforementioned rotating spoke instability, focuses in the near-anode region of the discharge and later presents indirect evidence that the instability extends into the rest of the thruster plume. This initial focus on the anode region where less anomalous transport is required in models is because it is a less harsh environment than the near-field plume and makes possible a "proof of concept" experiment using a segmented anode to link rotating spokes and cross-field electron current. This proof of concept also enables measurement of significant spoke-induced cross-field electron current and motivates the future investigation of this mechanism in greater detail in the near field.

2.2 Classical Transport and Bohm Mobility

The literature on electron transport in Hall thrusters is extensive. The following few sections review classical transport and Bohm mobility. While well understood, classical transport explains only a small part of observed electron transport in the thruster plume. However, the basic mechanism of transport by scattering off of particles is important since it is applied to collisions with neutrals, ions, thruster walls and even "effective collisions" with turbulence under the framework of Bohm mobility. Classical transport is at various times used to refer to only collisions with neutrals and ions, or to include wall collisions as well. Since wall collisions are now calculated analytically in some codes such as HPHall-2, it is becoming more common to consider them as another form of classical transport. In this sense, classical transport may be understood to mean collisional transport that can be well described from first principles. Transport that cannot be explained from first principles is by definition anomalous, and is often dealt with in models using a semi-empirical Bohm mobility.

2.2.1 Classical transport

Diffusion of electrons across a magnetic field due to binary collisions with heavy particles is the original and still most widely used definition of "classical transport", and it can be well-explained analytically. In the absence of the magnetic field, the full charged particle Euler equation of motion in an electric field is:

$$mn\frac{d\mathbf{v}}{dt} = mn\left[\frac{\partial \mathbf{v}}{\partial t} + (\mathbf{v}\cdot\nabla)\,\mathbf{v}\right] = \pm en\mathbf{E} - \nabla p - mn\nu\mathbf{v} \tag{2.1}$$

where the left hand side is the force density, the right hand side are terms for the electric force, the pressure gradient force and the force due to collisions at the collision frequency ν, and the $\pm$ denotes the sign of the particle charge. For a steady-state ($\partial/\partial t = 0$) isothermal ($\nabla T = 0$) plasma where the fluid element is not convected into regions of varied electric field or pressure in the collision period ($\left(\mathbf{v} \cdot \nabla\right) \mathbf{v} \approx 0$), i.e., one where either these quantities are spatially constant or only slowly spatially varying over a distance given by the velocity and collision period, this equation can be solved for the velocity as

$$\mathbf{v} = \pm \frac{e}{m\nu}\mathbf{E} - \frac{k_B T}{m\nu}\frac{\nabla n}{n} \tag{2.2}$$

$$\mu \equiv \frac{|e|}{m\nu} \tag{2.3}$$

$$D \equiv \frac{k_B T}{m\nu} \tag{2.4}$$

$$\mathbf{v} = \pm \mu \mathbf{E} - D\frac{\nabla n}{n} \tag{2.5}$$

where μ is the mobility and D is the coefficient of diffusion. There is considerable variation in the terminology used for anomalous transport in the literature; at times it is referred to as anomalous diffusion, mobility, or even resistivity ρ (where $\mathbf{j} = \mathbf{E}/\rho$). This variation reflects the uncertainty over the cause of anomalous transport in the first place – lacking a clear understanding of the mechanism, any of the terms is equally valid and they are used interchangeably in this thesis.

The classical cross-field mobility is defined in the case of a weakly ionized plasma consisting of charged particles and neutrals in the presence of an electric field and a magnetic field along the z-axis $\mathbf{B} = B\hat{\mathbf{z}}$. Motion parallel to $\mathbf{B}$ is unconstrained and, defining the particle flux $\Gamma_e = n\mathbf{v}$ as the product of velocity and density,

$$\Gamma_{ez} = \pm \mu n E_z - D\frac{\partial n}{\partial z} \tag{2.6}$$

To determine the fluxes perpendicular to the magnetic field, the equation of motion in the perpendicular direction must be considered including the Lorentz force

$$mn\frac{d\mathbf{v}_\perp}{dt} = \pm en(\mathbf{E} + \mathbf{v}_\perp \times \mathbf{B}) - k_B T \nabla n - mn\nu\mathbf{v} = 0 \tag{2.7}$$

This equation is straightforward to solve (see for example Chen[16], p. 171) and yields

$$\mu_\perp = \frac{\mu}{1 + \omega_c^2\tau^2} \tag{2.8}$$

$$D_\perp = \frac{D}{1 + \omega_c^2\tau^2} \tag{2.9}$$

where $\omega_c \equiv eB/m$ is the cyclotron frequency and $\tau \equiv 1/\nu$ is the collision period. Note that the cross-field diffusion and mobility are both reduced by a factor of $1 + \omega_c^2\tau^2$. These are the so-called "classical" transport parameters. The factor $\omega_c\tau$ is well-known in the electric propulsion community as the Hall parameter, and physically can be interpreted as a measure of electron confinement by the magnetic field. Large values of the Hall parameter indicate that many cyclotron orbits occur between collisions, such that the particle can be considered as predominantly confined along magnetic field lines with occasional scattering collisions. Small values of the Hall parameter indicate that the particle experiences many collisions each cyclotron period and scatters easily across the magnetic field.

For large values of the Hall parameter $\omega_c^2\tau^2 \gg 1$ the expressions above reduce to

$$\mu_\perp \approx \frac{\mu}{\omega_c^2\tau^2} = \frac{m\nu}{eB^2} \tag{2.10}$$

$$D_\perp \approx \frac{D}{\omega_c^2\tau^2} = \frac{k_B T m\nu}{e^2B^2} \tag{2.11}$$

The key characteristic to note here is that the classical mobility is proportional to $1/B^2$, a feature that is distinct from the type of mobility generally imposed in Hall thruster models to make these models consistent with experimental results. Such models usually invoke Bohm mobility, discussed in the next section, which goes as $1/B$.

2.2.2 Bohm Diffusion and the link to field fluctuations

In 1946 David Bohm first noted anomalous mobility in a crossed-field device that went as $1/B$ rather than $1/B^2$, in a report on work done during World War II for the Manhattan Project[1] on uranium isotope separation in magnetically confined arcs.[6] Bohm found that the cross-field diffusion in these arcs could be described by a semi-empirical expression

$$D_\perp = \frac{1}{16}\frac{k_B T}{eB} \equiv D_B \tag{2.12}$$

where the factor 1/16 is not rigorously derived and in practice is chosen to fit the results for a particular plasma device. Spitzer later provided a derivation of a $1/B$ form of diffusion valid for cold plasmas ($T_i \ll T_e$) due to electric field fluctuations slow relative to the electron cyclotron frequency and of long wavelength compared

---

[1] Bohm, a student of Oppenheimer's at the Berkeley Radiation Laboratory, had the ill fortune to run afoul of McCarthyism during his doctoral work on the atomic bomb effort. His own papers were classified out from under him and, deemed a security risk, he was denied access to them. Unable to write or defend a thesis, Bohm only received his doctorate by the personal intervention of Oppenheimer, who attested that it was deserved.[79]

to the electron gyroradius.[3] This derivation did not provide an explanation for the formation of such fluctuations; in Spitzer's words, "*We do not consider here how such fluctuations are produced and maintained, or what their properties should be. Instead we treat the much simpler kinematic problem of how such fluctuations can produce diffusion.*" Bohm diffusion has since been observed in many other crossed-field devices including stellarators, magnetrons, homopolar devices and plasma immersion ion implantation systems.[8] Indeed, the classical $1/B^2$ diffusion was not observed in a fully ionized plasma until the 1960s.[16]

Chen provides a simple motivation of the mechanism derived by Spitzer to explain the natural development of $1/B$ mobility in plasmas where electron losses are driven by $\mathbf{E} \times \mathbf{B}$ drifts (Chen[16] p. [193]). In this case the escape flux is:

$$\Gamma_\perp = n v_\perp \propto nE/B$$

If the electric field causing the flux is driven by an oscillation with wavelength long relative the to Debye length, due to Debye shielding the thermal energy will determine the amplitude Φ of potential oscillations as:

$$e\Phi_{max} \approx k_B T_e$$

For a plasma with a characteristic dimension R, the electric field amplitude may be approximated as

$$E_{max} \approx \frac{\Phi_{max}}{R} \approx \frac{k_B T_e}{eR}$$

leading to a flux given by

$$\Gamma_\perp \approx \alpha_B \frac{n}{R}\frac{k_B T_e}{eB} \approx -\alpha_B \frac{k_B T_e}{eB}\nabla n = -D_B \nabla n$$

where α_B is some value $\alpha_B < 1$ chosen to agree with experiment. The original value $\alpha_B = 1/16$ chosen by Bohm turns out to agree with many experiments within a factor of two to three.

2.3 Anomalous Electron Transport Mechanisms

2.3.1 Collisional Transport

Collisional transport follows the same logic as classical transport, and as noted in the previous section may sometimes be included in tallies of classical electron transport for contrast with anomalous transport mechanisms when the transport process can be described analytically. The term generally refers to transport-inducing collisions with the thruster body mediated through the sheath over thruster surfaces, but not to binary plume collisions with heavy thruster particles. In the thruster discharge channel this mechanism is referred to as near-wall conductivity (NWC) and was first proposed by Morozov in the early Soviet development of the stationary plasma thruster (SPT).[29]

Discussions of collisional transport and NWC in the Hall thruster field are often focused exclusively on the discharge channel, while this dissertation is more interested in the evaluation of transport mechanisms in the near-field. However, collisional transport may be relevant in the near-field through electron interactions with the forward surfaces of the thruster outside the discharge channels. These surfaces are formed by the inner and outer front magnetic pole pieces and may be bare iron or spray-coated with an insulating ceramic such as alumina (Al_2O_3) or boron nitride (BN). If spray-coated, the surface is a floating boundary, while if bare metal the surface is conducting and may be electrically grounded, floated, or even biased as in Section 4.4. Modeling by Smith discussed in more detail in Section 2.4.2.2 suggests that channel-bound electrons may bridge the near field to the discharge channel exit plane by bouncing back and forth across the thruster pole pieces due to a combination of magnetic mirror and electrostatic effects until they reach the channel.

2.3.2 Turbulent Transport

Turbulent transport is a collisionless transport mechanism where induced fluctuations in the electromagnetic fields of the Hall thruster plasma create axial $\mathbf{E} \times \mathbf{B}$ drift components, carrying electrons across the applied magnetic field to the anode. Such field fluctuations are commonly attributed to plasma instabilities across a wide range of frequencies, with driving mechanisms including Rayleigh-Taylor or Kelvin-Helmholtz type effects, resonant interaction with characteristic electron or ion oscillations such as the upper or lower hybrid modes, ionization or resistive instabilities, and many others. The form of turbulent cross-field diffusion most commonly considered in the literature is the formation of induced perpendicular $\mathbf{E}$-field components (the azimuthal direction in the cylindrical geometry of the Hall thruster), as for example by Spitzer[3] and Yoshikawa.[1]

A physical picture of turbulent transport begins with the introduction of an azimuthal plasma wave in the thruster, generated by any of the above mechanisms. Such a wave necessarily creates perturbations in the plasma properties, and if the oscillations in the electric field and density are in phase this can drive mobilities that go as $1/B$. This type of mobility is often observed before the turbulent mechanism that drives it is discovered (as in the case of Hall thrusters, where electron transport has been a focus of research for nearly 50 years), and is often referred to as Bohm mobility, discussed in Section 2.2.2.

Turbulent transport in principle can occur at any frequency slow relative to the electron cyclotron frequency, and in a Hall thruster oscillations are present from the low kilohertz up to several megahertz. A comprehensive study of oscillations in Hall thrusters focusing on data taken from the SPT-100 and organized by frequency band was presented by Choueiri.[43] In this discussion of turbulent transport we focus on azimuthal instabilities and also distinguish by frequency. Low frequency oscillations in the kilohertz band are discussed in Section 2.3.2.1, and high frequency oscillations in the megahertz range are covered in Section 2.3.2.2.

2.3.2.1 Low Frequency Azimuthal Instabilities

The first investigation of an azimuthal instability in the Hall thruster was by Janes in 1966.[11] Janes' experiment was on an early laboratory model thruster with a tungsten filament cathode, quartz discharge channel walls and a discharge channel length over ten centimeters. In one of the first demonstrations of the inadequacy of classical electron transport mechanisms to explain observed cross-field current in Hall thrusters, Janes used *in situ* Langmuir probes and floating emissive probes in the discharge channel to demonstrate electron density and plasma potential fluctuations slowly rotating in the $\mathbf{E} \times \mathbf{B}$ direction with sufficient amplitude to account for the experimentally observed anomalous transport in the thruster.

This instability is known as a rotating spoke instability, and has been discussed sporadically in the literature since, but only recently have any investigations been attempted that approach the remarkable thoroughness of this early work. With the cessation of Hall thruster funding in the United States by NASA in 1970, there would be no further domestic studies of this mechanism after Janes' for more than three decades.

In the early 1970s in the Soviet Hall thruster development program Esipchuk further investigated the rotating spoke mechanism in some detail, linking the spoke mode to incomplete ionization and describing its abatement or disappearance at higher power levels.[76] Rotating spokes were found to appear more commonly at low discharge voltages relative to the so-called saturation voltage, which Zhurin describes as the "knee" in a plot of discharge current versus increasing discharge voltage at fixed magnetic field settings.[23]

In the United Kingdom in the late 1970s Lomas linked electron current in a high-current-density hydrogen Hall accelerator intended for controlled fusion work to a rotating spoke or "streamer".[24] Lomas detected the spoke via optical and electrostatic probes, measured an azimuthal electric field fluctuation in phase with a density fluctuation in the spoke, and calculated that 20-70% of the 100 A discharge current was carried by this mechanism. Lomas also extended the electrothermal theory of Nelson[52], which had already been applied to streamer modes in MHD generators, to describe a dispersion relation for two modes, a low-frequency spoke mode and a high-frequency (5 MHz) streamer mode. This bifurcation of the azimuthal instability into low- and high-frequency branches is interesting in light of the present study of rotating spokes at kilohertz frequencies and the recent line of work begun by Adam et. al. dealing with azimuthal waves at megahertz frequencies in kinetic models of Hall thrusters and experimental observation of the same instabilities using collective light scattering techniques.[7,48] However, detailed investigation of the possible implications of the model of Lomas and a connection between azimuthal instabilities in different frequency bands observed in modern Hall thrusters lies outside the scope of the present investigation.

Examination of the spoke mode in the United States resumed in the early 2000s at Stanford University, where Chesta observed several spoke-type instabilities in low-voltage Hall thruster discharges of approximately 80-200 V using azimuthally spaced probes, though he did not conclusively link them to electron transport by measuring the relative phase of density and potential oscillations in the spokes.[54] Chesta's efforts are noteworthy as the first since the work of Lomas to attempt a model of the Hall thruster discharge channel in a 2-D axial-azimuthal (z-θ) formulation, using numerical techniques to solve the dispersion relations and carry out stability analyses on the resulting modes.[56] Like the earlier work of Janes and Lomas, Chesta ultimately attributed the spoke formation to electrothermal processes such as ionization, though the detailed mechanisms of this formation were left and still remain unclear. Later work at Stanford by Meezan would experimentally characterize an anomalously high electron mobility near the thruster acceleration region and, by association with large plasma fluctuations also measured in that region, make a correlative argument that the plasma fluctuations were linked to the transport.[68] However, this argument extended well beyond the frequency band of rotating spokes, encompassing all density fluctuations measured by Chesta via a Langmuir probe in ion saturation sampled at 800 kHz.

At Princeton University in 2010 Parker detected a spoke instability on high-speed camera in a small low-power cylindrical Hall thruster (CHT). Spokes were found to be only occasionally present in the CHT, and their appearance linked to a drastic decrease in thruster efficiency associated with large increases in backstreaming electron current.[80] Further work at Princeton by Ellison used *in situ* electrostatic probes embedded in the CHT channel to measure density and field fluctuations consistent with axial transport, created a small 4-element segmented anode and estimated approximately half the discharge current passed through a rotating spoke.[65]

Chapter V of this thesis presents the most recent work on spoke investigations in the Hall thruster. In parallel to and independently of the work at Princeton a segmented anode for the H6 Hall thruster was constructed with 12 azimuthal segments to measure electron current deposition associated with the spoke rotation.[33] Discharge current measurements were acquired synchronously with high speed video, and the local discharge current oscillation frequencies on each segment matched the visible spoke rotation frequencies. This experiment concluded that on the order of 50% of the electron current in the near-anode region may be carried by rotating spokes, a result consistent with the work of both Ellison and Lomas. Additional findings from this experiment are discussed in Chapter V.

2.3.2.1.1 Prior examination of critical ionization velocity phenomena

Based on their low velocity, Janes and Lowder characterized rotating spokes as part of a larger category of what may be termed "critical ionization velocity phenomena". The critical ionization velocity was first proposed by Alfvén in 1954, while considering the limits of relative flow velocity between a plasma and neutral gas. According to Alfvén, the plasma should be free to accelerate through the neutral gas until the relative velocity between the species reaches the so-called critical ionization velocity where the kinetic energy of the mobile species reaches the ionization potential of the gas,

$$\frac{1}{2}mv_c^2 = eU_i \tag{2.13}$$

where m is the mass of the gas, U_i is the ionization potential, and v_c is the critical ionization velocity (CIV).[72] The CIV varies mainly as the inverse root of the atomic mass for most plasmas, since the ionization potential is relatively constant across the stable elemental gases at standard temperature and pressure, from a low of about 12.1 eV for xenon to 24.6 eV for helium. For xenon, the CIV is about 4 km/s, while for hydrogen it is about 55 km/s. Once the relative velocity reaches the CIV, any additional energy applied to further accelerate the gas instead drives increased ionization, and the velocity will not increase further until total ionization is reached.

Investigations of CIV phenomena have taken place with some regularity over the years since Alfvén's first proposal on the subject, and reviews of experimental, numerical and analytical examinations may be found from the early 1970s by Danielsson and Sherman, in 1992 by Brenning, and in 2001 by Lai, among others.[21,53,57,74] Experimentally, the CIV is found to hold over a large range of background pressures, discharge currents, and gases. Many of these experiments are performed in homopolar devices, a crossed-field annular geometry similar to a Hall thruster but with an axial magnetic field and radial electric field, resulting in an azimuthal $E \times B$ drift just as in the Hall thruster.

Alfvén notes that a "*theory of this [CIV] phenomenon cannot be based on binary collisions, as an atom colliding with an ion has little chance of being ionized unless the velocity surpasses* v_c *by about a factor of 10. The kinetic energy of the atoms must be transferred to the electrons of the plasma, but a direct transfer by elastic collisions is a much too slow process.*"[28] In a recorded discussion of several prominent plasma physicists included with that paper, it is noted that in experiments in the homopolar device the radial current (recall that the homopolar electric field is radial) is observed in discrete surges, suggesting local clouds or blobs of plasma rotating around the azimuth similar to the rotating spokes seen in Hall thrusters and other crossed-field devices such as MPDs.[45]

Modified two-stream instabilities, lower hybrid instabilities, and more recently general plasma turbulence have been proposed as mechanisms to drive the electron heating that maintains the CIV. As Lai notes, "*How to get sufficient turbulence initially needs to be justified on a case-by-case basis.*" Ultimately, the CIV phenomenon is a general plasma behavior that does not necessarily lend greater insight into the mechanisms of formation or potential means for manipulation of the rotating spoke instability in Hall thrusters. Nevertheless, the wide literature available on this phenomenon may prove fruitful for Hall thruster theorists looking for inspiration, especially considering the small size of the electric propulsion community and its associated body of work.

2.3.2.2 High frequency azimuthal instabilities

The focus on turbulent instabilities in Hall thrusters tends to focus either at low frequencies as described above or else at very high frequencies in the MHz range. This bifurcation dates back at least as far back as Lomas, who experimentally observed and analytically described a high-frequency mode in his Hall accelerator along with the low-frequency spoke, and probably dates back even further in the Russian literature. Over the past decade or so this type of instability has received substantially more attention than the low frequency rotating spoke, especially after the publication of kinetic simulations by Adam that self-consistently developed such an instability.[48]

Experimental investigations of high-frequency instabilities generally use some combination of antennas or high-speed *in situ* probes to characterize the instability, for example the work of Litvak[40] and Lazurenko[13,42,63], and by means of either Fourier analysis or cross-correlation functions are able to convincingly demonstrate the presence of these instabilities in a variety of the regions in the near-field plume and into the channel. In some cases azimuthal arrays of probes can be used to demonstrate rotation of the oscillatory disturbances as well. A new collective light scattering optical diagnostic technique has also been recently used by Adam's research group in a report on the detection of a 4-5 MHz azimuthal wave with millimeter wavelengths in the Hall thruster near-field.[7]

The difficulty at the high frequencies and generally very short wavelengths (often < 1 cm) of these instabilities is to conclusively link the observed oscillation to electron transport. This requires a correlation between the plasma potential and density such that when the fluctuating electric field induces an $\mathbf{E}\times\mathbf{B}$ drift toward the anode, the density is high, and when the field is reversed, the field is low, so on each oscillation more electrons are pushed toward the anode than away from it. Measurement of correlated plasma potential and density measurements at MHz frequencies with spatial resolution sufficient to resolve instabilities of the type predicted would be enormously difficult, and to date no such experiment has been performed. Instead, high-frequency instability studies generally focus on characterization of oscillation magnitude and spatial extent with experiments, while net transport calculations are often performed from a theoretical basis, as for example in the further work of Litvak.[9,34]

2.4 Hall Thruster Electron Modeling Techniques

Prior to the 1990s Hall thruster modeling was more often pursued analytically than numerically. Owing to their near-exclusive development of the technology since 1970, a large part of the early analytical work on governing mechanisms in Hall thrusters was carried out in the former Soviet Union. Most of the analytical studies of this early period are 1D in the axial dimension of the thruster; treatment of the thruster in 2D or 3D did not begin until the rise of numerical simulation in the 1990s. The following is a brief overview of Hall thruster numerical modeling techniques organized according to their treatment of electrons, but while several works are listed as examples this is by no means an exhaustive review.

Broadly the electrons may be simulated either as a fluid or discretely. Fluid electron treatments differ in whether they simulate ions as discrete particles, as in hybrid particle-in-cell (hybrid-PIC) codes, or hydrodynamically as a second fluid. Discrete electron simulation is most commonly encountered in kinetic or full PIC codes, though some recent work has demonstrated the use of large-scale numerical solution of electron trajectory equations using static electromagnetic field inputs from hybrid-PIC models or experimental sources.

2.4.1 Fluid Electron Treatments

The most common Hall thruster simulation technique with fluid electrons is hybrid-PIC, leveraging the difference in mass between electrons and ions to treat the electrons as a continuous fluid, while the ions are treated as discrete particles (or, more commonly, superparticles representing many ions). The first such model of a Hall thruster appears to have been a 2D code in the axial and radial ($z-r$) direction by Komurasaki and Arakawa investigating the effects of magnetic field on ion production and losses to the discharge channel walls.[36] Perhaps the most well-known hybrid-PIC code is Fife's HPHall, also a 2D $z-r$ code that has seen substantial development in the nearly 15 years since it was first published.[22,44,47,69] Strictly speaking HPHall was not fully 2D, since it did not treat the radial direction as an independent coordinate for the electrons. Instead the radial gridlines were mapped to magnetic field streamlines, and the electron fluid was treated using a 1D axial energy equation assuming isothermal electrons on the "radial" magnetic field lines. This is a good approximation in part of the discharge chamber and near-field plume, and HPHall was one of the first modeling efforts to numerically reproduce the dominant Hall thruster "breathing mode" oscillation as a predator-prey cycle in the electron and neutral densities, along with the work of Boeuf.[15,64] However, HPHall's use of a "virtual cathode" at the axial gridline farthest downstream makes it difficult for the code to capture the radial variation in plasma potential in the near-field caused by the presence of a real cathode with its associated local depression in plasma potential, as for example in the H6 where the cathode lies on channel centerline.[78]

Electron mobility (defined in Equation 2.8) is not yet calculated fully from first principles in any fluid electron treatment; the portion of it that can be calculated analytically is only a small part of the whole in most of the plume. The larger part is empirically applied as due to collisional wall transport in the Hall thruster channel (NWC) and/or Bohm diffusion in the near-field plume due to azimuthal waves or turbulence of unknown origin. HPHall calculates NWC analytically and reserves empirical factors for Bohm diffusion, while other hybrid-PIC codes such as those by Koo[12] and Hagelaar[62] use empirical factors to address both mechanisms. In all of these codes it is clear that the classical collisions (e.g., electron-neutral and electron-ion collisions) are insufficient on their own to produce experimentally observed levels of electron mobility, a fact also observed experimentally,[11] so a new effective collision frequency is defined as a vehicle to introduce the anomalous transport mechanisms. In the most general case an effective electron collision frequency $\nu_{e,eff}$ may be given as the sum of contributions due to the frequency of collisions with neutrals and ions (ν_{en} and ν_{ei}), discharge channel walls (ν_{e-wall}), and anomalous Bohm turbulence

(ν_{Bohm}) as:

$$\nu_{e,eff} = \nu_{en} + \nu_{ei} + \nu_{e-wall} + \nu_{Bohm} \tag{2.14}$$

$$\nu_{Bohm} \equiv \frac{\alpha_B}{16}\omega_c \tag{2.15}$$

where α_B is a constant chosen to fit the model results to experimental data, and in some cases ν_{e-wall} is also empirically applied. In the case of

Over time α_B has evolved from a pure constant to vary spatially across the plume. Fife initially used classical neutral collisions and Bohm collisionality alone (no wall effects), with a uniform value $\alpha_B = 0.15$ over the whole simulation domain. Hagelaar[62] and later Koo[12] used a two-region mixed mobility model, with varied strengths of Bohm collisionality in the near-field outside the discharge channel and wall collisions inside the discharge channel. Hofer used three regions of varied Bohm mobility in the updated version of Fife's code HPHall-2, with the three regions corresponding to the near-anode region, the ionization / acceleration zone, and the near-field, prompting his remark that this last region is overlooked in the literature.[69] Recently Mikellides has developed a fully 2D Hall thruster simulation code, Hall2De, using a smoothly varying functional form for $\alpha_B = \alpha_B(z)$ where z is the axial coordinate across the simulation domain.[5,41,46] It should be noted that Hall2De is actually a *fully* fluid code, treating the ions as a fluid as well. However, it fits naturally in this section because the treatment of the electron fluid's collision frequency with an anomalous Bohm term is similar to hybrid codes. With the smoothly variable mobility, a field-aligned mesh designed to mimimize numerical diffusion aIn the thruster plasma the level of electron mobility likely varies not only spatially but temporally throughout the plume, and high-speed diagnostic techniques are now maturing to the point where it may soon be possible to experimentally resolve this temporal variation as well.

Most hybrid-PIC Hall thruster models and all of those described above are $z - r$ models, enabling convenient treatment of wall effects in the discharge channel radial boundary conditions. One unfortunate side-effect of this coordinate choice is that the azimuthal Hall current that lends the thruster its name and is such a critical part of its operation is not an integral part of the model physics.

One exception is the 2D $z - \theta$ hybrid-PIC model of Fernandez.[37] This simulation naturally develops a Hall current in the azimuthal direction, and forms azimuthal instabilities of the type theorized to drive turbulent cross-field transport. The model does not invoke anomalous transport coefficients. While the reproduction of the axial electric field in the model is qualitatively similar to experiment, the discharge current is still low (i.e., anomalous transport is not fully accounted for) but the azimuthal fluctuations do drive a level of transport Fernandez says is comparable to classical transport. Unspecified issues arising from numericla stability of the model, in addition to CPU time constraints, prevented the code from running for more than 1-2 μs in simulation time, or about 2 weeks in CPU run time. In addition to Fernandez, Lomas[24] and Chesta[56] have also examined 2D $z - \theta$ electron fluid simulations, and the kinetic simulations of Adam were also $z - \theta$.[48] The final 2D coordinate combination, $r - \theta$, is not used because lacking the axial coordinate the simulation cannot be applied to investigations fo cross-field axial transport.

2.4.2 Discrete Electron Treatments

One way to circumvent the need for empirical data to calculate anomalous transport coefficients is by using a kinetic or fully PIC treatment. Directly modeling the individual particles can, with sufficient time to run the simulation, allow plasma instabilities to form naturally from particle interactions and create cross-field transport. Another method is to sacrifice the self-consistency of the simulation and accept a set of electromagnetic fields as fixed inputs, then integrate many individual electron trajectories sampled from an initial distribution and analyze their motion. This second method is not a direct path to a predictive model, but it can provide insight into how electrons move in the thruster plasma and establish the plausibility of different transport schemes.

2.4.2.1 Kinetic or Particle-in-Cell Simulations

Kinetic codes directly model both electrons and ions as discrete particles acted on by self-consistent electromagnetic forces. This approach can model a thruster from first principles, but at tremendous computational cost. The mass difference between electrons and ions hinders collisional energy transfer between the species and drives distinct energy levels with $T_e \gg T_i$. As a result, the electron thermal velocities so greatly exceed the ions' that to simulate them individually requires much finer timescales than in hybrid-PIC modeling. However, with advances in computing power over the past decade, kinetic simulations have grown more frequent.

Early kinetic codes relied on clever rescaling of fundamental physical parameters, including reducing the ion/electron mass ratio and altering the permittivity of free space ϵ_0 to sidestep the timescale problem. The first kinetic simulation of a Hall thruster with a true mass ratio was by Adam, et. al. in 2004.[48] This 2D $z-\theta$ simulation code was notable for its reproduction of plausible cross-field electron transport without any anomalous transport coefficients over 100 μsec of simulated time. Adam's results suggested that a high-frequency short-wavelength instability in the discharge channel was responsible for transport. However, that simulation also required a full month of computational time on a quad-core processor, making it difficult to envision this technique used for rapid iteration of Hall thruster design at this time. The rapid improvement in affordable computational power, evidenced both in the increasing core counts and clock speeds of CPUs, and the potential for the use of graphical processing units (GPUs) with thousands of lower speed cores in massively parallel simulations, suggest that this simulation technique may be more feasible in the future.

2.4.2.2 Analytic Integration of Electron Trajectories

Anomalous transport coefficients may also be avoided in a simpler modeling technique by the direct numerical integration of electron trajectories in imposed electric and magnetic fields. The first such code applied to Hall thrusters to the author's knowledge was by Smith, who in 2006 began work on a trajectory integrator for use with the Stanford Hall thruster.[17,58,82] Smith's work used static electric fields from a hybrid-PIC model as fixed inputs and simulated large ensembles of electrons from an energy and spatial distribution to generate bulk measurements in the plume and examine electron drift transport. The main claim of this model was that collisions with thruster surfaces could drive a substantial amount of cross-field current to the discharge channel in the near-field, even in static, time-averaged fields devoid of turbulent transport.

This and other models using prescribed fields are of a qualitatively different character from those discussed previously – they are not self-consistent. The motion of each of the simulated electrons does not affect the overall electric or magnetic field or the motion of any other simulated electron in any way. Thus, the electron simulations are entirely independent and fall into a category known as "embarassingly parallel" in the wider simulation community. One benefit of this approach is that the speed of a simulation run scales readily with the number of available processors. A drawback is that the influence of any fluid phenomenon on the simulation must be captured in the imposed fields to show up in the trajectories, since the individual particles are unable to react to one another. Experimental challenges make time-averaged field measurements much more common than time-resolved measurements, and Smith's simulations use only static time-averaged field configurations. Any fluctuations associated with turbulent transport are ignored and only collisional transport is captured.

Some time-resolved measurements have recently been demonstrated,[4,50,61,67,75] and in the near future such measurements may find their way into trajectory-based turbulent transport simulations. Another option is the analytic introduction of turbulent field fluctuations. In 2007 Perez-Luna developed an approach similar to Smith's, inspired in part by the success of Adam's kinetic treatment of the Hall thruster channel, and again using electric fields generated by a hybrid model.[25,81] While Smith focused on collisional transport with thruster surfaces using static fields, Perez-Luna focused on turbulence. In time-averaged fields the model demonstrated the usual magnetic barrier to cross-field transport, but Perez-Luna imposed a simulated azimuthal wave based on the instability simulated by Adam and observed collisionless cross-field transport at a velocity comparable to experimental estimates. Electron trajectory integration has also been used by Wirz, albeit to characterize the motion of electrons emitted from the discharge cathode in a gridded ion thruster, not a Hall thruster.[71? ?]

The main reason to integrate individual electron trajectories in a Hall thruster is to investigate anomalous transport mechanisms. This makes the use of fields generated from hybrid-PIC codes a potential cause for concern, as these codes generally have anomalous transport coefficients empirically selected to reproduce common discharge parameters like discharge current or thrust, while electron trajectories are dependent on the plasma potential profile. On discharge channel centerline the match between modeled and experimental potential is often quite good, but in the very near-field the region in front of the thruster pole pieces (i.e., radially inside and outside the discharge channel, near the exit plane) may not be well-resolved. The level of anomalous transport is adjusted in order to match the model's predicted discharge current to values measured by experiment, and in the case of discrete axial ranges with constant values for the Bohm coefficient α_B the plasma potential may not be accurately reproduced at points radially distant from the channel, as for example over the thruster pole pieces to the inside and outside of the channel. For example, Figure 2.3 shows a comparison between HPHall-2 simulation outputs (blue) and plasma potential measurements by Jameson[60] in the H6 near field (red). The hump in plasma potential over the channel near z/L_c is clearly visible, but over the poles on either side the HPHall simulation values in blue underestimate the experimental values. This is to be expected over the inner pole, where the very large difference is because HPHall does not explicitly model the internal cathode in the H6, instead treating its farthest axial boundary as a virtual cathode. However, the difference persists over the outer pole, where no cathode is present. This difference is by several volts, and in an electron trajectory simulation would permit lower temperature electrons to penetrate deeper axially toward the poles than possible in experiment.

In short, the fields created from simulations with anomalous transport mechanisms are not necessarily the same as those found in the real thruster everywhere in the plume, in particular over the poles where electron interactions with the thruster

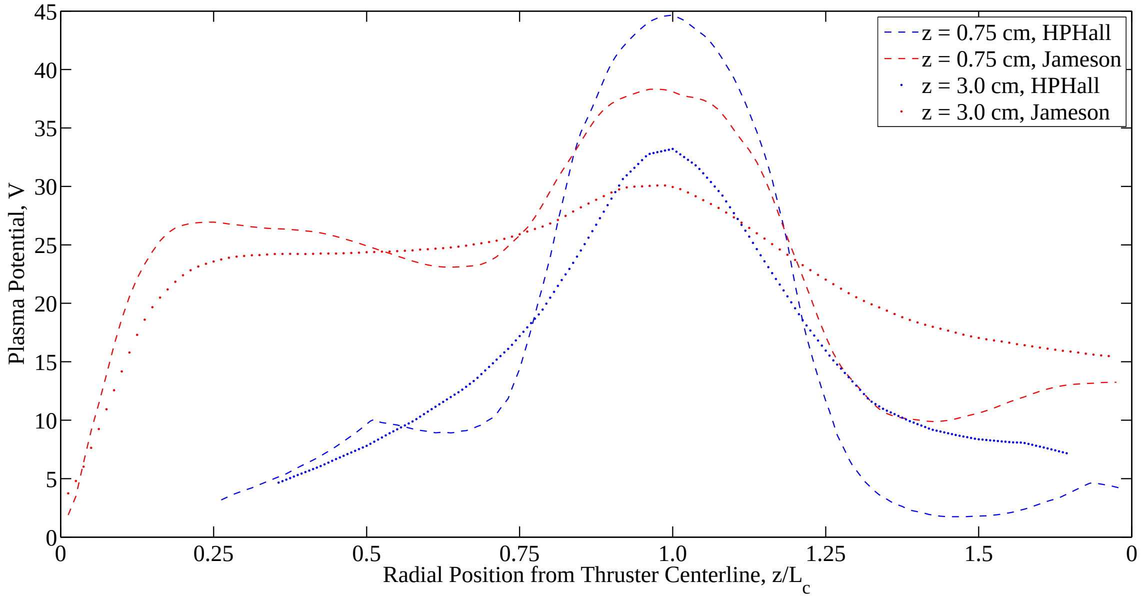

Figure 2.3. Comparison of HPHall-2 hybrid-PIC simulation outputs for plasma potential (blue) with measured plasma potentials in this region by Jameson (red) at nominal H6 300 V, 20 mg/s operation. The simulation should not be expected to accurately reproduce conditions near the cathode on channel centerline, since HPHall does not explicitly model the cathode, but at $z/L_c > 1$ where no cathode is nearby the simulation also overestimates the plasma potential by several volts. This would allow lower temperature electrons to reach these regions in electron trajectory simulations.

surface would take place. As a result, simulations using fully experimental measurements of fields in these regions are preferable. To the author's knowledge only one other brief published work to date beside his own[78,83] has simulated electron trajectories in experimentally measured thruster fields.[59]

2.5 Hall Parameter Gap

The Hall parameter is a convenient metric to note regions in the Hall thruster plume where anomalous transport must be imposed in a model. It can be computed experimentally in two different ways, and the difference illustrates the presence of anomalous transport mechanisms. The first calculation method produces a classical Hall parameter by relating the cyclotron frequency to the sum of the electron-neutral, electron-ion and electron-wall collision frequencies, thus describing how well electrons would be confined by the magnetic field if those transport processes were the only ones taking place. The second method computes a total Hall parameter, including the effects of all transport processes, by directly comparing azimuthal to axial current density, as explained in more detail by Haas.[30] The difference between the two is the turbulent Bohm collision frequency of Eqn. 2.15. Where the two classical and total Hall parameters differ, the difference is because some form of anomalous transport must be taking place in the plasma.

In the H6 Reid calculated both Hall parameters at several 300 V operating conditions (Figure 2.4).[73] The clearest difference between these two quantities is in the near field, where the total Hall parameter is about 1000 times larger than the classical Hall parameter. The definition of the near field varies, but one reasonable definition is the region within a few characteristic thruster lengths downstream of the exit plane, for example 1-2 channel lengths or discharge channel diameters. In the

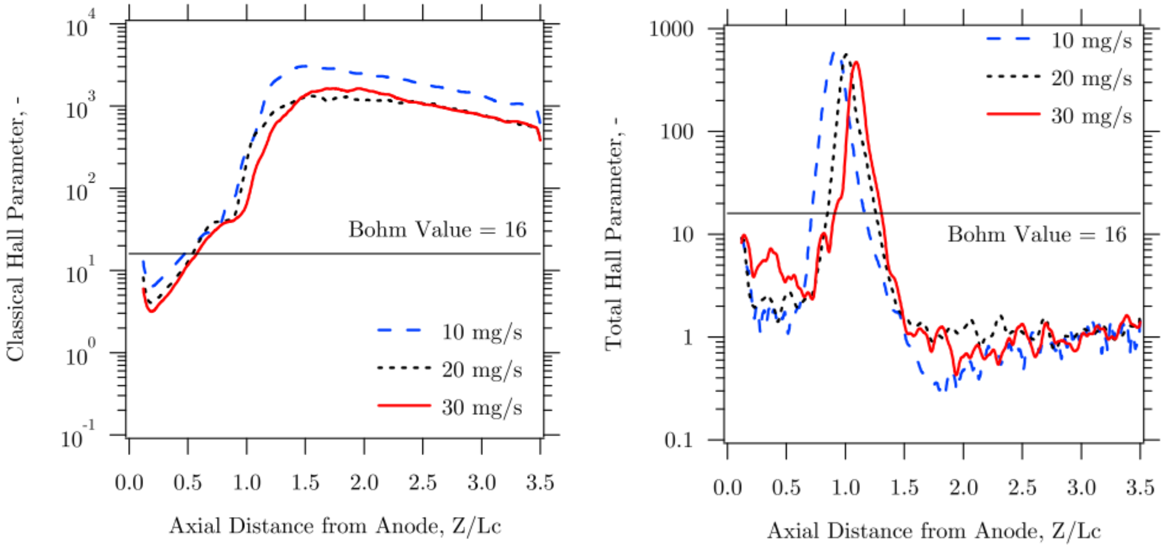

Figure 2.4. The classical Hall parameter, left, includes only collisional scattering with neutrals, ions and walls and as a result becomes extremely large downstream of the exit plane. By contrast, the total Hall parameter peaks near the exit plane in the acceleration and ionization regions and drops significantly both in the discharge channel, where collisional transport mostly explains the effect, and in the near field, where turbulent transport must be invoked. Figures from Reid.[73]

figure the Bohm value of the Hall parameter, i.e., the value obtained if the collision frequency is just the Bohm collision frequency with $\alpha_B = 1$, is shown for reference.

Reid went one step further and, using the difference in the Hall parameters to calculate an effective experimental turbulent collision frequency, compared this level of turbulence to a normalized value calculated from the Bohm collision frequency, again with $\alpha_B = 1$. This “turbulence intensity ratio” is shown in Figure 2.5, and shows both the expected large values in the near-field and also some moderate values between 1-10 in the discharge channel. This region is usually considered well described by collisional transport, but this may indicate there is room for turbulent transport mechanisms here as well.

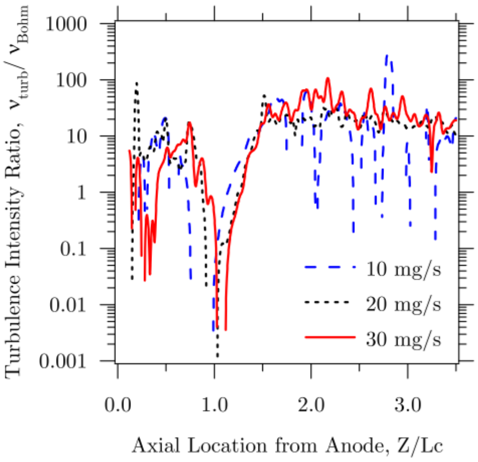

Figure 2.5. The ratio of the turbulent collision frequency calculated from the information in Figure 2.4 to the Bohm collision frequency in the H6 channel and near-field at several 300 V operating conditions. The values are largest in the near-field, indicating the presence of substantial anomalous turbulent transport in this area, and are also notable in the channel upstream of the ionization and acceleration regions. Figure from Reid.[73]

2.6 Summary

The picture of electron transport in the Hall thruster is complicated. There are many results, often conflicting, and it is difficult to draw together a coherent picture of which electron transport mechanisms are dominant in the thruster. It is entirely possible that different mechanisms are dominant in different regions of the plume and channel, and different thruster configurations (internal vs. external cathode, high vs. low power, single channel vs. nested) may also impact the interplay between mechanisms.

This thesis identifies two areas for focus. The first is on the potential of electron trajectory modeling to shed light on the importance of collisional transport with thruster surfaces in the near field, following the work of Smith in this area. Given the observed differences between experimental and simulated plasma potential profiles in the regions near thruster surfaces, there is a potential for electron trajectory simulations using fully experimental plasma potential profiles to estimate the influence of this mechanism with higher fidelity.

The second area of focus, and the larger portion of this work, is on the low-frequency turbulent transport mechanisms called rotating spokes, introduced in Section 2.3.2.1 and discussed in Chapter V. Rotating spokes were among the first demonstrated turbulent transport mechanisms in Hall thrusters, and while they have rarely been observed in Hall thrusters since the early investigations of Janes and Lowder, it seems entirely possible this is only because investigators have rarely gone looking for them.[11] Several cases of observation have been reported since Janes, including the work of Lomas, Chesta, and recently Parker and Ellison.[24,51,54,80] Through the development of new analysis techniques for high speed video, an extensive characterization of the presence of rotating spokes across various operating conditions will be undertaken. The high-speed camera offers a new technique to detect rotating spokes with orders of magnitude less difficulty than the insertion of in situ probes in the harsh plasma of the Hall thruster discharge channel. The implementation of an azimuthally segmented anode in the H6 Hall thruster will be used to link the oscillations observed on camera with electron current fluctuations in the discharge channel, and will also provide one of the first quantitative experimental estimates of the level of cross-field electron current due to any turbulent transport mechanism, and the first on a modern high-power Hall thruster.

[1] Yoshikawa, S. and Rose, D. J., "Anomalous Diffusion of a Plasma across a Magnetic Field," *Physics of Fluids*, Vol. 5, 1962, pp. 334.

[2] de Grys, K., Mathers, A., Welander, B., and Khayms, V., "Demonstration of 10,400 Hours of Operation on 4.5 kW Qualification Model Hall Thruster," AIAA 2010-6698, Nashville, TN, July 2010.

[3] Spitzer, L., "Particle Diffusion across a Magnetic Field," *Physics of Fluids*, Vol. 3, No. 4, July 1960, pp. 659–661.

[4] Smith, A. W. and Cappelli, M. A., "Time and space-correlated plasma potential measurements in the near field of a coaxial Hall plasma discharge," *Physics of Plasmas*, Vol. 16, No. 7, 2009, pp. 073504–11.

[5] Mikellides, I. G., Katz, I., Hofer, R. R., and Goebel, D. M., "Numerical Simulations of a 20-kW Class Hall Thruster Using the Magnetic-Field-Aligned-Mesh Code Hall2De," *32nd International Electric Propulsion Conference*, IEPC-2011-244, Wiesbaden, Germany, 2011.

[6] Bohm, D., Burhop, E. H. S., and Massey, H. S. W., "The Use of Probes for Plasma Exploration in Strong Magnetic Fields," *The Characteristics of Electrical Discharges in Magnetic Fields*, edited by A. Guthrie and R. Wakerling, McGraw-Hill, 1949.

[7] Adam, J. C., Boeuf, J. P., Dubuit, N., Dudeck, M., Garrigues, L., Gresillon, D., Heron, A., Hagelaar, G. J. M., Kulaev, V., Lemoine, N., Mazouffre, S., Perez Luna, J., Pisarev, V., and Tsikata, S., "Physics, simulation and diagnostics of Hall effect thrusters," *Plasma Physics and Controlled Fusion*, Vol. 50, Dec. 2008, pp. 4041.

[8] Keidar, M. and Beilis, I., "Electron transport phenomena in plasma devices with ExB drift," *Plasma Science, IEEE Transactions on*, Vol. 34, No. 3, 2006, pp. 804–814.

[9] Litvak, A. A. and Fisch, N. J., "Rayleigh instability in Hall thrusters," *Physics of Plasmas*, Vol. 11, No. 4, April 2004, pp. 1379–1383.

[10] Strange, N., Merrill, R., Landau, D., Drake, B., Brophy, J., and Hofer, R., "Human Missions to Phobos and Deimos Using Combined Chemical and Solar Electric Propulsion," July 2011.

[11] Janes, G. S. and Lowder, R. S., "Anomalous Electron Diffusion and Ion Acceleration in a Low-Density Plasma," *Physics of Fluids*, Vol. 9, 1966, pp. 1115.

[12] Koo, J. W. and Boyd, I. D., "Modeling of anomalous electron mobility in Hall thrusters," *Physics of Plasmas*, Vol. 13, No. 3, March 2006, pp. 033501–7.

[13] Lazurenko, A., de Wit, T. D., Cavoit, C., Krasnoselskikh, V., Bouchoule, A., and Dudeck, M., "Determination of the electron anomalous mobility through measurements of turbulent magnetic field in Hall thrusters," *Physics of Plasmas*, Vol. 14, No. 3, March 2007, pp. 033504–11.

[14] Salz, F., Meyerand, R., and Lary, E., "Ion Acceleration in a Gyro-Dominated Neutral Plasma Experiment," *Bulletin of the American Physical Society, Sr. II*, Vol. 7, 1962, pp. 441.

[15] Fife, J. M., Martinez-Sanchez, M., and Szabo, J., "A numerical study of low-frequency discharge oscillations in Hall thrusters," *33rd AIAA/ASME/SAE/ASEE Joint Propulsion Conference & Exhibit, Seattle, WA*, 1997.

[16] Chen, F. F., *Introduction to Plasma Physics and Controlled Fusion: Plasma physics*, Plenum Press, New York, Feb. 1984.

[17] Smith, A. W. and Cappelli, M. A., "Numerical investigation of electron behavior in the near-field of Hall thrusters," 43rd AIAA/ASME/SAE/ASEE Joint Propulsion Conference & Exhibit, Cincinnati, OH, AIAA 2007-5240, 2007.

[18] Lary, E., Meyerand, R., and Salz, F., "Ion Acceleration in a Gyro-Dominated Neutral Plasma–Theory," *Bulletin of the American Physical Society, Sr. II*, Vol. 7, 1962, pp. 441.

[19] Hess, R. V., Burlock, J., Sidney, B., Brockman, P., and Weinstein, R. H., *Study of instabilities and transition to turbulence in a linear Hall accelerator*, 1964.

[20] Brophy, J., Gershman, R., Strange, N., Landau, D., Merrill, R., and Kerslake, T., "300-kW Solar Electric Propulsion System Configuration for Human Exploration of Near-Earth Asteroids," July 2011.

[21] Brenning, N., “Review of the CIV phenomenon,” *Space Science Reviews*, Vol. 59, Feb. 1992.

[22] Fife, J. M., *Hybrid-PIC Modeling and Electrostatic Probe Survey of Hall Thrusters*, Ph.D. thesis, Massachusetts Institute of Technology, Cambridge, MA, 1998.

[23] Zhurin, V. V., Kaufman, H. R., and Robinson, R. S., “Physics of closed drift thrusters,” *Plasma Sources Sci. Technol*, Vol. 8, No. 1, 1999.

[24] Lomas, P. J. and Kilkenny, J. D., “Electrothermal instabilities in a Hall accelerator,” *Plasma Physics*, Vol. 19, No. 4, 1977, pp. 329–341.

[25] Pérez-Luna, J., Hagelaar, G. J. M., Garrigues, L., Dubuit, N., and Boeuf, J. P., “Influence of azimuthal instabilities on electron motion in a Hall effect thruster,” *30th International Electric Propulsion Conference*, 2007, p. 17–20.

[26] Brown, D., Larson, C., Beal, B., and Gallimore, A., “Methodology and Historical Perspective of a Hall Thruster Efficiency Analysis,” *Journal of Propulsion and Power*, Vol. 25, No. 6, 2009, pp. 1163–1177.

[27] Ellison, L., Raitses, Y., and Fisch, N. J., “Fast Camera Imaging of Hall Thruster Ignition,” *IEEE Transactions on Plasma Science*, 2011, (to be published).

[28] Alfvén, H., “Collision between a Nonionized Gas and a Magnetized Plasma,” *Reviews of Modern Physics*, Vol. 32, No. 4, 1960, pp. 710.

[29] Morozov, A. I., “Wall conduction in a highly magnetized plasma,” *Journal of Applied Mechanics and Technical Physics*, Vol. 9, No. 3, 1968, pp. 249–251.

[30] Haas, J. M., Gallimore, A. D., McFall, K., and Spanjers, G., “Development of a high-speed, reciprocating electrostatic probe system for Hall thruster interrogation,” *Review of Scientific Instruments*, Vol. 71, 2000, pp. 4131.

[31] Brophy, J., Gershman, R., Landau, D., Polk, J., Porter, C., Yeomans, D., Allen, C., Williams, W., and Asphaug, E., “Asteroid Return Mission Feasibility Study,” July 2011.

[32] Seikel, G. and Reshotko, E., “Hall current ion accelerator,” *Bull, Am. Phys. Soc*, 1962.

[33] McDonald, M. S. and Gallimore, A. D., “Measurement of Cross-Field Electron Current in a Hall Thruster Due to Rotating Spoke Instabilities,” *47th AIAA/ASME/SAE/ASEE Joint Propulsion Conference & Exhibit*, AIAA 2011-5810, 2011.

[34] Litvak, A. A. and Fisch, N. J., “Resistive instabilities in Hall current plasma discharge,” *Physics of Plasmas*, Vol. 8, No. 2, Feb. 2001, pp. 648–651.

[35] Linnell, J. A., *An Evaluation of Krypton Propellant in Hall Thrusters*, Ph.D. thesis, 2007.

[36] Komurasaki, K. and Arakawa, Y., “Two-dimensional numerical model of plasma flow in a Hall thruster,” *Journal of Propulsion and Power*, Vol. 11, No. 6, Nov. 1995, pp. 1317–1323.

[37] Fernandez, E., Knoll, A., and Cappelli, M. A., “An axial-azimuthal hybrid simulation of coaxial Hall thrusters,” *42nd AIAA/ASME/SAE/ASEE Joint Propulsion Conference & Exhibit*, AIAA 2006-4329, 2006.

[38] Pinsley, E. A., “Characteristics of a Surface Contact Hall Current Accelerator,” *IEEE Transactions on Nuclear Science*, Vol. 11, No. 1, Jan. 1964, pp. 58–65.

[39] Allario, F., Hess, R. V., and Sidney, B. D., “Onset of rotating disturbance in linear Hall-current accelerator,” *AIAA Journal*, Vol. 8, No. 6, June 1970, pp. 1117–1120.

[40] Litvak, A. A., Raitses, Y., and Fisch, N. J., “Experimental studies of high-frequency azimuthal waves in Hall thrusters,” *Physics of Plasmas*, Vol. 11, No. 4, April 2004, pp. 1701–1705.

[41] Mikellides, I. G., Katz, I., and Hofer, R. R., “Design of a Laboratory Hall Thruster with Magnetically Shielded Channel Walls, Phase I: Numerical Simulations,” *47th AIAA/ASME/SAE/ASEE Joint Propulsion Conference & Exhibit*, AIAA 2011-5809, 2011.

[42] Lazurenko, A., Vial, V., Prioul, M., and Bouchoule, A., “Experimental investigation of high-frequency drifting perturbations in Hall thrusters,” *Physics of Plasmas*, Vol. 12, No. 1, Jan. 2005, pp. 013501–9.

[43] Choueiri, E. Y., “Plasma oscillations in Hall thrusters,” *Physics of Plasmas*, Vol. 8, No. 4, 2001, pp. 1411.

[44] Parra, F. I., Ahedo, E., Fife, J. M., and Marti?nez-Sa?nchez, M., “A two-dimensional hybrid model of the Hall thruster discharge,” *Journal of Applied Physics*, Vol. 100, No. 2, 2006, pp. 023304.

[45] Cochran, R. A. and Fay, J. A., “Occurrence and behavior of current spokes in MPD arcs,” *AIAA Journal*, Vol. 9, No. 5, May 1971, pp. 886–893.

[46] Mikellides, I. G., Katz, I., Hofer, R. R., and Goebel, D. M., “Hall-Effect Thruster Simulations with 2-D Electron Transport and Hydrodynamics Ions,” *31st International Electric Propulsion Conference*, IEPC-2009-114, Ann Arbor, MI, 2009.

[47] Hofer, R., Mikellides, I., Katz, I., and Goebel, D., “Wall Sheath and Electron Mobility Modeling in Hybrid-PIC Hall Thruster Simulations,” July 2007.

[48] Adam, J. C., Héron, A., and Laval, G., “Study of stationary plasma thrusters using two-dimensional fully kinetic simulations,” *Physics of Plasmas*, Vol. 11, 2004, pp. 295.

[49] Brown, C. and Pinsley, E., “Further experimental investigations of a cesium hall-current accelerator(Electrical propulsion thrustor using cesium hall current accelerator to achieve high thrust densities and efficiencies at moderate specific impulses),” 1964.

[50] Lobbia, R. B. and Gallimore, A. D., “A Method of Measuring Transient Plume Properties,” July 2008.

[51] Ellison, C. L., Raitses, Y., and Fisch, N. J., “Cross-field electron transport induced by a rotating spoke in a cylindrical Hall thruster,” *Physics of Plasmas*, Vol. 19, No. 1, Jan. 2012, pp. 013503–013503–7.

[52] Nelson, A. H. and Haines, M. G., “Analysis of the nature and growth of electrothermal waves,” *Plasma Physics*, Vol. 11, No. 10, 1969, pp. 811–837.

[53] Lai, S. T., “A review of critical ionization velocity,” *Reviews of Geophysics*, Vol. 39, No. 4, 2001, pp. PP. 471–506.

[54] Chesta, E., Lam, C. M., Meezan, N. B., Schmidt, D. P., and Cappelli, M. A., “A characterization of plasma fluctuations within a Hall discharge,” *Plasma Science, IEEE Transactions on*, Vol. 29, No. 4, 2001, pp. 582–591.

[55] Janes, G. S., Dotson, J., and Wilson, T., *ELECTROSTATIC ACCELERATION OF NEUTRAL PLASMAS–MOMENTUM TRANSFER THROUGH MAGNETIC FIELDS*, 1962.

[56] Chesta, E., Meezan, N. B., and Cappelli, M. A., “Stability of a magnetized Hall plasma discharge,” *Journal of Applied Physics*, Vol. 89, No. 6, March 2001, pp. 3099–3107.

[57] Sherman, J., “Review of the critical velocity of gas-plasma interaction,” *Astrophysics and Space Science*, Vol. 24, No. 2, Oct. 1973, pp. 487–510.

[58] Smith, A. W. and Cappelli, M. A., “Single particle simulations of electron transport in the near-field of Hall thrusters,” *Journal of Physics D: Applied Physics*, Vol. 43, No. 4, 2010, pp. 045203.

[59] Alman, D. A., Rovey, J. L., Stubbers, R. A., and Jurczyk, B. E., “Hall Thruster Electron Mobility Investigation using Full 3D Monte Carlo Trajectory Simulations,” *30th International Electric Propulsion Conference*, IEPC 2007-291, 2007.

[60] Jameson, K., *Investigation of Hollow Cathode Effects on Total Thruster Efficiency in a 6-kW Hall Thruster*, Ph.D. thesis, University of California Los Angeles, Los Angeles, CA, 2008.

[61] Lobbia, R. B. and Gallimore, A. D., “High-speed dual Langmuir probe,” *Review of Scientific Instruments*, Vol. 81, No. 7, 2010, pp. 073503.

[62] Hagelaar, G. J. M., Bareilles, J., Garrigues, L., and Boeuf, J. P., “Two-dimensional model of a stationary plasma thruster,” *Journal of Applied Physics*, Vol. 91, No. 9, 2002, pp. 5592.

[63] Lazurenko, A., Albarede, L., and Bouchoule, A., “Physical characterization of high-frequency instabilities in Hall thrusters,” *Physics of Plasmas*, Vol. 13, No. 8, 2006, pp. 083503–6.

[64] Boeuf, J. P. and Garrigues, L., “Low frequency oscillations in a stationary plasma thruster,” *Journal of Applied Physics*, Vol. 84, No. 7, Oct. 1998, pp. 3541–3554.

[65] Ellison, L., Raitses, Y., and Fisch, N. J., “Cross-field Current through a Rotating Spoke,” *53rd Annual Meeting of the American Physical Society Division of Plasma Physics*, Poster Presentation, 2010.

[66] Lobbia, R. B., *A Time-Resolved Investigation of the Hall Thruster Breathing Mode*, Ph.D. thesis, University of Michigan, Ann Arbor, MI, 2010.

[67] Lobbia, R. B. and Gallimore, A. D., "Temporal limits of a rapidly swept Langmuir probe," *Physics of Plasmas*, Vol. 17, No. 7, 2010, pp. 073502.

[68] Meezan, N. B., Hargus Jr, W. A., and Cappelli, M. A., "Anomalous electron mobility in a coaxial Hall discharge plasma," *Physical Review E*, Vol. 63, No. 2, 2001, pp. 26410.

[69] Hofer, R. R., Katz, I., Mikellides, I. G., Goebel, D. M., Jameson, K. K., Sullivan, R. M., and Johnson, L. K., "Efficacy of Electron Mobility Models in Hybrid-PIC Hall Thruster Simulations," 44th AIAA/ASME/SAE/ASEE Joint Propulsion Conference, Hartford, CT, AIAA-2008-4924, 2008.

[70] Shastry, R., *Experimental Characterization of the Near-Wall Region in Hall Thrusters and its Implications on Performance and Lifetime*, Ph.D. thesis, University of Michigan, Ann Arbor, MI, 2010.

[71] Wirz, R. E., *Discharge plasma processes of ring-cusp ion thrusters*, Ph.D. thesis, California Institute of Technology, Pasadena, CA, 2005.

[72] Alfven, H., *On the origin of the solar system.*, Clarendon Press, Oxford, 1954.

[73] Reid, B., *The Influence of Neutral Flow Rate in the Operation of Hall Thrusters*, Ph.D. thesis, University of Michigan, Ann Arbor, MI, 2009.

[74] Danielsson, L., "Review of the critical velocity of gas-plasma interaction," *Astrophysics and Space Science*, Vol. 24, No. 2, Oct. 1973, pp. 459–485.

[75] Lobbia, R. B. and Gallimore, A. D., "Two-dimensional Time-resolved Breathing Mode Plasma Fluctuation with Hall Thruster Discharge Settings," *31st International Electric Propulsion Conference*, IEPC 2009-106, 2009.

[76] Esipchuk, Y. V. and Tilinin, G. N., "Drift instability in a Hall-current plasma accelerator," Vol. 18, 1974, pp. 928.

[77] Pinsley, E., Brown, C., and Banas, C., "Hall-current accelerator utilizing surface contact ionization," *Journal of Spacecraft and Rockets*, Vol. 1, No. 5, 1964, pp. 525–531.

[78] McDonald, M. S., Gallimore, A., Hofer, R. R., and Goebel, D., "Development of a 3D Electron Trajectory Model with Monte Carlo Collisions for the Hall Thruster Near-Field Plume," 57th Joint Army/Navy/NASA/Air Force (JANNAF) Propulsion Subcommittee Meeting, Colorado Springs, CO JANNAF-1192, 2010.

[79] Bird, K. and Sherwin, M. J., *American Prometheus: the Triumph and Tragedy of J. Robert Oppenheimer*, Random House Digital, Inc., April 2006.

[80] Parker, J. B., Raitses, Y., and Fisch, N. J., "Transition in electron transport in a cylindrical Hall thruster," *Applied Physics Letters*, Vol. 97, No. 9, 2010, pp. 091501.

[81] Perez-Luna, J., Dubuit, N., Garrigues, L., Hagelaar, G., and Boeuf, J., "Electron Trajectories in a Hall Effect Thruster Anomalous Transport Induced by an Azimuthal Wave," *Plasma Science, IEEE Transactions on*, Vol. 36, No. 4, 2008, pp. 1212–1213.

[82] Smith, A. W. and Cappelli, M. A., "Investigation of field structure and electron behavior in near-field of Hall thrusters," 42nd AIAA/ASME/SAE/ASEE Joint Propulsion Conference and Exhibit, Sacramento, CA, AIAA 2006-4835, 2006.

[83] McDonald, M. and Gallimore, A., "Electron Trajectory Simulation in Experimental Hall Thruster Fields," *32nd International Electric Propulsion Conference*, IEPC 2011-243, Wiesbaden, Germany, 2011.

CHAPTER III

Experimental Equipment, Setup and Background

"It doesn't matter how beautiful your theory is, it doesn't matter how smart you are. If it doesn't agree with experiment, it's wrong.

Richard Feynman

The work in this dissertation is largely experimental in nature. This chapter outlines the equipment used and, where appropriate, delves into their principles of operation. All experiments were performed at the Plasmadynamics and Electric Propulsion Laboratory (PEPL) at the University of Michigan in the Large Vacuum Test Facility (LVTF) on the H6 6-kW Hall thruster. The diagnostic techniques applied to the H6 include the use of a drop-in azimuthally segmented anode, ex situ optical investigations via high-speed camera and planar Langmuir probes flush-mounted to the inner and outer pole pieces.

3.1 Large Vacuum Test Facility (LVTF)

The LVTF is a stainless steel-clad vacuum chamber 9 m long and 6 m in diameter, with an approximate volume of 200 m^3. The chamber, originally built in 1961 by the Bendix Corporation as a space simulation chamber with thermal testing capability, was later donated to the University of Michigan in the 1980s. Now the centerpiece

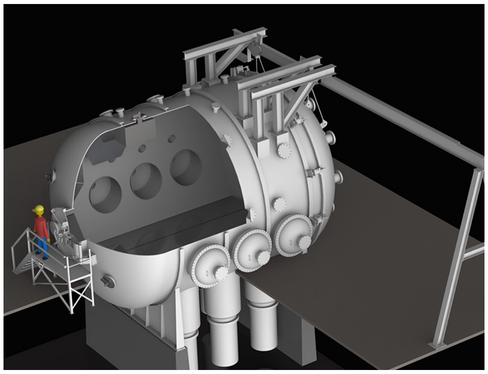

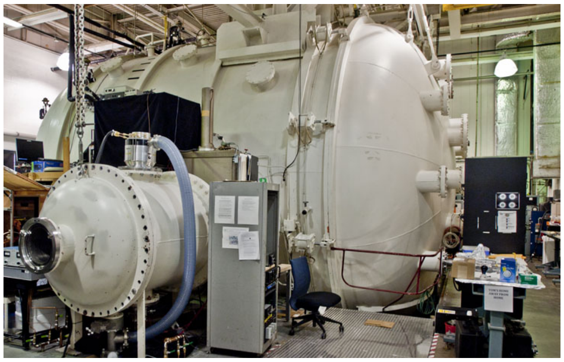

Figure 3.1. Left, a cutaway CAD model of the Large Vacuum Test Facility with a 6' person shown for scale, image courtesy of ElectroDynamic Applications Inc.; right, a photo of the chamber circa 2010 also showing the smaller side chamber in the foreground.

of PEPL, it is the largest university vacuum chamber in the nation. The chamber is brought to rough vacuum by two 2000 CFM blowers backed by four 400 CFM mechanical pumps. Seven CVI TM-1200 re-entrant cryopumps with LN2 baffles and a nominal pumping speed of 500,000 L/s on air or 240,000 L/s on xenon achieve high vacuum in the low 10^{-7} to high 10^{-8} Torr range.

3.2 The H6 Hall thruster

The H6 Hall thruster is a 6-kW class Hall thruster with a nominal operating condition at 300 V and 20 mg/s anode flow rate (approximately 20 A discharge current) with a 7% cathode flow fraction. The H6 is a joint development effort of the University of Michigan, Jet Propulsion Laboratory and the Air Force Research Laboratory, and a separate copy of the thruster is maintained at each institution. It is notable for its high total efficiency, 60% at nominal operation and 70% at 800 V, 6-kW operation.[12,25]

At its nominal operating condition the H6 produces approximately 400 mN of thrust at a specific impulse of about 1900 s.[25] It uses a center-mount cathode with a lanthanum hexaboride (LaB_6) insert with the cathode exit plane flush with the discharge channel exit plane. The channel exit plane sits a few millimeters forward of the inner and outer pole pieces. More detailed dimensions for the thruster are given by Jameson.[18]

The H6 has been well-characterized by a variety of diagnostic and modeling techniques at Michigan, JPL and AFRL since its first firing in 2006. The present work marks the sixth doctoral dissertation focusing on the thruster, following those of Jameson, Reid, Brown, Shastry and Huang.[8,18,23,25] Experimental work on the H6 includes investigations of cathode coupling with internal and external cathode operation,[24] internal probing of the discharge channel with Langmuir and emissive probes,[3 9] low-voltage operating characteristics in the 100-150 V range,[16] plasma-wall interactions using embedded Langmuir probes in the discharge channel wall[20] and 2-axis laser-induced fluorescence measurements of ion velocity profiles in the acceleration zone and near field.[6] Modeling of the H6 has been performed using both

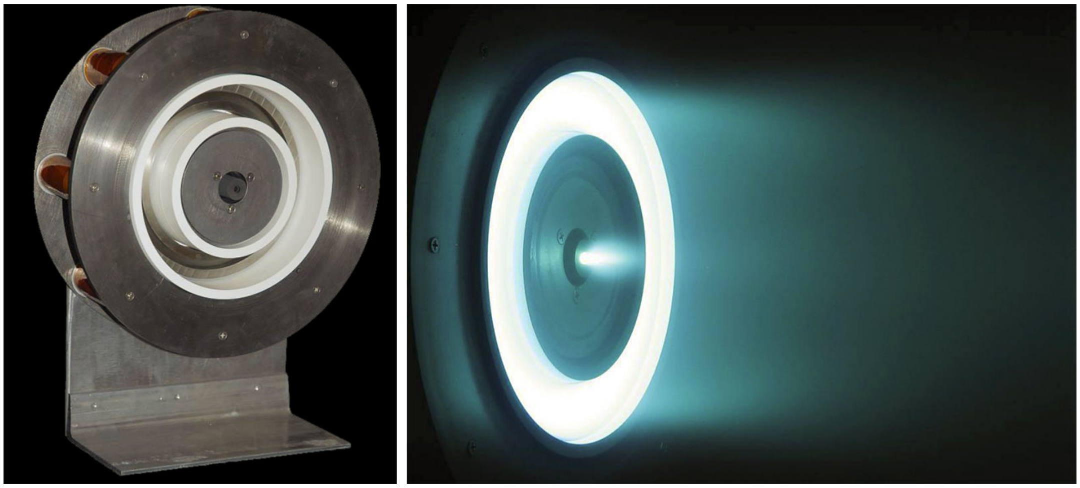

Figure 3.2. The H6 6-kW Hall thruster, left, before first firing in 2006; right, firing at nominal 300 V, 20 mg/s (20 A) operating conditions. Images courtesy of Reid.[25]

the quasi-1D HPHall-2[15,22] and the more recent fully two dimensional Hall-2De.[12,14]

3.2.1 Segmented Anode

An azimuthally segmented anode was retrofitted onto the H6 to resolve rotating points of electron current deposition to the anode, as part of the investigation into turbulent transport by rotating spoke instabilities in Chapter V. The segmented anode is a set of 12 independently monitored electrodes biased at anode potential and equally spaced azimuthally at the rear of the annular Hall thruster channel. The number of segments was chosen in order to resolve spoke modes with up to 5-6 spokes present simultaneously, though generally only modes with 2-3 simultaneous spokes are observed.

3.2.1.1 Segmented Anode Design

The segmented anode was designed with the express goal of making minimal if any changes to the original H6 structure. The existing magnetic circuit and discharge channel were left completely intact, e.g., no holes were drilled through the pole pieces or channel walls. Installation is instead an entirely reversible procedure with the

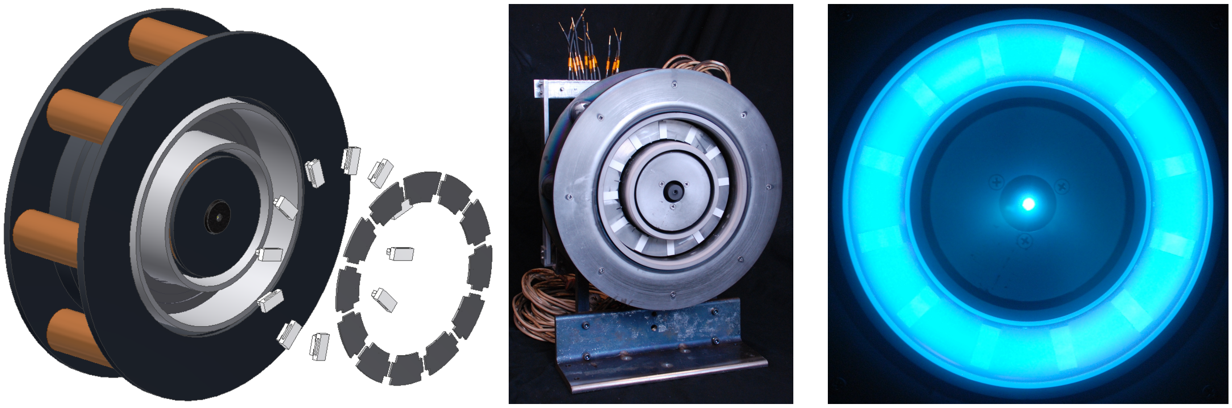

Figure 3.3. Left, an exploded view of the H6 Hall thruster with segmented anode, showing the 12 boron nitride spacers and 12 stainless steel anode segments. Middle, the thruster fully assembled with the segmented anode installed. The 12 current lines for the segments are visible rising out the back of the thruster. Right, an axial view of the thruster firing with the segmented anode installed. The white boron nitride spacers are more reflective than the stainless steel anode segments, and so appear brighter in the image. This vantage point is also used to record the high-speed video presented in Chapter V.

segmented anode installed over the original anode, which is retained as an electrically floating gas distributor. Current-carrying lines are routed out the rear of the thruster through clearance in existing holes for the anode mechanical support studs.

The anode segments are machined from a single solid ring of 300-series stainless steel and are held in place and electrically isolated from the original H6 anode and from each other by insulating boron nitride (BN) spacers (see Figure 3.3). The BN spacers are in turn held in place on the original contiguous H6 anode by means of a twist-and-lock mechanism similar to channel nuts in unistrut framing. The extra height of the spacers and segments over the original anode plus the space behind the anode required to route the current-carrying wires out the anode support holes effectively shortens the discharge channel to 90% of its original unmodified length as measured from the anode surface to the exit plane, and the BN spacers rise an additional 1.5 mm above each anode segment. The introduction of the segmented anode also effectively converts the H6 from an axial to a radial neutral injection scheme, rerouting the flow around the segments to the inner and outer channel radii. The implications of this change in neutral flow dynamics are not explored, though a comparison between operation with and without the segmented anode is made in Section 5.3.3.2.

Copper wires with polyamide/imide insulation 1.0 mm in diameter (.040" or 18 AWG) are attached to each segment and mechanically held in place by a crimped ring terminal connection connection to a 1/8" long 0-80 threaded screw that secures into a tapped hole on the inner diameter of each anode segment. Both the ring terminal and 0-80 screw are 18-8 stainless steel. As noted above these lines are routed out the rear of the thruster through clearance in the holes for the original anode's support studs. At that point they connect to 22 AWG coaxial cables that run 25 feet to the chamber feedthrough and another 3 feet outside the chamber to the measurement circuitry.

The tight fit between the current carrying wires and the inner radius of the discharge channel make this the region most susceptible to breakdown between the segments and the original anode. This is also the hottest region during thruster operation, as the wires experience both Ohmic heating from the discharge current through the wire and direct heating from segments as the discharge current falls through the anode sheath. Isolation from the floating anode is maintained by polyamide/polyimide lacquer on the magnet wire, fiberglass tape and a layer of mica insulation. The magnet wire alone demonstrated isolation up to 2 kV at atmosphere and room temperature, but is only rated to a temperature of 200 C. The fiberglass tape holds the mica in place as an additional high-temperature insulator.

Finally, during initial firing with the segmented anode frequent visible flashes of plasma could be seen on high speed video behind the anode segments, suggesting some sort of glow discharge or Paschen breakdown in the narrow gaps and relatively high pressure (several Torr) in the rear of the discharge channel between the floating original anode and the anode segments at high voltage. To combat this the entire outer surface of the original anode was coated in a layer of polyimide (Kapton) tape, and no further flashing was visible during the final trials.

3.2.1.2 Measurement Circuitry

The measurement circuitry for the segmented anode is necessarily biased to anode voltage and in series with the main discharge. As a result all current sensors are contained within a Plexiglas box during the experiment. The current to each anode segment is monitored by a F.W. Bell NT-5 magneto-resistive current sensor. The NT-5 is a nominal 5 amp current sensor capable of handling current spikes up to 50 A and with voltage isolation to 3500 V.

The specified NT-5 measurement bandwidth is DC to 100 kHz, and all sensors are simultaneously sampled at 1 MHz. Due to the 100 kHz bandwidth limit on the NT-5, all segmented anode current measurements presented in this paper have been passed through a digital anti-aliasing low-pass Butterworth filter in MATLAB postprocessing using the built-in function *filtfilt* with a cutoff frequency at 100 kHz.

Owing to the large number of current signals to be acquired, 8 segments are sampled on a General Standards PMC-16AISS8AO4 8-channel 16-bit data acquisition board with independent analog-to-digital converters on each channel, while the remaining 4 segments are captured to internal memory on an Agilent DSO-X 3024A 4-channel digital oscilloscope operating in an enhanced 9-bit acquisition mode.

In addition to individual segment current measurements through the NT-5 sensors, two split-core Hall probe measurements of the AC-coupled discharge current

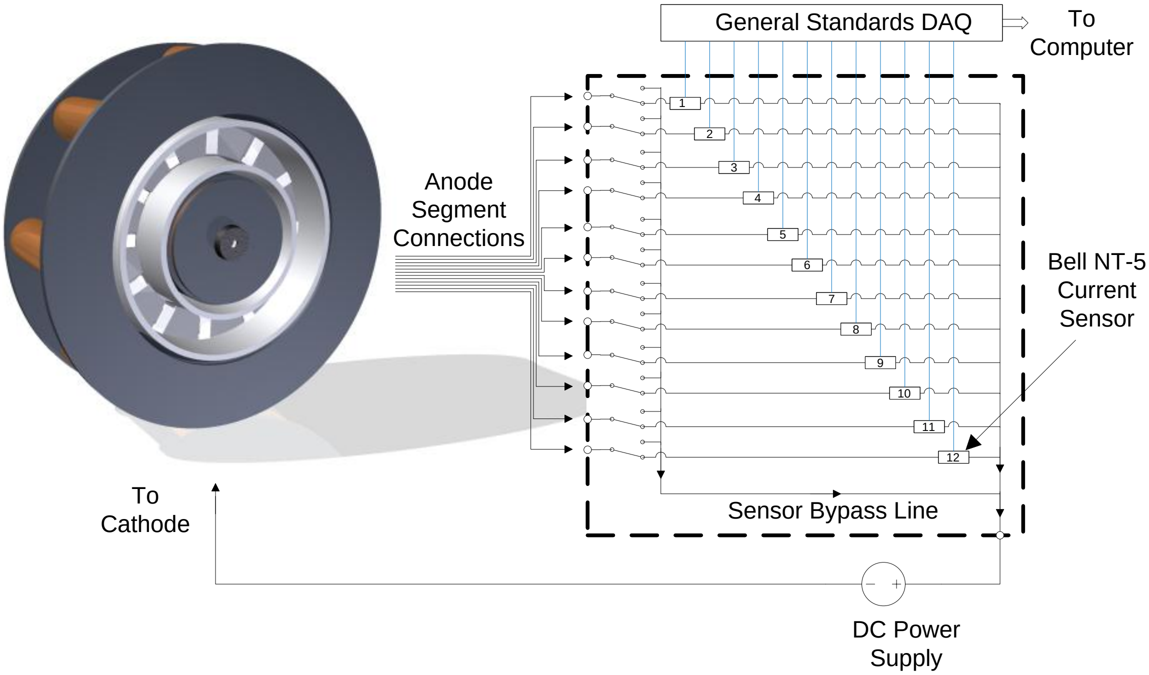

Figure 3.4. The segmented anode measurement circuit, contained in a Plexiglas box denoted by the dotted lines, consists of 12 separate current carrying lines to each anode segment. The lines pass through 12 FW Bell NT-5 magnetoresistive current sensors before rejoining into a single line to the main power supply. Each line additionally has a switch to bypass the sensors and the data acquisition system during thruster startup and shutdown transients. Split-core Hall sensors on the anode and cathode lines are not shown.

oscillations were also recorded. The first, with a Tektronix TCP303 sensor and TCPA300 amplifier, was just upstream of the measurement circuitry on the anode side, measuring the full oscillations of the discharge current from the supply before the lines split off to each segment. The second, with a Tektronix TCP312 sensor and TCPA300 amplifier, was on the cathode side of the circuit. These signals were recorded at 180 MHz and provided high-bandwidth confirmation of the oscillations observed with the FW Bell NT-5's.

3.3 Optical Diagnostics with a High Speed Camera

Optical diagnostics of the Hall thruster historically have focused on laser-induced fluorescence, or on the detection of single signals from isolated locations by photodiodes.[6,11,19] Only recently has it become possible to take full video of an operating Hall thruster at sufficient resolution and frame rate to capture meaningful images. The first of these investigations was undertaken by Darnon in the late 1990s, capturing the breathing mode in visible oscillations of light intensity.[17] Parker and Ellison have recently used a high-speed camera on the Princeton cylindrical Hall thruster as well, as has Liu on the Busek BHT-200.[7,13,26] Previous high-speed imaging work on the H6 and other thrusters at PEPL during the development of this dissertation has also been published.[1,5,10]

Two high speed cameras are used in this thesis. The more capable of the two and the one used for most images shown in this thesis is a Photron SA5 FASTCAM, typically used with a Nikon ED AF Nikkor 80-200mm lens at its maximum aperture f/2.8. The SA5 is capable of full megapixel 1024x1024 resolution with 12 bits per pixel at up to 7,000 frames per second (fps), with a peak framerate over 1,000,000 fps at high-aspect ratio and low resolution. For this test it was often operated at 87,500 fps at a 256x256 pixel resolution. A 1:1 aspect ratio (square image) is best for Hall thruster imaging to capture the entire discharge channel and make unambiguous identification of rotating instabilities. A second unit, a Photron 1024PCI FASTCAM, is used in some cases and noted in image captions where applicable. The 1024PCI is an older model with approximately one tenth the imaging capability of the SA5 and a 10 bit-per-pixel bit depth. The peak framerate is 109,000 fps at 64 x 8 resolution and is typically employed at 128 x 128 resolution at 27,000 fps. This is about the minimum frame rate necessary to capture meaningful Hall thruster plasma images, since it puts the Nyquist frequency of the framerate in the middle of the typical breathing mode frequencies of most Hall thrusters. Table 3.1 shows maximum framerates for several square aspect ratio resolutions for both cameras above the 27,000 fps level, as well

Camera	Video length (sec)	Frame Rate (fps)	Resolution	Bit Depth	File Size (GB)
1024PCI	1	27000	128 x 128	10	0.55
SA5	1	87500	256 x 256	12	8.6
SA5	1	262500	128 x 128	12	6.5
SA5	1	581250	64 x 64	12	3.6

Table 3.1. File sizes for square aspect ratio high-speed video with the Photron FAST-CAMs 1024PCI and SA5

as corresponding file sizes for each video according to the formula:

$$[GB] = (T\,seconds)\,(F\,fps)\,(M \times N\frac{pixels}{frame})\left(B\frac{bits}{pixel}\right)\left(\frac{1\,byte}{8\,bits}\right)\left(\frac{1\,GB}{10^9\,bytes}\right)$$

The high-speed cameras view the thruster axially through a quartz viewport with an interior sacrificial glass plate cover from approximately 6.5 meters downstream. In the horizontal plane (parallel to the ground) the viewport is raised above the thruster mounting surface and all high speed video and images are taken from approximately 2.5 degrees above the horizontal level of the thruster. For the experiments with the segmented anode the thruster was laser-aligned with the camera in the vertical plane; in all other videos the thruster is slightly angled from the camera to fire parallel to chamber centerline.

While the Hall thruster discharge appears steady to the naked eye and in still images as in Figure 3.2, the high-speed video reveals vigorous oscillations in the plasma, both overall flickering corresponding to the Hall thruster breathing mode as well as azimuthal instabilities of the type first reported by Janes and Lowder.[4] The breathing mode and azimuthal modes coexist, both spatially and temporally. Considering the large file sizes and extraordinary number of individual images in each video, Chapter V describes statistical analysis and visualization techniques have been developed to extract the frequency content of the Hall thruster instabilities and display them.

3.4 Surface-Mounted Langmuir Probes

Two arrays of planar Langmuir probes were mounted on the inner and outer pole pieces of the H6 to resolve details of the thruster extreme near-field and sheath behavior, as well as to investigate changes in this region due to changes in the electrical bias potential of the thruster as a whole. The probes themselves are made of stainless steel, and they are flush-mounted in a macor ceramic housing. The three inner probes have a diameter of 3.175 mm (0.125") and the four outer probes have a diameter of 4.763 mm (0.188"). These large diameters are intended to provide good signals in ion saturation given the low expected plasma densities in this region of the plume.

The ceramic housings for the probes are very thin, such that when mounted on the thruster face the probe surface is only 3 mm forward of the pole pieces. This low profile can be seen in Figure 3.5. Since only time-averaged measurements with these probes were desired, a Keithley 2410 high voltage sourcemeter operated through LabView swept the probe voltages and monitored the probe current, obviating the need for the isolation amplifiers often used with this diagnostic.

3.4.1 Langmuir Probe Operating Principles

The basic Langmuir probe configuration is a typically planar or cylindrical piece of metal immersed in the plasma and swept across a range of bias voltages. Subject to several assumptions about the nature of the plasma, the characteristic trace of current (I) drawn to the probe vs. bias voltage (V) can be interpreted to determine the plasma density, plasma potential and electron temperature. This subject is lengthy and plays only a small part in this dissertation, so while the basic principles

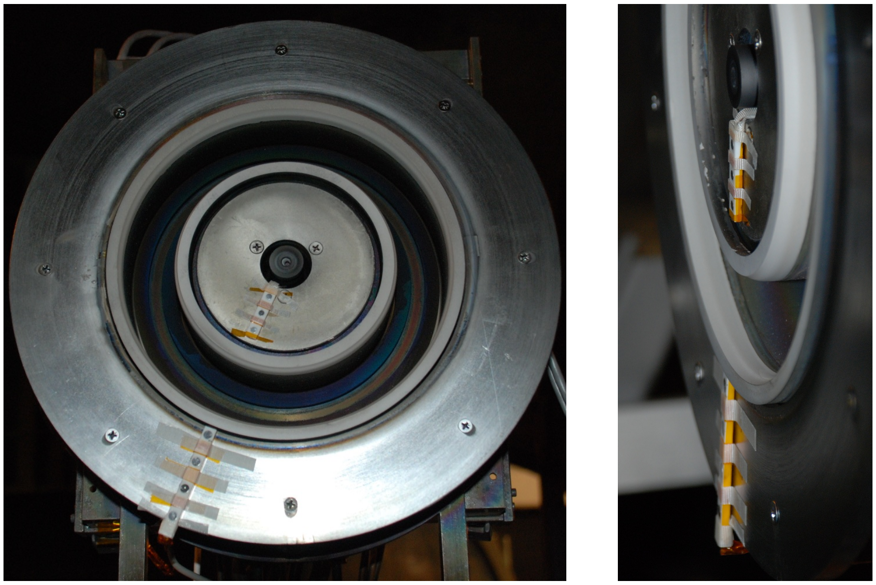

Figure 3.5. Left, arrays of planar Langmuir probes secured to the inner and outer H6 pole pieces; right, a side view demonstrates the low profile construction of the probes, less than 3 mm deep, to stay as nearly flush to the poles as possible.

of Langmuir probe operation are outlined below, for more detailed discussion of Langmuir probe operating principles the reader is referred to a more comprehensive resource such as Hershkowitz.[2]

Left to itself a Langmuir probe in a plasma settles at the floating potential, defined as the voltage where the probe draws zero net current, where the thermal fluxes of electrons and ions to the probe surface are in balance. At voltages below the floating voltage the probe slowly enters ion saturation, where the increasingly negative voltage repels electrons to the point where only ions are collected by the probe. In the opposite direction, at voltages far above the floating potential electrons are increasingly attracted to the probe and it enters electron saturation.

A typical Langmuir probe trace looks like the one found in Figure 3.6. The low mass of electrons compared to ions makes them far more mobile in response to an applied electric field, so the electron saturation current is many orders of magnitude larger than the ion saturation current. This makes their behavior the dominant

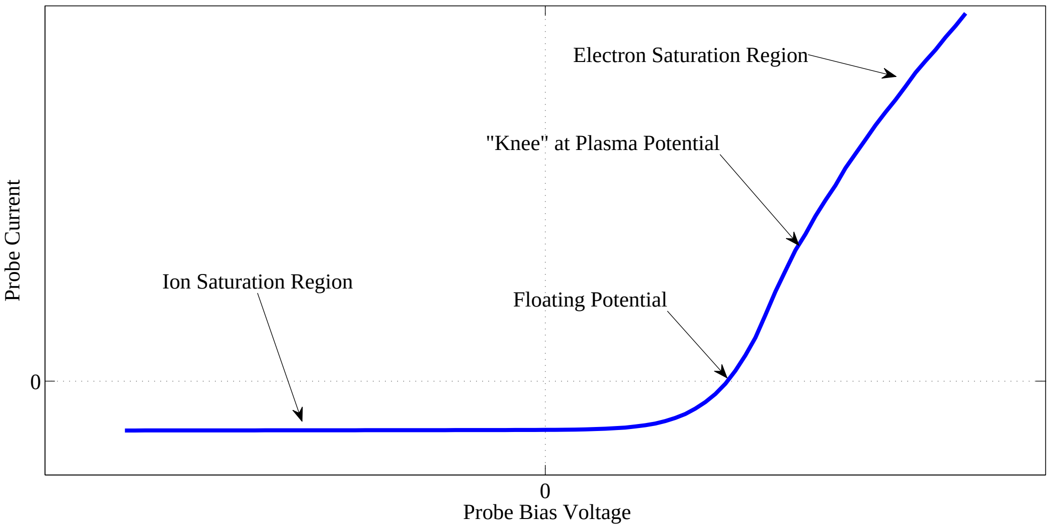

Figure 3.6. A typical Langmuir probe trace showing the features of interest.

influence on the Langmuir probe characteristic trace and its interpretation. In the figure the ion saturation current is exaggerated to make the floating potential clear.

For the small number of measurements taken with these Langmuir probes, the plasma potential and electron temperature were determined manually for each of the seven probes at the nominal H6 operating condition. The plasma potential was calculated by the usual technique of graphically finding the intercept between linear fits to the electron saturation and electron retarding regions on a semi-log plot of the I-V trace, and the electron temperature in eV was calculated as the inverse slope of the line through the electron retarding region.

One complicating factor for planar probes is the probe sheath expansion in ion saturation, increasing the effective probe area and inflating the measured ion saturation current. Unaccounted for, this effect can seriously alter calculated ion densities. Practically speaking, the best defense against this effect is a large probe such that sheath expansion can exert only a relatively small influence on the measured current density, and the large diameters of these probes help in that respect. In addition the sheath expansion model of Shastry[20] for flush-mounted Langmuir probes in a ceramic was also applied, which takes into account the local electron temperature and secondary electron emission yield of the surrounding ceramic material. This model was developed for use with tungsten probes in a boron nitride ceramic, but with the appropriate secondary electron emission yield for macor available from Dunaevsky it is straightforward to use here as well.[21]

[1] McDonald, M. and Gallimore, A., "Parametric Investigation of the Rotating Spoke Instability in Hall Thrusters," *32nd International Electric Propulsion Conference*, IEPC 2011-242, Wiesbaden, Germany, 2011.

[2] Hershkowitz, N., "How Langmuir Probes Work," *Plasma Diagnostics*, Academic Press, Boston, 1989, pp. 113–183.

[3] Reid, B. M. and Gallimore, A. D., "Langmuir Probe Measurements in the Discharge Channel of a 6-kW Hall Thruster," *44th AIAA/ASME/SAE/ASEE Joint Propulsion Conference & Exhibit*, AIAA 2008-4920, 2008.

[4] Janes, G. S. and Lowder, R. S., "Anomalous Electron Diffusion and Ion Acceleration in a Low-Density Plasma," *Physics of Fluids*, Vol. 9, 1966, pp. 1115.

[5] McDonald, M. S. and Gallimore, A. D., "Rotating Spoke Instabilities in Hall Thrusters," *IEEE Transactions on Plasma Science (to be published)*, 2011.

[6] Huang, W., Gallimore, A., and Smith, T., "Two-Axis Laser-Induced Fluorescence of Singly-Charged Xenon inside a 6-kW Hall Thruster," Jan. 2011.

[7] Ellison, L., Raitses, Y., and Fisch, N. J., "Fast Camera Imaging of Hall Thruster Ignition," *IEEE Transactions on Plasma Science*, 2011, (to be published).

[8] Huang, W., *Study of Hall Thruster Discharge Channel Wall Erosion via Optical Diagnostics*, Ph.D. thesis, University of Michigan, Ann Arbor, MI, 2011.

[9] Reid, B. M. and Gallimore, A. D., "Plasma Potential Measurements in the Discharge Channel of a 6-kW Hall Thruster," *44th AIAA/ASME/SAE/ASEE Joint Propulsion Conference & Exhibit*, AIAA 2008-5185, 2008.

[10] McDonald, M. S. and Gallimore, A. D., "Measurement of Cross-Field Electron Current in a Hall Thruster Due to Rotating Spoke Instabilities," *47th AIAA/ASME/SAE/ASEE Joint Propulsion Conference & Exhibit*, AIAA 2011-5810, 2011.

[11] Huang, W., Gallimore, A., and Hofer, R., "Neutral Flow Evolution in a Six-Kilowatt Hall Thruster," *Journal of Propulsion and Power*, Vol. 27, No. 3, 2011, pp. 553–563.

[12] Mikellides, I. G., Katz, I., and Hofer, R. R., "Design of a Laboratory Hall Thruster with Magnetically Shielded Channel Walls, Phase I: Numerical Simulations," *47th AIAA/ASME/SAE/ASEE Joint Propulsion Conference & Exhibit*, AIAA 2011-5809, 2011.

[13] Liu, D., Huffman, R. E., Branam, R. D., and Hargus, W. A., "Ultrahigh-Speed Imaging of Hall-Thruster Discharge Oscillations With Krypton Propellant," *IEEE Transactions on Plasma Science*, 2011.

[14] Mikellides, I. G., Katz, I., Hofer, R. R., and Goebel, D. M., "Hall-Effect Thruster Simulations with 2-D Electron Transport and Hydrodynamics Ions," *31st International Electric Propulsion Conference*, IEPC-2009-114, Ann Arbor, MI, 2009.

[15] Hofer, R., Mikellides, I., Katz, I., and Goebel, D., "Wall Sheath and Electron Mobility Modeling in Hybrid-PIC Hall Thruster Simulations," July 2007.

[16] Brown, D. and Gallimore, A., "Investigation of Low Discharge Voltage Hall Thruster Operating Modes and Ionization Processes," *31st International Electric Propulsion Conference*, IEPC 2009-074, Ann Arbor, MI, 2009.

[17] Darnon, F., Lyszyk, M., and Bouchoule, A., "Optical investigation on plasma investigations of SPT thrusters," Seattle, WA, 1997.

[18] Jameson, K., *Investigation of Hollow Cathode Effects on Total Thruster Efficiency in a 6-kW Hall Thruster*, Ph.D. thesis, University of California Los Angeles, Los Angeles, CA, 2008.

[19] Bouchoule, A., Philippe-Kadlec, C., Prioul, M., Darnon, F., Lyszyk, M., Magne, L., Pagnon, D., Roche, S., Touzeau, M., Béchu, S., Lasgorceix, P., Sadeghi, N., Dorval, N., Marque, J., and Bonnet, J., "Transient phenomena in closed electron drift plasma thrusters: insights obtained in a French cooperative program," *Plasma Sources Science and Technology*, Vol. 10, No. 2, May 2001, pp. 364–377.

[20] Shastry, R., Gallimore, A., and Hofer, R., "Experimental Characterization of the Near-Wall Plasma in a 6-kW Hall Thruster and Comparison to Simulation," July 2011.

[21] Dunaevsky, A., Raitses, Y., and Fisch, N. J., "Secondary electron emission from dielectric materials of a Hall thruster with segmented electrodes," *Physics of Plasmas*, Vol. 10, No. 6, 2003, pp. 2574.

[22] Hofer, R. R., Katz, I., Mikellides, I. G., Goebel, D. M., Jameson, K. K., Sullivan, R. M., and Johnson, L. K., "Efficacy of Electron Mobility Models in Hybrid-PIC Hall Thruster Simulations," 44th AIAA/ASME/SAE/ASEE Joint Propulsion Conference, Hartford, CT, AIAA-2008-4924, 2008.

[23] Shastry, R., *Experimental Characterization of the Near-Wall Region in Hall Thrusters and its Implications on Performance and Lifetime*, Ph.D. thesis, University of Michigan, Ann Arbor, MI, 2010.

[24] Jameson, K., Goebel, D., Hofer, R., and Watkins, R., "Cathode Coupling in Hall Thrusters," Florence, Italy, Sept. 2007, pp. IEPC 2007–278.

[25] Reid, B., *The Influence of Neutral Flow Rate in the Operation of Hall Thrusters*, Ph.D. thesis, University of Michigan, Ann Arbor, MI, 2009.

[26] Parker, J. B., Raitses, Y., and Fisch, N. J., "Transition in electron transport in a cylindrical Hall thruster," *Applied Physics Letters*, Vol. 97, No. 9, 2010, pp. 091501.

CHAPTER IV

Collisional Transport Modeling

> *"I am busy just now again on electromagnetism, and think I have got hold of a good thing, but can't say. It may be a weed instead of a fish that, after all my labour, I may at last pull up."*
>
> Michael Faraday, 1831

Recall from Chapter II that the mechanisms of electron transport can broadly be separated into collisional and turbulent transport mechanisms. This chapter focuses on qualitative estimates of near-field electron transport by collisional mechanisms, largely through development of an electron trajectory model to simulate the motion of large ensembles of electrons in the static electromagnetic fields of the H6 at its nominal 300 V, 20 mg/s operating condition.

There are two goals to the development of this model. The first is to determine whether results first obtained by Smith suggesting that collisions with the thruster pole pieces are sufficient to explain anomalous electron transport in the Stanford Hall thruster, a small, low-power thruster with an external cathode, also apply to the larger 6-kW H6 Hall thruster with its internal cathode.[5,18,25] The second goal is to better spatially resolve where anomalous mobility is present in the plume than has been previously possible, by observing where this model capable of only classical and collisional mobility fails to reproduce cross-field transport.

The results of this modeling have been that it is not possible to drive electrons into the channel given the experimentally observed static fields in the H6 through classical and collisional transport from either of two points in the near-field plume: directly from the cathode or directly in front of the thruster discharge channel at one discharge channel length downstream. This includes accounting for transport by binary plume collisions with neutrals and treating the thruster surface boundary conditions to allow for collisional transport by impact with exposed thruster surfaces in the near-field. While electron-ion collisions were not explicitly included due to a lack of full 2D maps of ion density, experimental collision frequencies are known for this reaction pathway in the region directly front of the H6 discharge channel and the neutral collision frequency was artificially inflated in a subset of simulations to account for the missing electron-ion collisions. Both reasonable increases in neutral density by a factor of 10 to account for the ion collisions and a large increase by a factor of 100 to account for uncertainties in measurements of both neutral and ion collision frequencies did not drive any increase in transport. Finally, as an experimental check the entire thruster body, pole pieces included, was isolated from chamber ground in an attempt to observe some effect on the thruster plasma by altering the boundary potentials on the poles. The potential of the normally grounded thruster poles dropped drastically to a floating potential over 30 volts below ground. Such a large change in the near-field thruster surface boundary condition was expected to increase total discharge current by keeping electrons that normally would have collided with the poles in the discharge, but only a very small change in thruster discharge current and no observable changes in thrust were observed.

The results of simulations in this chapter indicate that a) binary plume collisions are not a strong factor in electron transport in thruster operation in general in the near-field region, which is expected since these collisions fall under classical transport which has long been known to be insufficient, and b) that collisions with the thruster surfaces in the near-field given a static field configuration also do not contribute to cross-field electron transport in the near-field, which is in contradiction of the results reported by Smith. This second finding may indicate that near field thruster surface collisions are truly not an important effect in Hall thrusters, or that they are important only in a device of the type examined by Smith: small, low power, using an externally mounted cathode and with several other distiguishing features discussed in the chapter. It is possible that even if this mechanism does normally play a strong role in collisional transport in the H6, that when it is suppressed or enhanced by biasing the thruster pole pieces the other transport mechanisms are sufficiently robust or flexible that the plasma conditions adapt to maintain stable operation. The simpler explanation is that this mechanism is not a significant part of near-field electron transport in the H6.

This chapter first presents the a broad description and the motivation for the creation of the code, including a review of the earlier work in this area by Smith. A detailed description of the model may be found in Section 4.2. The simulation results and related experimental results are presented in Sections 4.3 and 4.4, respectively.

4.1 Model description and motivation

The electron model, dubbed “MCHall” for *M*onte *C*arlo *Hall* thruster model in a nod to the well-known HPHall simulation code, is at its heart is an integrator for the electron equations of motion. MCHall accepts input meshes for electric and magnetic fields and particle density maps, uses a Boris integrator to track electrons seeded from a half-Maxwellian distribution, and treats binary plume collisions with neutrals in a Monte Carlo fashion. The development of MCHall was heavily motivated by the work of Smith discussed in Section 2.4.2.2, in particular the notion of modeling electron transport in the near field using experimentally measured fields as static inputs. By definition experimental measurements will include contributions to the overall field structure produced by all forms of electron transport, including turbulence. Fluctuations due to turbulence will be averaged out, but increased transport between different regions due to the presence of turbulence may affect the potentials throughout the plume. As a result, while MCHall simulates classical or collisional turbulent mechanisms, it does so in a static field profile that includes contributions of turbulent and any other anomalous sources present in the real Hall thruster discharge.

Smith's results reproduced realistic fractions of electrons emitted from the cathode reaching the discharge channel, about 10-20%, without the imposition of either time-resolved turbulent fields or binary plume collisions – transport was achieved solely by inclusion of collisions between electrons and the sheath over the thruster pole pieces, with no observed sensitivity to the specular or diffuse character of the collisions.

A second motivation for direct electron modeling was the hope of localizing by elimination which regions in the plume require turbulent transport mechanisms. The trend in Hall thruster modeling has been to treat anomalous mobility coefficients in ever greater resolution, and each step has provided new insights. The early models of Fife used a single factor to characterize the entire plume; later efforts by Koo, Garrigues and Hofer treated the discharge channel plasma independently from the plume plasma with two factors.[3,6,7,14] Hofer later extended this discretization to three factors, one each for the deep channel, acceleration region and near-field.[21] Since development of MCHall began, Mikellides has extended the flexibility of the anomalous mobility further by modeling it as a continuous function.[11,13] It has become increasingly clear across all of these hybrid and eventually full fluid models that the near-field is the region where anomalous transport is most required. It seemed possible that the necessary near-field anomalous transport mechanism might be the collisions with the thruster near-field directly modeled in electron trajectories by Smith but not captured in other models.

Still, the near-field extends radially as well as axially, and in particular with the use of the internal cathode there are a wide variety of plasma conditions in the near-field. It is not clear whether we should be looking near the cathode, downstream of the discharge channel, over the pole pieces, elsewhere or all of the above for anomalous electron mobility. MCHall is a relatively simple tool that can be used to drop electrons anywhere in the plasma and see where they go, without explicitly having to model ion and neutral behavior or enforce self-consistent field formulations. As a result, MCHall can simulate large numbers of electrons traveling through the H6 very quickly.

Directly modeling electron trajectories is also appealing as a way to build a sense of physical intuition for the behavior of charged particle trajectories in the very complex fields of a real Hall thruster. For example, King's modeling of electron trajectories in the channel of the NASA 173Mv1 Hall thruster showed that the classic picture of closed electron $\mathbf{E} \times \mathbf{B}$ drift in purely radial magnetic and axial electric fields described by Jahn is an oversimplification, and demonstrated features like the characteristic radial bounce frequency of electrons between the channel walls and the

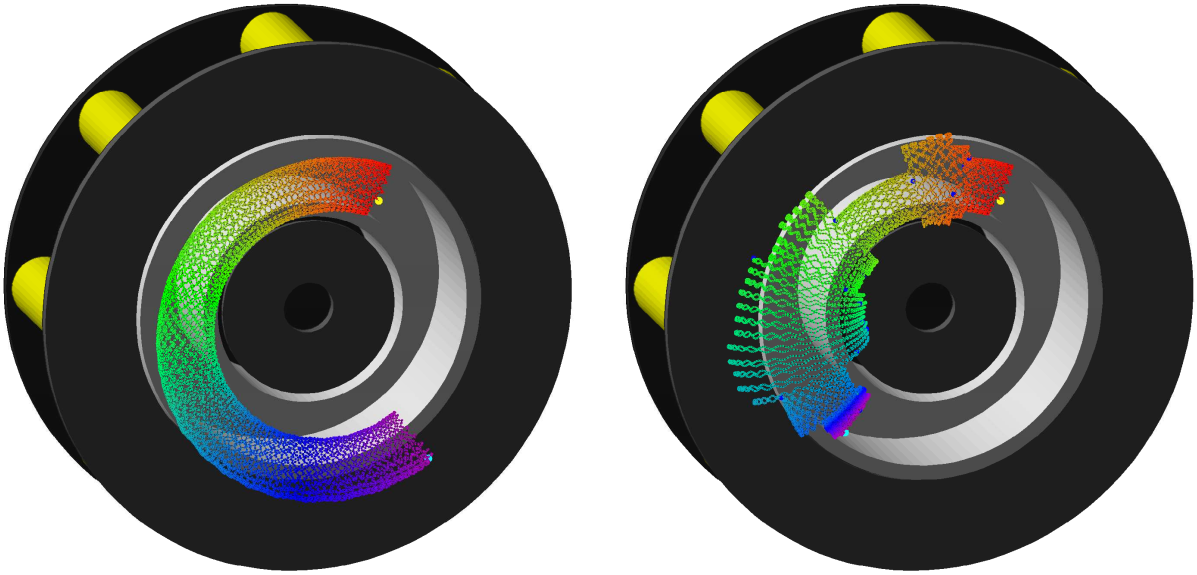

Figure 4.1. Two cases of electron trajectories with duration 1 μs seeded on channel centerline, one discharge channel length forward of the exit plane, with 2.5 eV initial energy. Left, a collisionless orbit rotates in the E × B direction about 2/3 of the way around the thruster in a repetitive fashion. Right, when the effects of electron-neutral collisions (large blue dots) are included, the regularity of the orbit is broken and the electron may penetrate further toward the poles when its velocity vector aligns with the local magnetic field. Both orbits are color-coded from red at the beginning of the orbit to violet at the end. A yellow dot notes the beginning of the orbit, a light blue dot the end, and dark blue dots note electron-neutral collisions.

importance of radial electric field components to maintain the closed drift orbit.[2,12]

The picture is similarly complex in the near-field, where even electrons in relatively bound configurations may have an orbit that spans over a large portion of the plume, calling into question whether and which local properties should be used to describe it. Figure 4.1 shows an electron on the left seeded with an initial energy of 2.5 eV from one discharge channel length in front of the exit plane in the H6. In the near-field the radial bouncing between channel walls described by King becomes a bounce over the channel exit between the inner and outer poles, with the restoring force provided by a magnetic mirror and electric field on the inside and an electric field alone on the outside.

This is the case for a collisionless orbit; accounting for collisional scattering complicates matters further. The right image in Figure 4.1 demonstrates the effects of collisions on an orbit by assuming hard-sphere scattering when the electron collides with neutrals during its orbit. The method and source data for modeling these collisions are discussed later in the chapter; for now it is sufficient to notice that the collisions can scatter the electron into widely different parts of the plasma, albeit along the same or adjacent magnetic field lines. These orbits are already far more complex than the simple pictures of an electron diving into the channel shown in the beginning of Chapter II. The real trajectories when the thruster operates are more complex still, since the plasma sustains a rich variety of oscillations and the azimuthal uniformity assumed so far is no longer valid. Ultimately to understand electron transport in Hall thrusters it will probably be useful to understand the limits to the simple depictions of electron orbits we use to make sense of how these devices operate.

4.1.1 Trajectory Simulations by Smith

Smith's electron trajectory modeling may be found in a series of papers beginning in 2006.[5,18,25] In the most recent results from 2010, Smith uses a Runge-Kutta 4th order integrator to calculate an ensemble of 10^6 electron trajectories through the plume of the Stanford Hall Thruster, a 82 mm channel diameter thruster operated in this case at 200 V and 2.6 A and that in general has been run over a range of operating points from 200-500 W.[27] Electrons are seeded from an externally mounted cathode angled in at 45° toward thruster centerline, with a Maxwellian distribution about a temperature of 1000 K and an angular emission distribution from the cathode that is Gaussian with a standard deviation of 30 degrees. The electrons are then given an additional "kick" in their chosen direction with magnitude equal to the local plasma potential of 10 eV.

The simulation reproduces a reasonable amount of backstreaming electron current, about 10% of the total discharge current, without the introduction of any anomalous transport coefficients or time-varying fields that might induce turbulent transport. The population of electrons that make it to the channel (channel-bound) experience on average a thousand times more collisions with the thruster surface than those that leave the simulation domain (plume-bound). The sheath over thruster surfaces is modeled as a fixed 15 V potential drop with a thickness of 1 mm, based on an assumption of a 5 eV temperature near the poles. Those electrons that penetrate the sheath are re-emitted from a Maxwellian distribution with temperature 500 K, the estimated temperature of the thruster poles, in a random direction (i.e.,diffuse colisions). The effect of specular collisions, where the axial component of the velocity vector is simply reversed in sign upon collision, was also considered but had minimal effect on the results. The exposed thruster surfaces are bare iron but are left floating, and shorting (i.e., grounding) the thruster surface dramatically alters thruster operation.[28]

The point of greatest interest in the simulation is the enormous effect of interaction with the thruster surfaces on the overall transport. While binary plume collisions with neutrals were not considered in the bulk of Smith's simulations, they were noted to produce little effect in teh cases where they were considered. The thruster surfaces were the primary contributor to the cross-field transport. If these results could be reproduced it would indicate that collisional transport with the thruster surfaces may play a large role in explaining the electron transport problem. It would also obviate the need for high-speed measurements of thruster properties to help with predictive models, since the transport appears to function even in static field configurations.

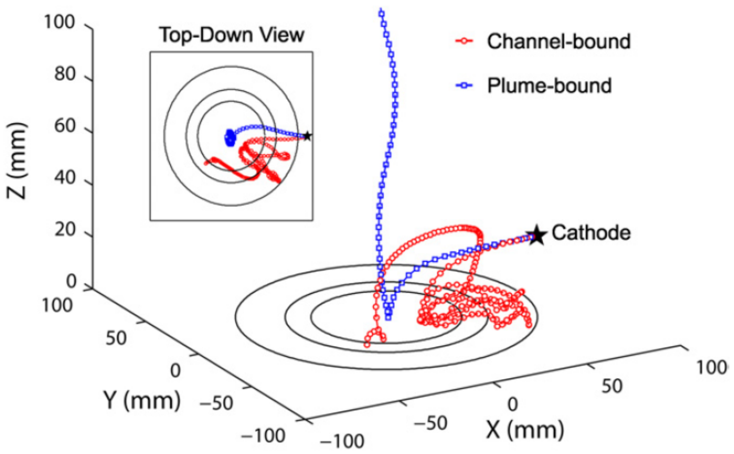

Figure 4.2. Electron trajectory simulations by Smith show realistic levels of backstreaming electron current into the discharge channel. The key difference between channel-bound (red) and plume-bound (blue) electrons is the large number of collisions with the thruster surfaces experienced by the channel-bound electrons. On average, Smith finds these electrons to experience ~10^3 more surface collisions than plume-bound electrons. Figure reproduced from Smith.[18]

4.2 Model Details

4.2.1 Simulation Domain and Experimental Fields

The MCHall simulation domain is determined by the availability of experimental maps of the H6 thruster plasma potential and, to a lesser extent, neutral density in the near-field plume. The domain extends 1.75 thruster mean channel radii radially and 2.6 radii in the axial direction. The electric field is prescribed by the discrete gradient of plasma potential measurements made by Jameson using floating emissive probes corrected for electron temperature.[19] These maps were obtained by several radial sweeps at widely spaced axial locations, and are numerically interpolated to the desired resolution before taking the gradient. The neutral density is also from Jameson, using relative densities obtained via optical measurements and scaled to absolute values using neutral density estimates from HPHall. The magnetic field is obtained from a finite element simulation in Infolytica's commercial MagNet software package.

The magnetic field simulation takes into account only the vacuum field configuration, neglecting any self-fields caused by the currents within the plasma during operation. Previous work has shown that the magnitudes of the self-fields are small in the channel compared to the static field set up by the magnetic circuit.[16] Both the electric and magnetic field are specified on a 1 mm mesh, and on each timestep the local fields at the electron position are bilinearly interpolated from the values at each corner of the current mesh cell. To speed computation time, this bilinear interpolation is expressed in matrix form as

$$f(x,y) = \frac{1}{(x_2-x_1)(y_2-y_1)} \begin{bmatrix} x_2 - x & x - x_1 \end{bmatrix} \begin{bmatrix} f(x_1,y_1) & f(x_2,y_1) \\ f(x_1,y_2) & f(x_2,y_2) \end{bmatrix} \begin{bmatrix} y_2 - y \\ y - y_1 \end{bmatrix} \tag{4.1}$$

where x and y are assumed to lie between (x_1, x_2) and (y_1, y_2), respectively. By defining the input meshes at the same size and resolution, the first, second and fourth terms on the RHS of this equation need only be evaluated once for both fields. The particle densities are not nearly as sensitive to accurate interpolation since they figure only probabilistically into the Monte Carlo process and so they are interpolated with a simpler nearest-neighbor scheme.

4.2.1.1 Treatment of boundary conditions

Boundary conditions apply in theory both at the thruster surfaces and in the far field. In practice only the thruster surface boundary conditions are needed and any electron reaching the edge of the simulation domain is assumed lost permanently. Near-field boundaries include the thruster pole pieces and keeper in the spatial domain and the source condition for electron energy and angle of emission from the cathode in the time domain.

The plasma potentials from Jameson in the H6 thruster plume are only available beginning at $z = 0.75$ cm in front of the thruster exit plane, creating a gap in the dataset near the thruster pole pieces. In the H6 the exit plane is defined as the axial location flush with the end of the boron nitride discharge channel, which is a few millimeters downstream of the pole pieces, so the gap with unresolved plasma behavior in front of the thruster surfaces is over a centimeter. Over this span the potential drops from several to tens of volts down to zero at the exposed metal pole pieces where the thruster is grounded. Since MCHall is intended to resolve the influence of collisions with the thruster surfaces on electron transport, I characterized this high-gradient region further using flush-mounted Langmuir probes on the pole pieces. These probes resolve the plasma potential, density and electron temperature 3 mm in front of the pole pieces at 3 radial locations on the inner pole and 4 radial locations on the larger outer pole.

The probes demonstrate that even very close in front of the inner pole, the plasma potential is relatively high, while at the outer pole the potential is relatively close to ground already. This fits with the picture hinted at in Jameson's data; both those measurements at the $z =$7.5 mm axial position and the measured plasma potentials with the Langmuir probes are shown in Figure 4.3.

The electron temperatures and densities measured by the probes give a Debye length in this region $\lambda_D \leq 0.3$ mm. The axial position of the pole probes at 3 mm forward of the pole pieces may then be thought of as more of a pre-sheath condition. However, no attempt at a detailed sheath model is made in MCHall; instead the measured plasma potentials from the Langmuir probes are inserted into the mesh at the $z = -1$ mm axial location at the appropriate radial locations. The potential from the innermost and outermost probe on each pole to the edge is assumed constant, and a piecewise cubic polynomial is interpolated between the probes. The grounded pole potential is applied along the poles at $z = -4$ mm. Practically speaking, this does not affect the simulation results. While significant attention was paid to acquiring accurate data to simulate this region, the baseline and channel-seeded MCHall simulation discussed in Section 4.3 found that no electrons collided with or even came near to the $z = -1$ mm axial location of the pole probes, much less the sheath over the pole pieces.

It is much more difficult to model the cathode orifice region accurately due to the small physical dimensions in this area and the poor spatial resolution of existing data. The measured cathode floating potential of -9.75 V during nominal operation, slightly below the plasma potential in the cathode plume measured by Jameson. Since Jameson's data does not quite extend to centerline, the centerline plasma potential is assumed equal to the measured value closest to centerline to force a smooth derivative over the line of symmetry (not shown). The keeper floats a few volts several volts above the cathode floating potential at -6.4 V. It is difficult to use these two values to estimate an orifice electron temperature because the cathode floating potential is the potential at the insert, deep inside the cathode, and the keeper is physically large and makes contact with the plasma both inside and outside so it likely floats at a potential proportional to a spatial average of electron temperatures in this region.

The orifice potential at which the electrons are seeded is taken to be the cathode floating potential plus the Maxwellian electron temperature T_e= 2 eV discussed in the next section. The sheath potential in front of the floating keeper is calculated as[17]

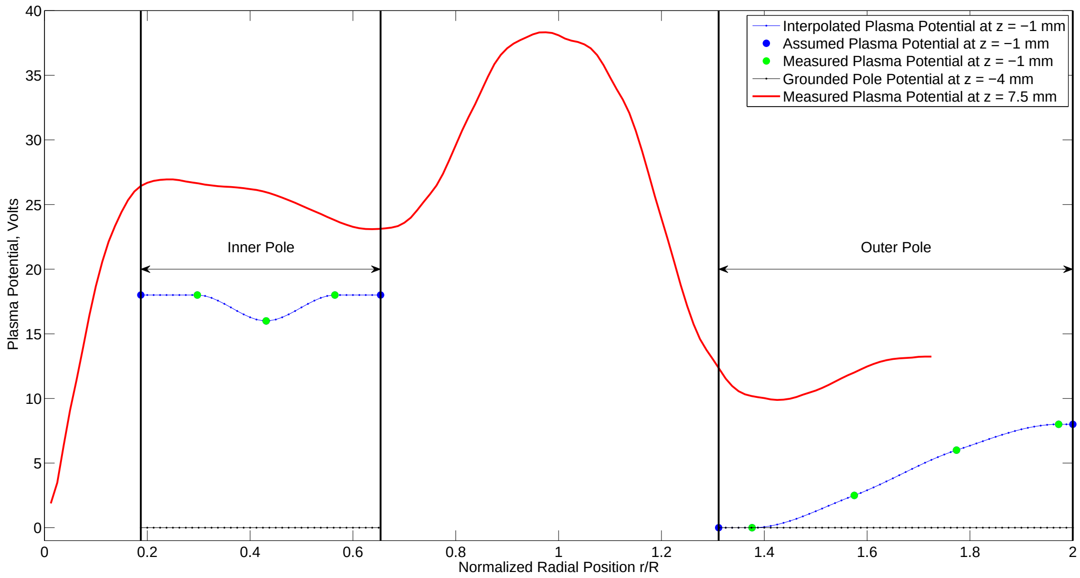

Figure 4.3. Plasma potential measurements in the H6 very near-field plume at nominal operation in the very near field from Jameson[19] at $z = 7.5$ mm (red) using emissive probes and at $z = -1$ mm from this work using flush-mounted Langmuir probes (green). The interpolated plasma potential used in the field mesh for MCHall is shown in blue. The large blue dots represent an assumed constant potential between the inner and outermost probes on each pole and the pole edges.

$$V_{sheath,kpr} = V_{kpr} + T_e ln\left(\frac{m_i}{2\pi m_e}\right) \tag{4.2}$$

and an arbitrary sheath thickness of 0.1 mm is imposed. The cathode region plasma conditions in MCHall are shown in Figure 4.4. The final field meshes used as inputs for MCHall for V_p, B and n_n are shown in Figure 4.5.

4.2.2 Electron Trajectory Integration Method

The particle mover is the *sine qua non* of this type of simulation. Without an effective integrator for the charged particle equations of motion the electrons are prone to spurious numerical heating and require such short timesteps to maintain energy conservation that simulation times become prohibitively long. For this work the leapfrog Boris algorithm with an adaptive timestep is used. Since MCHall is

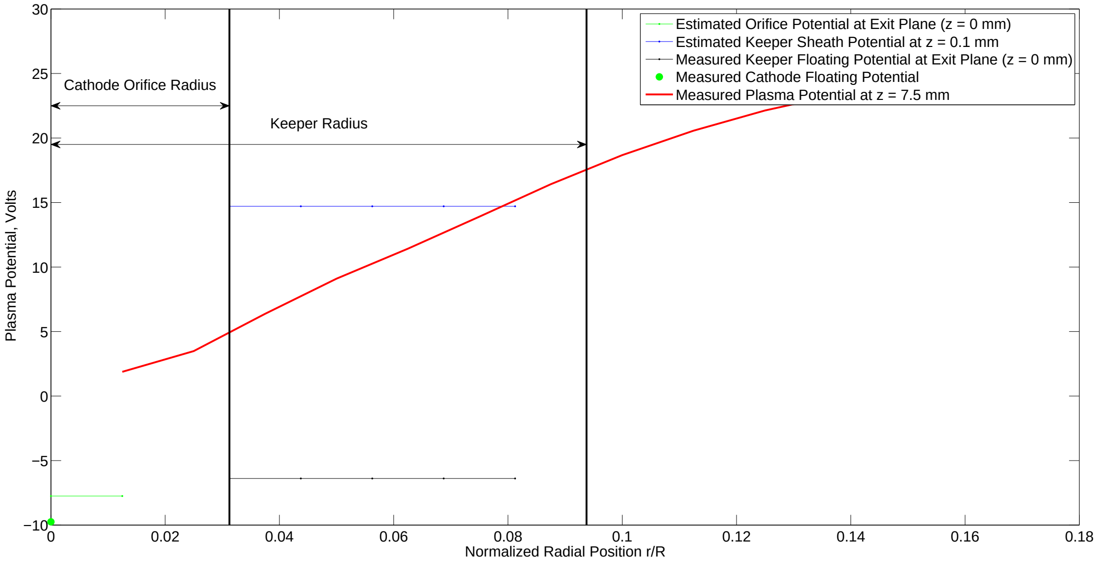

Figure 4.4. Cathode region plasma potentials enforced in MCHall. This region suffers from coarse resolution due to its small physical size. Measured floating potentials of the cathode and the keeper form the basis for most of the conditions in this region. [Note: For some reason outermost radial plot points did not show up; correct this]

written in MATLAB, a vector-based implementation of the algorithm is implemented following the development in Birdsall.[20]

Given the electron's differential equations of motion,

$$\mathbf{a}(t) = -\frac{e}{m}\left(\mathbf{E} + \mathbf{v} \times \mathbf{B}\right) \tag{4.3}$$

$$\mathbf{v}(t) = \frac{d\mathbf{r}}{dt} \tag{4.4}$$

where e is the fundamental unit of charge and the negative sign represents the negative charge of the electron, the Boris algorithm numerically integrates the electron trajectory using a staggered leapfrog scheme that cleverly decomposes the force on the electrons into purely electric "drift" steps and purely magnetic "kick" steps. In the staggered leapfrog scheme the position $\mathbf{r}$ at time t are related to the velocity $\mathbf{v}$

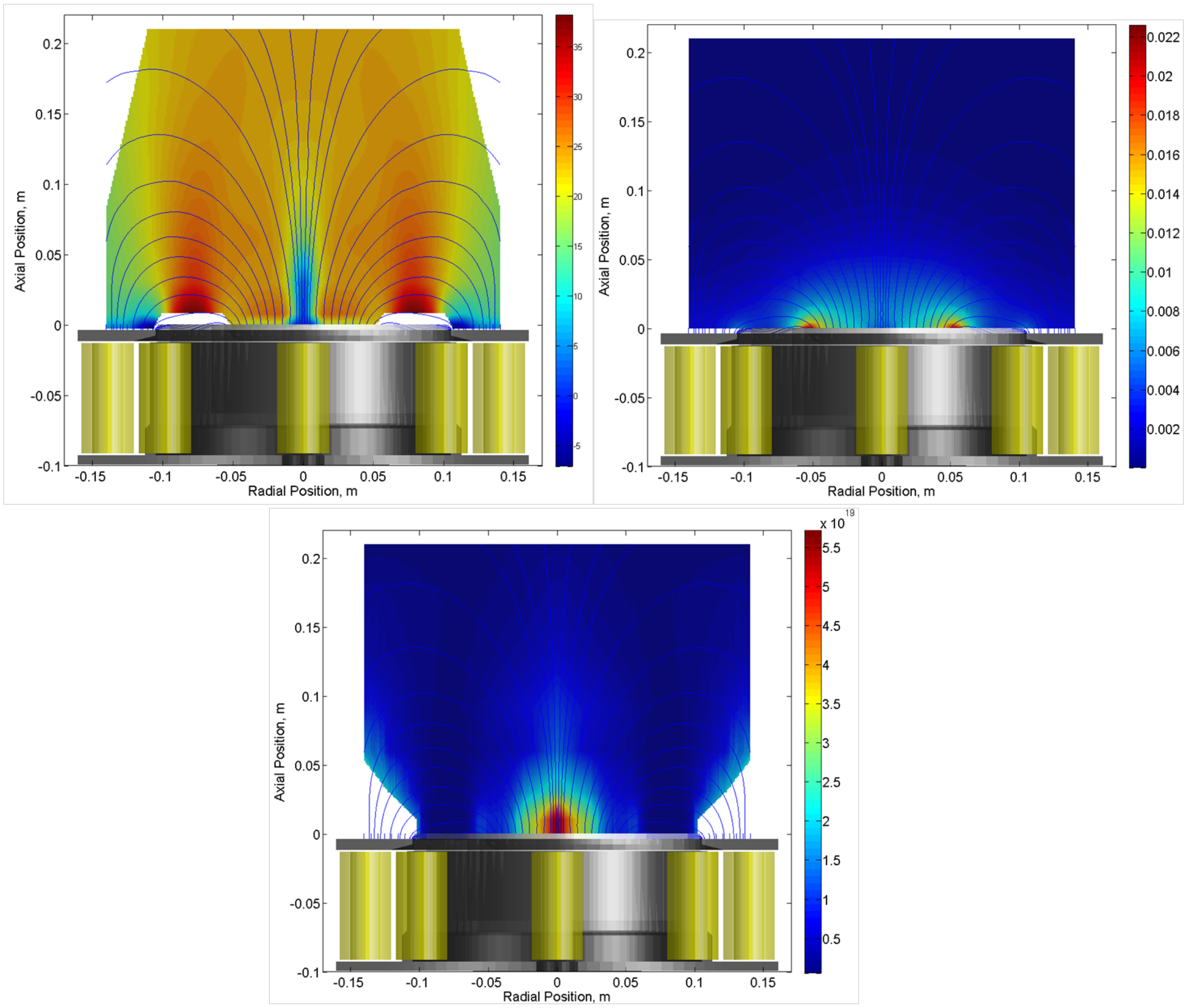

Figure 4.5. Field inputs from left to right for plasma potential (Volts), magnetic field strength (Tesla) and neutral density (m^{-3}) used in MCHall. Magnetic field streamlines are shown overlaid on all plots.

at intermediate timesteps $t + \Delta t/2$ and $t + -\Delta t/2$ as

$$\begin{aligned} \mathbf{r}_{t+\Delta t} &= \mathbf{r}_t + \mathbf{v}_{t+\Delta t/2}\Delta t & (4.5) \\ \mathbf{v}_{t+\Delta t/2} &= \mathbf{v}_{t-\Delta t/2} - \frac{e}{m}\left(\mathbf{E} + \mathbf{v}_t \times \mathbf{B}\right)\Delta t & (4.6) \end{aligned}$$

where for compactness we define $\mathbf{r}_t \equiv \mathbf{r}(t)$. Evaluation of $\mathbf{v}_{t+\Delta t/2}$ in Eqn. (4.6) requires some subtlety due to the inclusion of $\mathbf{v}_t$ in the Lorentz force term. The simplifying insight first suggested by Buneman is to approximate the velocity symmetrically about the current time as

$$\mathbf{v}_t \approx \frac{\mathbf{v}_{t+\Delta t/2} + \mathbf{v}_{t-\Delta t/2}}{2} \tag{4.7}$$

This method maintains time reversibility of the model, a property discussed in more detail by Buneman.[8] While this is no longer strictly true when Δt varies from one timestep to the next, as when using an adaptive timestep, in practice there were no observable effects on energy conservation between a fixed timestep on the order of the smallest adaptive timestep in a given electron's orbit vs. the use of the adaptive timestep. Substitution in Eqn. (4.6) yields the implicit expression

$$\mathbf{v}_{t+\Delta t/2} = \mathbf{v}_{t-\Delta t/2} - \frac{e\Delta t}{m}\left(\mathbf{E} + \frac{1}{2}\left(\mathbf{v}_{t-\Delta t/2} + \mathbf{v}_{t+\Delta t/2}\right) \times \mathbf{B}\right) \tag{4.8}$$

The key to the Boris technique is to use intermediate velocities $\mathbf{v}^-$ and $\mathbf{v}^+$to separate the electric and magnetic forces completely. Substituting

$$\mathbf{v}_{t-\Delta t/2} = \mathbf{v}^- - \frac{e\mathbf{E}}{m}\frac{\Delta t}{2} \tag{4.9}$$

$$\mathbf{v}_{t+\Delta t/2} = \mathbf{v}^+ + \frac{e\mathbf{E}}{m}\frac{\Delta t}{2} \tag{4.10}$$

into Eqn. 4.8 yields an expression where $\mathbf{E}$ cancels entirely, leaving only a rotation (the "kick") due to $\mathbf{B}$:

$$\frac{\mathbf{v}^{+} - \mathbf{v}^{-}}{\Delta t} = \frac{e}{2m}\left(\mathbf{v}^{+} + \mathbf{v}^{-}\right) \times \mathbf{B} \tag{4.11}$$

For efficient vector implementation the intermediate vector $\mathbf{v}'$ bisecting $\mathbf{v}^{+}$ and $\mathbf{v}^{-}$ is defined as

$$\mathbf{v}' \equiv \mathbf{v}^{-} + \mathbf{v}^{-} \times \mathbf{t} \tag{4.12}$$

$$\mathbf{t} \equiv \frac{e\mathbf{B}}{m}\frac{\Delta t}{2} \tag{4.13}$$

where the vector $\mathbf{t}$ represents the rotation due to the magnetic field in a half timestep by $\omega_c \Delta t/2$ in vector form. Then

$$\mathbf{v}^{+} = \mathbf{v}^{-} + \mathbf{v}' \times \mathbf{s} \tag{4.14}$$

$$\mathbf{s} \equiv \frac{2\mathbf{t}}{1 + t^2} \tag{4.15}$$

In practice, the leapfrog method is not self-starting, and given an initial condition $\mathbf{r}_0$ and $\mathbf{v}_0$ a half-step backwards in $\mathbf{v}$ is needed to generate $\mathbf{v}_{-\Delta t/2}$ to kickstart the leapfrog process.

Other integrators were also considered for this work, including a direct linear algebraic solution of the equations of motion following the initial method of Smith in[25], and an embedded 4th-5th order Runge-Kutta method. Both methods were too time-consuming without sufficient benefit in energy conservation.

To resolve the electron cyclotron motion efficiently, the electron trajectory is calculated with an adaptive timestep based on the local cyclotron frequency such that $\omega_c \Delta t \ll 1$. Choosing a timestep proportional to $1/\omega_c$ resolves trajectories well in high-field regions where the electron velocity vector rotates appreciably over short intervals without forcing a short, fixed maximum timestep across the entire simulation. For the simulations presented, a timestep equal to a constant fraction of the local cyclotron frequency $\omega_c \Delta t = 10^{-3}$ is used. This value was selected based on energy conservation grounds for long-lived electrons confined in the Hall current in front of the Hall thruster channel.

No maximum timestep is implemented in MCHall, but a maximum physical step size of 0.5 mm is enforced to prevent electrons from nonphysically gaining energy by accelerating due to a high electric field over a distance longer than that field is valid. This is particularly of concern for secondary electrons born with zero velocity in strong electric field regions with low B – for example, downstream on thruster centerline. A simple predictor / corrector scheme enforces the maximum step size by comparing the timestep and velocity magnitude after each Boris $\mathbf{v} \times \mathbf{B}$ integration. When the step size is too large, the timestep is reduced and, in the case of the corrector step, the timestep is resimulated.

For the special case in the H6 of a center-mount cathode and axisymmetric fields, a 2D simulation could suffice. Since the cathode centerline and thruster centerline coincide in this arrangement, it is possible to specify all thruster field properties independently of the azimuthal angle θ. However, the 3D formulation of MCHall permits the introduction of azimuthal perturbations on the axisymmetric fields, and holds out the possibility for future simulations of non-axisymmetric external cathode operating conditions.

4.2.3 Electron Sourcing

MCHall treats the cathode as a point source on thruster centerline, seeding electrons in a half-Maxwellian distribution with an experimentally guided energy. The source type is chosen to be a point instead of a more realistic disk, reflecting the finite sized cathode orifice, because the poor resolution of the plasma potential in the orifice region produces more significant errors for trajectories seeded from off cathode centerline.

The source electron energy is taken from measurements in the orifice region of a lanthanum hexaboride (LaB6) hollow cathode like the one used in the H6 by Goebel.[?] Rapidly injected probes measured an orifice electron temperature of about 2 eV while running at 25 A on 10 sccm of xenon, similar to the 20 A, 14 sccm cathode flowrate at the nominal H6 operating condition.

The half-Maxwellian source distribution is based on calculations of the mean free path at the cathode orifice that indicate a collisional flow regime. Following the technique given by Goebel for calculating the pressure in the orifice region of a cathode,[10] the upstream orifice pressure P may be computed as

$$P \approx \left(\frac{1.794 \times 10^{-4} Q l \left(\frac{T}{T_0}\right)^{1.71 + 0.29 \frac{T_0}{T}}}{d^4} \right)^{\frac{1}{2}} \tag{4.16}$$

where P is in torr, T is the gas temperature in Kelvin, $T_0 \equiv 289.7$ K, d and l are the length and diameter of the cylindrical orifice section in centimeters, and Q is the cathode flowrate in sccm. For the H6 cathode at a 14 sccm flowrate with an assumed gas temperature of 4000 K and approximate values $d = 0.25$ cm and $l = 0.1$ cm, the upstream orifice pressure is 2.5 torr. This formula is not exact, since the orifice is not perfectly cylindrical, the finite downstream pressure is neglected, and the gas temperature is not known exactly, but varying these quantities does not significantly change the pressure. The neutral density at this pressure is $n_n = 6 \times 10^{21}$ m^{-3}, for an electron-neutral collisional mean free path for a 2 eV electron of $\lambda_{mfp_{en}} \equiv 1/(n_n \sigma_{en}) = 0.5$ mm.

In a half-Maxwellian distribution, electron velocity unit vectors are scattered uniformly over a hemisphere of solid angle. A uniform distribution over the hemisphere of solid angle requires more electrons be seeded at large polar angles than along the cathode centerline. This dependence is given by the sine term in the expression for the differential unit of solid angle

$$d\Omega = sin\left(\phi\right) d\phi d\theta$$

where ϕ is the polar angle from the shared cathode and thruster centerline and θ is the azimuthal angle.

The energies E in eV are chosen for the electron temperature T_e =2 eV according to the Maxwellian distribution

$$f\left(E\right) = 2\sqrt{\frac{E}{\pi}}\left(\frac{1}{kT}\right)^{3/2} exp\left(\frac{-E}{kT}\right) \tag{4.17}$$

Energy isotropy is assumed since the same EEDF is distributed across all emission angles, and the velocity is calculated from the 2 eV electron temperature as $v = \sqrt{2eE/m}$, where again E is in eV.

In this manner, electrons are seeded with energy and spatial distributions as shown in Figure 4.6.

4.2.4 Collision Modeling

Collisions in MCHall are modeled probabilistically with the Monte Carlo method using the electron collision frequency at each timestep. The electron collision fre-

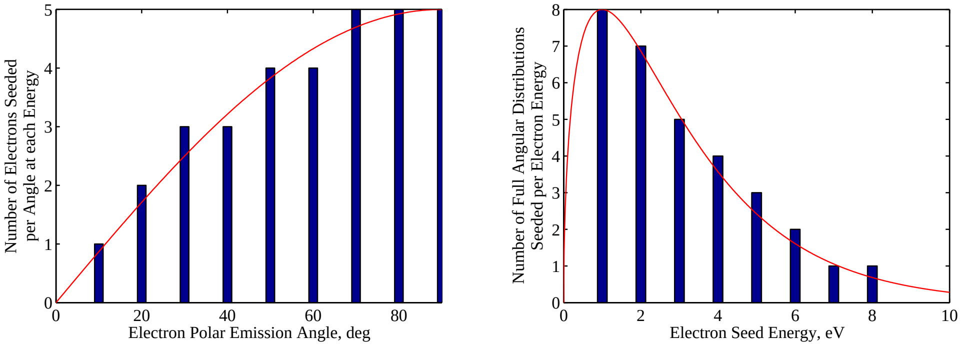

Figure 4.6. Sourcing distributions in polar angle (left) and energy (right). The analytic expressions for uniform angular seeding and Maxwellian energy distributions are shown in red, while the blue bars show the discrete approximations to these functions actually used when seeding electrons in MCHall. The pictured distribution would seed about 1000 electrons; the full angular distribution of 32 total electrons at left is seeded with each of the 32 energy levels at right.

quency ν is defined as

$$\nu = n\sigma v \tag{4.18}$$

where n is the density of the target species, σ is the collision cross section with the target species, and v is the velocity relative to the target species. In practice electrons move so much faster than anything else in the plasma that v is assumed to just be the electron velocity.

Four types of electron collisions can take place in a Hall thruster: electron-electron, electron-ion, electron-neutral, and electron-wall. The first type of collision is ignored for the purposes of modeling cross-field transport. As Chen notes, *"collisions between like particles give rise to very little diffusion"* since their guiding centers are either unaffected in head-on collisions or, in the worst case scenario, impact at right angles such that the guiding centers scatter in opposite directions without net transport.[4]

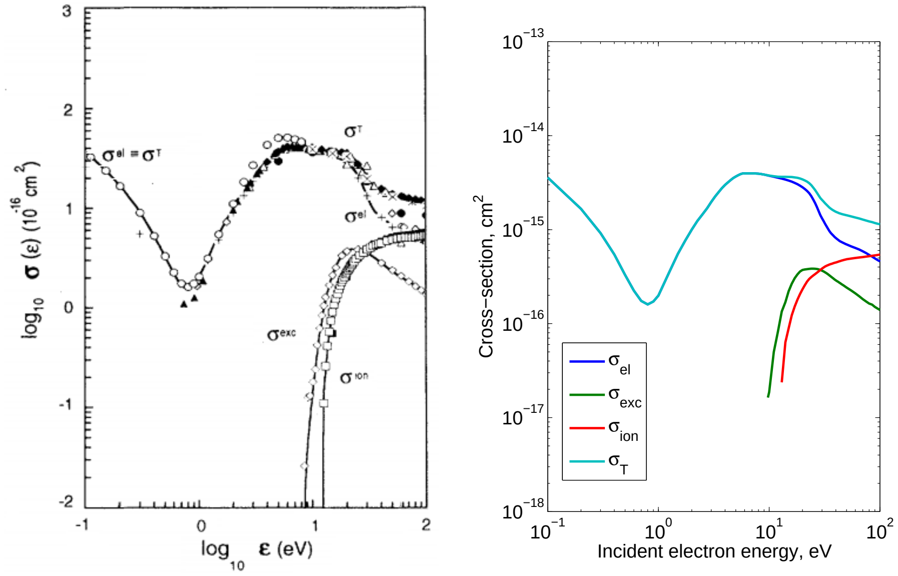

Figure 4.7. Left, compiled electron-neutral cross sections for momentum transfer, ionization and excitation from Dias.[15] Right, the re-sampled versions of these cross sections used in MCHall.

4.2.4.1 Elastic Neutral Scattering Collisions

The electron-neutral xenon cross section has been the subject of a number of experimental investigations. cross sections as a function of energy are available from a variety of sources; the work of Dias[15] is an excellent reference that compiles a large amount of this data. Cross sections for the several collision pathways discussed in the next few sections are plotted together in Figure 4.7. Momentum transfer collisions with neutrals dominate up to electron energies of 20-30 eV, at which point ionization collisions take over. Only the excitation to the 6p state has an appreciable contribution to the total cross section; the other excitation pathways are much smaller and are ignored.[22]

Recent modeling of the H6 in HPHall uses the data of Nickel[9] on total electron-neutral cross sections to generate Maxwellian-averaged cross sections as a function of temperature, i.e., an average value generated over an entire Maxwellian distribution suitable for use in equations describing a Maxwellian electron fluid. The Maxwellian-averaged cross section used in HPHall is not suitable for MCHall's particle-based approach, but the total cross sections of Nickel are among those collected in the plot by Dias in 4.7 and used in MCHall.

Relative neutral density measurements in the H6 near-field plume have been reported by Jameson[19]; the relative densities are scaled to absolute values in MCHall by matching to HPHall simulation outputs on channel centerline for matching H6 operating conditions.

4.2.4.2 Inelastic Neutral Ionization and Excitation Collisions

In addition to elastic scattering collisions, an electron can also inelastically ionize or excite an atom. This is particularly important as ionizing collisions release an extra electron into the plasma. These cross sections are also pulled from the compilation of experimental cross sections by Dias.

In the code secondary electrons from ionization are registered as they are created and subsequently tracked in addition to the primary electrons from the cathode. This implementation is recursive, such that secondary electrons can create and register tertiary electrons, and so on. Secondary electrons are seeded at rest from the position of the ionizing collision. Secondary electron tracking is important because, given the approximate 80% / 20% balance of plume-bound / channel-bound electrons, each channel-bound electron in the 20% must generate 3 additional channel-bound electrons on average either directly by ionization or indirectly through its ionization-born descendants in order to maintain current continuity. While much of that ionization surely occurs in the discharge channel, some may occur in the near field as well, and since the secondary electrons effectively are electrons that get "free passage" across the magnetic field to their birthplace they should not be overlooked.

4.2.4.3 Ion scattering collisions

Electron-ion scattering collisions are not explicitly modeled in MCHall due to the lack of full experimental maps of plasma density throughout the plume to accompany the plasma potential and neutral density. However, the effects of an increased electron collision frequency in front of the channel due to Coulomb scattering is addressed by inflating the neutral density in Section 4.3. This section discusses the Coulomb scattering process, reviews experimental measurements of ion density and electron temperature by Reid[1] on channel centerline, and uses these values to estimate a conservative or worst-case factor of 100 by which to inflate the neutral density in order to account for any additional scattering through this pathway. The ratio ν_{ei}/ν_{en} is about 4-5 over the first channel length downstream of the exit plane, and peaks at about 30 further downstream, so a factor of 100 includes a fair margin for error in these estimates to make sure this transport mechanism is accounted for fully.

Electron-ion collisions are mediated by the long-range Coulomb force, and as a result are generally gradually deflected through small angles over large distances compared to the sudden billiard-ball style collisions between electrons and neutrals. Nevertheless, an effective cross section for large-angle scattering by ion collisions can be derived analytically. The general Coulomb cross section is defined in terms of the impact parameter r_0 as

$$\sigma_{Coulomb} = \pi r_0^2 = \pi \left(\frac{e^2}{4\pi\epsilon_0 m_e v^2} \right)^2 = \frac{\pi e^4}{\left(4\pi\epsilon_0\right)^2 \left(kT_e\right)^2} \tag{4.19}$$

where we take v to be the thermal velocity such that $kT_e = m_e v^2$. This cross section only takes into account large-angle scattering collisions[4]; the Coulomb logarithm introduced by Spitzer additionally takes into account the much larger cumulative effect of many small-angle scattering collisions 4.19 to give the total electron-ion scattering cross section as

$$\sigma_{ei} = \frac{\pi e^4}{\left(4\pi\epsilon_0\right)^2 \left(kT_e\right)^2} ln\Lambda \tag{4.20}$$

where the Coulomb logarithm $ln\Lambda$ is the logarithm of the ratio of upper and lower bounds on the range over which the Coulomb force is appropriate. Physically, the upper bound is where space charge shielding comes into play, on the order of the Debye length, and the lower bound is where the momentum transfer to the incoming electron gives a perpendicular scattering momentum equal to the incoming momentum. The Coulomb logarithm has a weak dependence on plasma density and electron temperature, but over a vast range of plasma parameters it is about 10. Simple expressions for the Coulomb logarithm with a singly charged ion are:

$$ln\Lambda = \begin{cases} 23 - \frac{1}{2} ln\left(\frac{n_e}{T_e^3}\right) & T_e < 10\,eV \\ 24 - \frac{1}{2} ln\left(\frac{n_e}{T_e^2}\right) & T_e > 10\,eV \end{cases} \tag{4.21}$$

The electron-ion collision frequency is then

$$\nu_{ei} = n_i \sigma_{ei} v_e = n_i \frac{\pi e^4}{\left(4\pi\epsilon_0\right)^2} \frac{1}{m_e^{1/2} \left(kT_e\right)^{3/2}} ln\Lambda \tag{4.22}$$

As noted above, plasma densities and electron temperatures have been measured in the near-field in front of the channel by Reid using a swept Langmuir probe on a high-speed reciprocating motion stage. These values are shown in Figure 4.8. Since the plasma density spans a wide range but is measured by a single probe, with increasing axial distance the probe transitions from a thin-sheath regime where the probe radius is much greater than the Debye length to an orbital motion-limited

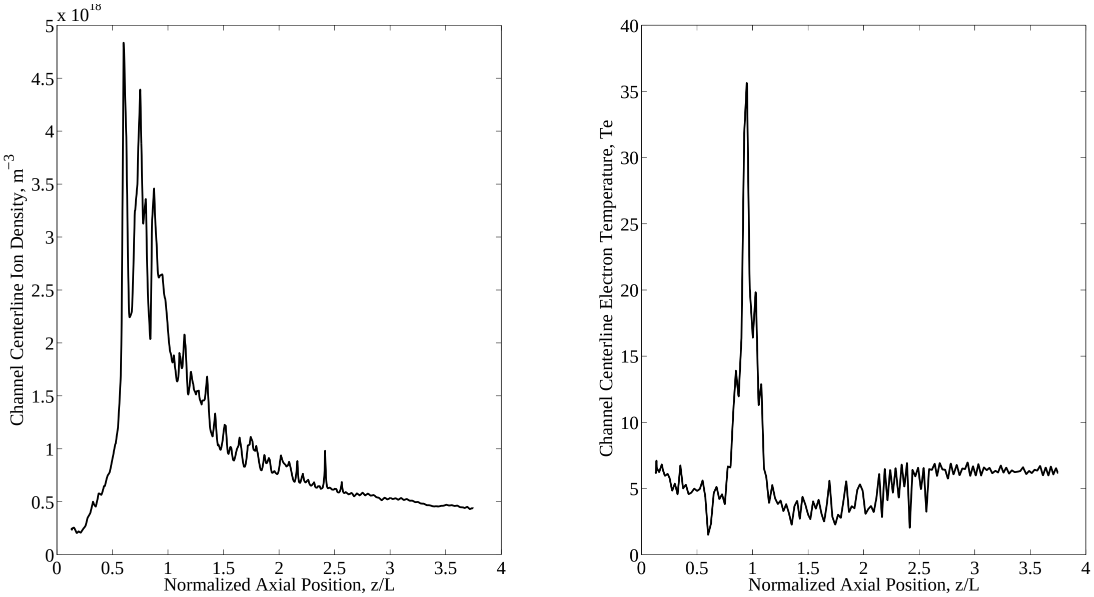

Figure 4.8. Measured ion density and electron temperature on the H6 channel centerline at 300 V, 20 mg/s as a function of the normalized axial coordinate z/L where L is the discharge channel length and $z = 1$ denotes the exit plane. The plasma density in the near-field, i.e., within one discharge channel length of the exit plane, is approximately 10^{18} m^{-3} and the near-field electron temperature is about 3-5 eV.

(OML) regime where the probe radius is of the same order as the Debye length. Reid accounted for this with a weighted average of the densities computed by each method depending on where the probe radius to Debye length ratio r_p/λ_D falls in the range $3 < r_p/\lambda_D < 10$.

The collision frequency computed from Eqn. 4.22 using these values for density and temperature cannot be compared directly to collision frequencies derived from the cross sections of Figure 4.7 because those cross sections are for individual incident particles with a given energy, while Eqn. 4.22 is for a population of electrons with a given mean temperature. To cast the cross-sections from Figure 4.7 into comparable form they must be integrated over a Maxwellian distribution to compute a Maxwellian collision frequency as

$$\nu = n\left\langle \sigma v \right\rangle = n\int \sigma\left(v\right) v f\left(v\right) dv = n\int \sigma\left(E\right)\sqrt{\frac{2E}{m}} f\left(E\right) dE$$

where the Maxwellian distribution $f\left(E\right)$is given by Eqn. 4.17. This integration has already been performed for the cross section data of Nickel[9] (one of the contributors to the compiled cross section data from Dias in Figure 4.7) for use in HPHall-2 by Hofer[26] and fit to functional form:

$$\sigma_{en} = \begin{cases} 33.9581 \times 10^{-20} & T_e < 5\,eV \\ 10^{-20}\left(11.3596 + 28.0985\exp\left(-0.0433494 * T_e\right)\right) & T_e \geq 5\,eV \end{cases}$$

This form has already been used by Reid as part of internal analysis of the H6 Hall thruster to compute the electron-neutral collision frequency in the near-field plume in front of the discharge channel.[23] These frequencies used neutral densities calculated from continuity arguments with ion flux calculations and electron temperatures measured by swept Langmuir probe. The electron-ion, electron-neutral and electron-wall frequencies are compared in Figure 4.9. In the near field $z/L_c < 2$ the electron-ion collision frequency never reaches above about 4-5 times the electron-neutral collision frequency, and extending out to 3.5 channel lengths the electron-ion collision frequency is about 30 times the electron-neutral collision frequency.

4.2.5 Monte Carlo Collision Implementation

Equation 4.18 is valid only for small time intervals Δt where n and v can be assumed constant. Generally this is sufficiently short that $\nu\Delta t \ll 1$, so in any given timestep a collision is unexpected, but over several such steps the likelihood of a collision event "builds up" until eventually one is due to take place. This scenario is well-suited to Monte Carlo methods, where by treating a sufficiently large number of statistically independent trials the probable final outcome(s) of a series of random events can be estimated. In MCHall likely electron transport pathways are estimated

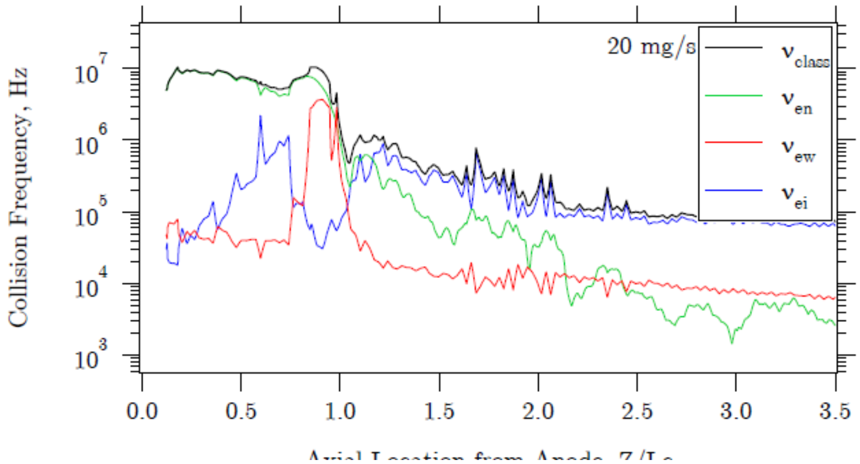

Figure 4.9. Figure courtesy of Reid.[23] Experimental collision frequencies on H6 channel centerline at 300 V, 10 mg/s. The electron-ion collision frequency is largest, but in the very near field $z/L_c < 2$ it never exceeds 4-5 times the neutral collision frequency, and even several channel lengths downstream ν_{ei}/ν_{en} only reaches about 30.

by simulating a large number of electron trajectories through random scattering processes with an appropriate distribution of initial conditions.

Detailed implementation of a Monte Carlo scattering process is outlined in the review paper by Birdsall.[24] The probability of a particle collision in a time step Δt is

$$P_{collision} = 1 - exp(-\nu \Delta t) \tag{4.23}$$

For the timesteps and conditions in MCHall the argument of the exponent is very small and Eqn. (4.23) may be approximated by Taylor expansion of the exponent as

$$P_{collision} \approx \nu \Delta t \tag{4.24}$$

The "building up" of probability over time occurs by repeatedly comparing the collision probability with a unique random number R_1 generated on each timestep. If $P > R_1$, a collision occurs. In practice, several collision pathways are considered simultaneously, and the cross section used to calculate ν in Eqn. (4.18) is a total cross section computed as the sum of the cross sections for each event. If a collision occurs on a given timestep, a second random number R_2 is generated, the relative cross sections are lined up on the range from 0 to 1 as σ_1/σ_{tot}, $(\sigma_1 + \sigma_2)/\sigma_{tot}$, $(\sigma_1 + \sigma_2 + \sigma_3)/\sigma_{tot}$, etc., and the reaction is given by the scattering process covering the range where R_2 falls. To ensure statistical independence, each electron is assigned a unique seed in the random number generator.

After a collision MCHall chooses a new unit vector direction distributed randomly over the unit sphere and, after adjusting the electron energy to account for any losses in the scattering process (for example, -12.13 eV for ionization), the electron is sent along its way in the new direction. Some further refinement of the exit velocity distribution as a function of the incoming velocity vector is possible and outlined by Birdsall, but for simplicity the method used here is just probabilistic hard-sphere scattering.

4.2.5.1 Simulation parallelization, speed and convergence

Whether a number of trials is "sufficiently large" is a matter of convergence of the model's final state; for MCHall, I treat the model as converged when doubling the number of particles does not appreciably affect the results. In practice, this is implemented when the average lifetime of the ensemble of electrons does not change by more than 10%, the fraction of primary electrons producing a secondary electron does not change by more than 1%, and the distribution of final exit points of electrons in the simulation (i.e., lost to far field, impact with cathode keeper, etc.) does not change by more than 1%. This generally occurs at between 10^3 and 10^4 electrons. Beyond this point histogram plots become smoother, but no real new insights are obtained.

The code is run in parallel on an AMD Opteron 6128 8-core 2.0 GHz processor in MATLAB r2011a. A simulation of 10^4 electrons from the cathode requires about 2 hours, for an average simulation rate of about 6 seconds / electron / core. The low simulation speed is due to the very small timesteps, $\omega_c \Delta t = 10^{-3}$, used to ensure conservation of energy during confined electron orbits which may have durations up to 10^{-5} seconds, corresponding to up to several million timesteps. Simulations seeded from the thruster channel are significantly more time-consuming; the predominantly confined orbits in this region compared to the many electrons that depart straight to the far-field in the cathode-seeded cases raise the simulation time by a factor of about 100, such that simulations of only 100 electrons are typically run with channel seeding.

Field interpolation is the largest part of simulation time, taking 50-70% of a given simulation's wall time, while the compact Boris algorithm takes only about 20%. An arbitrary cutoff was imposed at 10^{-5} seconds for this simulation, since this corresponds to a tenth of the period of a 10 kHz oscillation, on the order of the breathing mode, and conclusions drawn from static field simulations at timescales longer than this seem questionable.

Parallelization of the code is accomplished through the angular and energy distributions pictured in Figure 4.6. Different discrete energy levels are simulated in parallel on separate cores, and within each energy level on a core a complete angular distribution of electrons is seeded in series. To get good approximation to both the angular and energy distributions, for a desired run of N electrons I use $\sqrt{N}$ energy bins and $\sqrt{N}$ angular bins.

4.3 Simulation Results

4.3.1 Baseline simulation

The baseline MCHall simulation is of 10^4 electrons seeded into the H6 plume from a point source cathode on thruster centerline at the exit plane. There are few surprises in the baseline; given that classical transport is not expected to move electrons across field lines well if at all, the baseline behaves as expected in delivering almost all electrons to an axisymmetric focused dispersal into the far-field simulation boundary at $z = 21$ cm within a fraction of a microsecond. The mean electron lifetime is 1.0×10^{-7} seconds. A small fraction of electrons, about 10% of the total, are reflected back into the cathode orifice or into a collision with the cathode keeper surface due to a weak magnetic mirror in front of the cathode orifice. Two electron trajectories are shown in Figure 4.10, one a typical case of an electron emitted from the cathode and departing without interruption to the far field plume, the other a very atypical case of a long-lived secondary electron confined for an extended azimuthal drift. The typical primary electron has a lifetime of only a fraction of a microsecond in the simulation domain, experiences no collisions, and exits as part of a tight beam downstream on thruster centerline.

The initial electron velocities are such that the electrons tightly follow the magnetic field on thruster centerline into the far field, exiting the simulation domain an average of 9.7 mm off centerline at 2.6 mean thruster channel radii downstream, with 50% of all electrons exiting within a median 4.8 mm off centerline. While Smith found little contribution to cross-field transport due to binary plume collisions with neutrals, neutral collisional scattering is the only reason that any electrons are knocked off this beam to the far field to form the long-lived tail of the distribution of lifetimes in Figure 4.12. Some 80% of all electrons are expected to depart into the far field to neutralize the beam current, which means 2000 electrons in a simulation that correctly reproduced anomalous transport should have made it to the channel. Instead, not one of over ten thousand electrons not did so, or even reached one of the thruster poles. This is in rather severe contrast to Smith's results showing substantial transport due to thruster surface collisions in time-averaged fields discussed in Section 4.1.1.

The majority of electron lifetimes in the plume are distributed by the travel time from the cathode to exit plane given by the Maxwellian velocity distribution and accounting for the strong axial electric fields near thruster centerline. One interesting result of this work is the inclusion of secondary electrons, which when broken out account disproportionately for the long tail of the lifetime distribution. Part of this is because of the zero energy these secondaries are seeded with, but part is because with zero initial velocity they are free to become trapped on the magnetic field lines where they are born in a drift pattern and enter into extended, confined orbits. Of the handful of electrons in the baseline simulation with lifetimes longer than a microsecond, all are secondary electrons. The spike in population at 10^{-8} seconds is an aggregate of all electrons having very short lifetimes $\tau < 10^{-8}$.

In terms of proportional representation in the lifetime distribution, note that in a real discharge electrons are continuously seeded from the cathode, so long-lived electron populations observed in isolated seeding like that shown here would be more strongly represented at steady state from continual seeding in a normalized distribution. This scaling would be by a factor equal to their lifetime divided by the lifetime of the mean of the distribution. For the case here of electrons with lifetimes near to 10^{-5} seconds in a distribution with mean on the order of 10^{-7} seconds, these small populations would be a hundred times more prevalent at steady state.

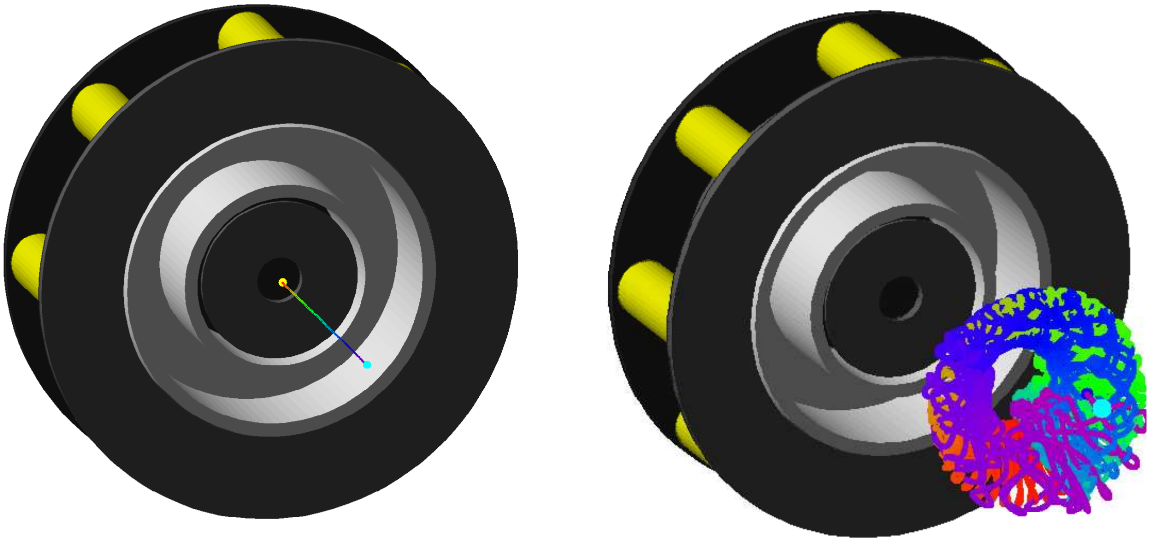

Figure 4.10. Two electron orbits observed out of over 10^4 in a simulation run of MCHall. Left, a typical orbit with a lifetime on the order of 10^{-7} seconds stays confined to thruster centerline after being emitted from a centrally mounted cathode (not pictured). The orbit is color-coded in time from red to violet, the yellow dot marks the sourcing point, and the blue dot marks the exit from the simulation domain. At right, an atypical secondary electron generated by an ionizing collision in the near-field is held in a confined azimuthal drift on the order of 10^{-5} seconds. This orbit is the longest-lived electron in the simulation run.

Conversely, the short-lived tail of electrons with lifetimes below 10^{-8} seconds are less prevalent in a steady state distribution and not as worthy of notice. Of course, this also speculates that it is reasonable to consider a “steady state” simulation of Hall thruster operation since the real thruster is characterized by fluctuating fields that are not accounted for here. Extending electron trajectory modeling to real time-resolved fields is a high priority and discussed in the next chapter as recommended future work.

4.3.2 Simulations from discharge channel centerline

A difficulty in modeling anomalous mobility in the center-mount cathode configuration is that electrons are seeded axially while trapped on the strongest magnetic field anywhere in the thruster plume – if the model fails to capture the anomalous character of the transport, all of the electrons will behave exactly as observed in the

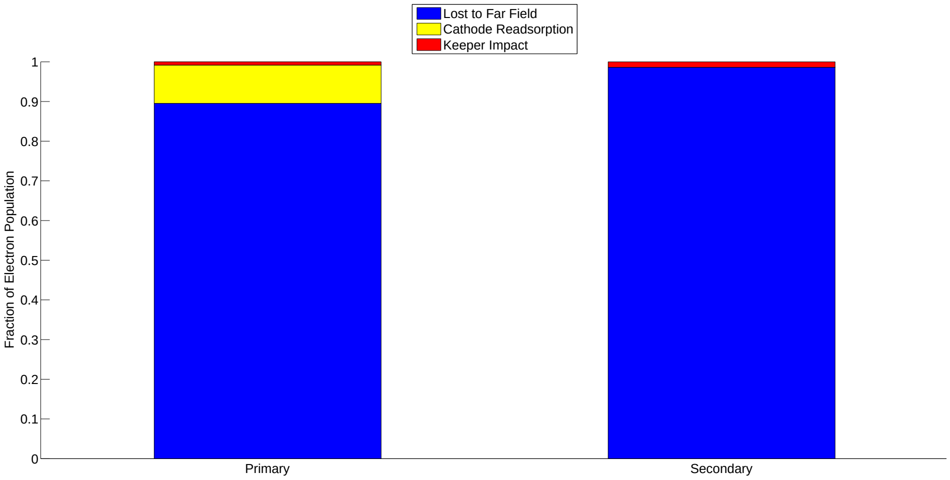

Figure 4.11. Exit locations from the MCHall simulation domain in the baseline simulation for primary electrons, left, and secondary electrons, right. The vast majority of both populations exit the domain into the far field, while a small fraction are reabsorbed into the cathode orifice (primaries only) or impact the keeper. No electrons make it to the discharge channel or impact the thruster poles.

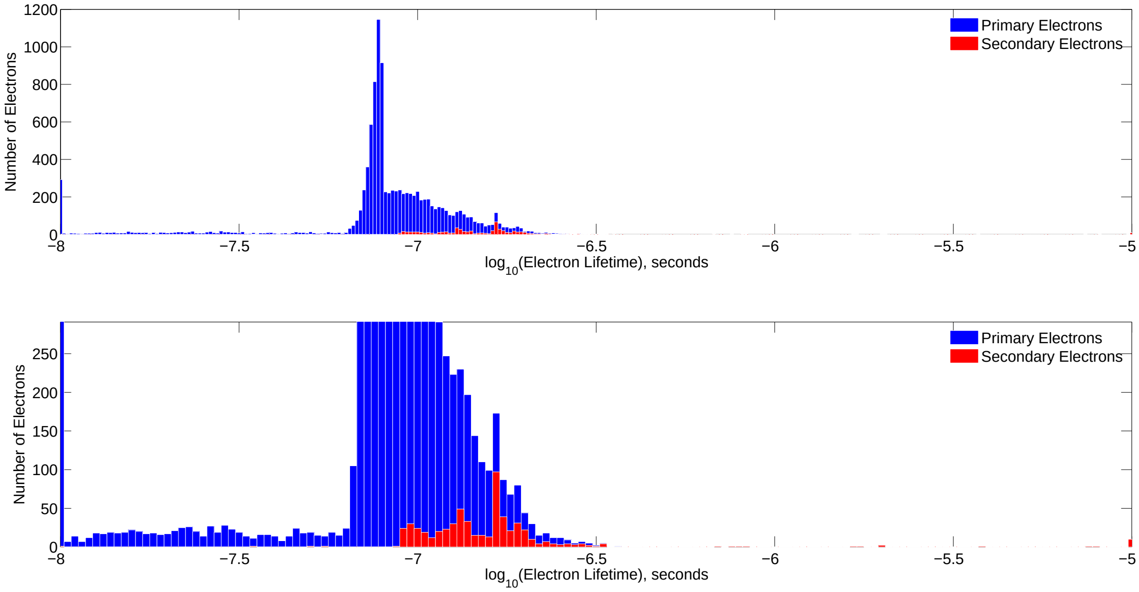

Figure 4.12. Distribution of electron lifetimes seeded at T_e =2 eV from the centrally mounted H6 cathode. Above, the entire distribution is shown, while below the scale is exaggerated to show the contributions of secondary electrons from ionization events. The mean lifetime over all electrons is 1.0×10^{-7} seconds. The secondary electrons, shown in red, have a longer average lifetime (3.7×10^{-7} seconds) than primaries since they are born at zero velocity and tend to be born off thruster centerline, where they are more likely to be caught in an azimuthal E $\times$ B drift before exiting the simulation. The very long-lived tail of the distribution is entirely composed of secondary electrons.

previous section, classically following confined helical orbits on the magnetic field and exiting almost immediately. This region, with the geometry of a high current density or arc passing axially along a magnetic field, is particularly subject to turbulent instability due to fluting, Rayleigh-Taylor and Kelvin-Helmholtz instabilities due to the strong radial gradients in plasma density and $E \times B$ velocity. Such modes are not considered in the static field configuration of MCHall.

This difficulty and also the poor spatial resolution of fields in the cathode region noted in Section 4.2.3 motivated a second seeding point, directly on channel centerline and only a single discharge channel length downstream of the exit plane. The qualitatively different character of a few confined orbits from secondary electrons seen in the baseline simulation made this case interesting as it should see substantially more of those confined orbits. These electrons are also seeded from a Maxwellian distribution at 2 eV , but due to the confined nature of the orbits and the correspondingly longer simulation times, only 100 electrons are seeded in this case. While the baseline simulation's cathode-born electrons are seeded from a half-Maxwellian, the electrons seeded over the channel are seeded from a full Maxwellian and as a result the initial velocity unit vector directions are distributed randomly over a full 4π of solid angle. The actual electron temperature at this axial location is more like 3-5 eV, based on the results from Reid shown in Figure 4.8, but the limited radial extent of the current maps for plasma potential preclude the simulation of these higher energy electrons because they penetrate too far radially over the outer pole and are lost to the simulation. The depth of the plasma potential well over the outer pole, which drops to very near the ground potential of the pole itself, makes it unlikely even the slightly higher temperature electrons observed over the channel in this region could penetrate to the outer pole. Still, the continued development of MCHall as more complete experimental maps become available has a high priority in future work, in part so that the realistic temperatures in this region can be explored more fully.

One feature that is not included in MCHall is the effect of electron-ion collisions, which can be even more frequent than electron-neutral collisions in the near-field. Lacking maps of ion density of the type used for the neutral density calculations over the whole plume, the enhanced collisional effect of this additional collisional pathway is introduced by simulating elevated neutral densities when seeding electrons over the channel. This is introduced as a sensitivity parameter and the results were observed at 1x, 10x and 100x neutral density in the plume. Figure 4.13 shows typical orbits for each of the 1x and 100x sensitivity studies.

At the normal density simulation all 100 electrons either time out or exit to the far-field plume; none make it to the discharge channel or pole pieces. The electrons that exit to the far-field plume are those few in Figure 4.14 with a lifetime less than the maximum 10^{-5} seconds. These are not simulation domain exits of the type seen in the baseline simulation, straight down thruster centerline, but rather are a consequence of the radial limit of the input field meshes in Figure 4.5 about halfway through the outer pole. Some collisions kick the orbiting electrons into a direction where they penetrate deeply through the electrostatic barrier over the outer pole, as can be seen to a limited extent in the orbit at left in Figure 4.13. Other than these exits, the rest of the electrons are confined in stable azimuthally drifting orbits with minimal scattering across field lines. In the normal density simulations the electrons experience an average of 8 scattering collisions over the 10 microseconds of simulation time, with only a small handful of ionization or excitation collisions due to the energy threshold for these processes – lacking cross-field transport the electrons cannot gain energy easily in this region and so tend to stay too cold to take part in inelastic collisions.

The results with 100x neutral density are essentially the same as with normal density level – no electrons make it to the discharge channel or outer poles, a few exit radially from the simulation domain and most time out. Qualitatively these electrons have less azimuthal drift than the electrons seeded at normal density, due to their much higher number of collisions. They also tend to scatter more back and forth across the field lines (see Figure 4.15), but this does not produce a great deal of net axial transport. For one thing, if the electrons were still confined on magnetic field lines after 10 microseconds or a tenth of a breathing mode cycle in the real plasma, collisional transport would quickly become immaterial as the entire thruster plasma properties changed drastically with the mass expulsion of ions and as-yet uncharacterized upheaval of the near-field plasma potential. While this method might eventually produce more realistic bulk transport if the collisional frequencies were continually increased, this is already what hybrid codes do and repeating it in MCHall would not provide new information. A neutral collision frequency increase by a factor of 100 is a reasonable level to confirm that even if the effects of ions were included, some other phenomenon must be driving the transport in this region.

4.4 Qualitative Experiments on Thruster Surface Conditions

The electron model has great difficulty reproducing electron transport to the pole pieces or discharge channel. In a real thruster the electrons have no difficulty reaching the channel, however, and it stands to reason they may also reach the poles, even in large quantities, in spite of the model's inability to capture this effect. Since the electron interaction with the poles is important only if it contributes to the net electron transport to the channel, this section presents a simple experiment to

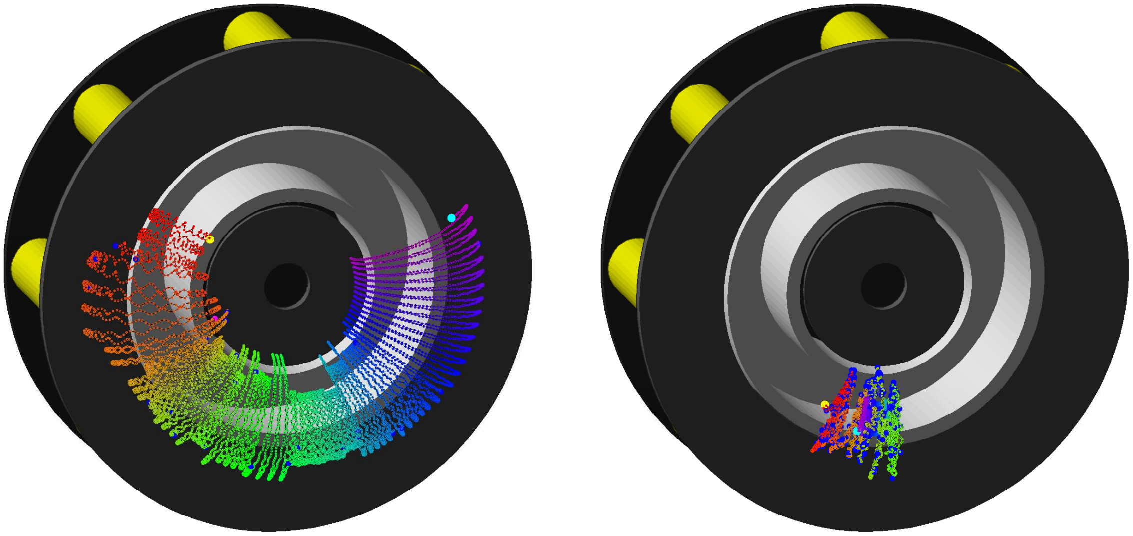

Figure 4.13. Simulated electron orbits for seeding directly in front of the channel with normal neutral density, left, and 100x elevated neutral density, right. In the elevated neutral density case the azimuthal drift is seriously impeded, but with some additional random-walk transport back and forth over magnetic field lines compared to the 1x case. However, the level of transport is still very small. Both orbits are truncated at an imposed ceiling of 10^{-5} seconds, corresponding to one tenth of a 10 kHz breathing mode cycle.

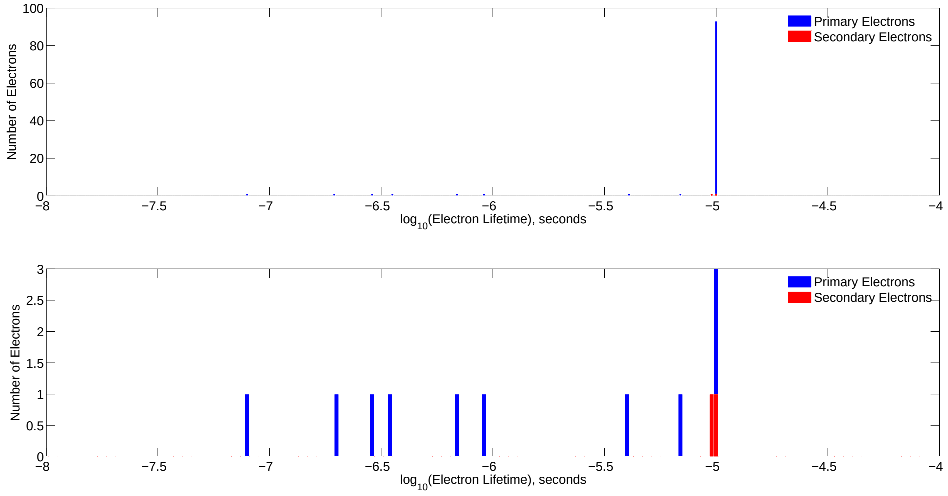

Figure 4.14. Distribution of electron lifetimes seeded at T_e =2 eV over discharge channel centerline with normal neutral density, one discharge channel length downstream of the exit plane. The mean lifetime over all electrons is effectively the imposed limit on simulation duration at 1.0×10^{-5} seconds. The few electrons that exit the domain before that limit exit through the radial border over the outer pole, shown in Figure 4.5.

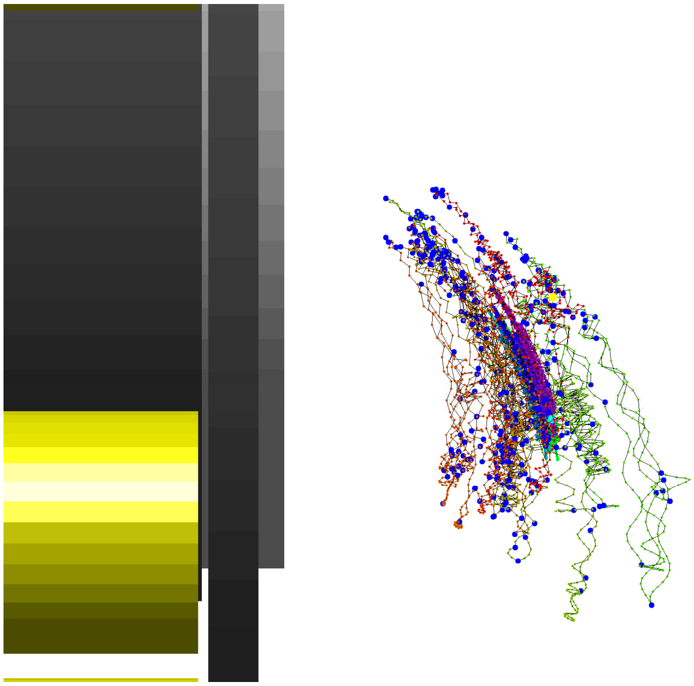

Figure 4.15. Side view of an electron orbit seeded in front of the discharge channel with 100x normal background neutral density. Electron-neutral collisions are indicated by large blue dots. The orbit travels somewhat back and forth across the magnetic field lines (elapsed time in the orbit goes from red to violet in rainbow order), but overall it does not experience much axial transport from orbit beginning (the large yellow dot near the top) to end (the large light blue dot in the middle).

determine whether the pole boundary condition affects thruster operation.

Recall that the thruster pole pieces are used to shape the magnetic field by bridging the inner and outer solenoid cores to form a magnetic circuit. As a result the pole pieces are always some form of iron, a conductive metal. In some thrusters, such as the H6, these iron pole pieces are bare and exposed to the plasma. In others, such as the Aerojet BPT-4000, Busek BHT-200, or NASA 300M, the pole pieces are spray-coated in insulating ceramic such as aluminum oxide or boron nitride. The result is either a radial short circuit at constant potential or a floating boundary at variable potential in the near field. Since the thruster body is mechanically fastened to metal mounting structures in a metal vacuum chamber, this short circuit is at ground potential.

If interaction with the thruster surface in the near-field are truly an important mechanism for thruster operation, there should be substantial differences in thruster behavior when the conditions of the pole surfaces are changed. To check this, an insulating pole material was mimicked on the H6 by floating the thruster body as a whole. The pole is still shorted in this case since the iron is still conducting, but as it turns out the floating potential is significantly lower than ground.

Since the thruster is normally grounded through the base mounting plate, to float it a mica sheet was placed under the base mounting plate and fiberglass insulating screws were used to fasten the mounting plate down to the chamber structure (Figure 4.16). A large gauge wire was secured to the thruster body and routed outside the chamber, where it could be manually shorted to ground, floated, or even biased at will. For this test it was either floated or grounded; in the floating condition the voltage to ground was measured, and in the grounded condition the current to ground was measured.

The variation in potential of the thruster body between the two conditions was striking. The thruster body floating potential was -33.2 V, indicating that when ungrounded the thruster drove far into the negative potentials to drive off electron current from the plasma. While grounded, the multimeter measured 2.1 A of electron current drawn into the thruster body. The large current, on the order of 10% of the discharge current, reflects the enormous exposed area of the thruster in the plasma. In spite of this large disturbance to the plasma conditions, the discharge current changed by only 250 mA from 20.14 A in the usual grounded configuration to 19.89 A in the floating configuration, while the cathode floating potential dropped slightly from -9.9 V to -12.1 V in the grounded and floating cases, respectively.

One might have expected that floating the thruster, and thus preserving electrons in the discharge that would otherwise have been lost to ground, would increase the discharge current as more electrons were able to backstream to the channel. Instead it had the opposite effect, decreasing the discharge current by a small amount. This experiment confirms that, in spite of the inability of MCHall to model their actual motion, electrons are able to reach the thruster body in large numbers and that during normal operation an additional population of electrons equal to about 10% of the normal discharge current do discharge through the thruster body to ground. However, the minimal impact this has on the total discharge current makes it unlikely that this mechanism is playing a dominant role in the overall electron transport picture in the near-field.

4.5 Summary

The development of MCHall was intended to test a hypothesis that collisional transport with thruster surfaces in the near field is a significant factor in opera-

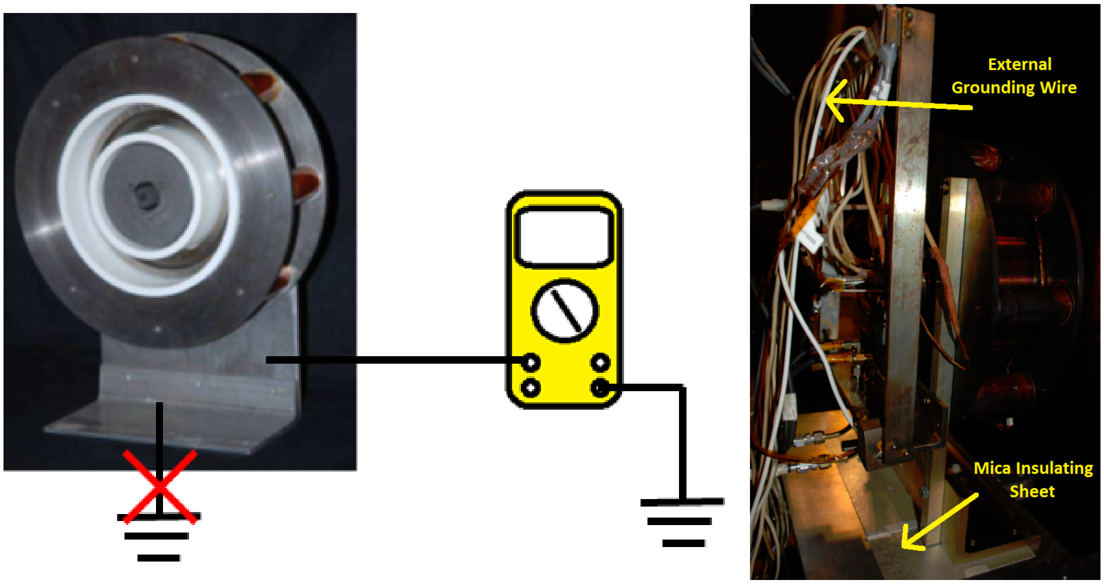

Figure 4.16. Simple electrical schematic (left) and photo (right) of experimental setup to electrically float the H6. A mica sheet breaks the usual contact between the thruster mounting plate and the chamber, and a wire run out of the chamber to a multimeter allows the thruster pole condition to be varied without breaking vacuum. Fiberglass insulating screws secure the thruster to the structure underneath the mica sheet. As pictured in the schematic the multimeter is measuring the current drawn by the thruster poles when they are grounded; when floated the connection to ground is severed entirely.

tion of the H6, a large high-power Hall thruster with a centrally mounted cathode. Such transport had previously been simulated by Smith in work on the Stanford Hall thruster, a physically smaller and lower power thruster with an externally mounted cathode. MCHall differed from Smith's simulation technique by including experimental measurements for the plasma potential and focusing on inclusion of electron-neutral collisions in the plume using experimental maps of the neutral density. Electron-ion collisions were also included through the use of an inflated neutral density, based on previous experimental assessments of collision frequencies in front of the discharge channel by Reid. The sheath effect over the thruster surfaces was informed by measurements of plasma potential with low-profile planar Langmuir probes on the thruster poles, though this turned out not to be necessary since electrons in the simulation could not penetrate the significant plasma potential barriers to reach the area a few millimeters in front of the poles where the probes' data was included.

Ultimately Smith's results could not be reproduced on the H6 using MCHall. There are a number of possible reasons for this, both experimental and numerical. Experimentally, Smith's thruster is quite different from the H6. It is smaller and operates at about one tenth the discharge power of the H6, it uses an external cathode and it has floating, not grounded, poles. Tellingly, grounding versus floating the poles of the H6 barely makes a difference in that thruster's operation, while conversations with Smith have revealed that these details are important and produce gross changes to the operation of the Stanford Hall Thruster.

Numerically, the spatial domain of Smith's simulations is much larger relative to the size of his thruster than the domain of MCHall. Smith's domain extended six times the thruster outer channel diameter both axially and radially; by contrast the H6 plasma property maps that dictated MCHall's domain only extend about 1.25-1.5 outer channel diameters in each direction. It is possible that electrons that were deemed "lost" for MCHall would have returned to the simulation and eventually made it to the channel with a much larger domain size. On the other hand, the implementation of the sheath and fields especially over the poles in Smith's domain may not be as close to experiment as the ones in MCHall, such that estimates of electron penetration into the thruster sheath in that simulation may be subject to systematic error. One point of confusion is the "kick" that Smith gives electrons leaving the cathode, equal to the local plasma potential. This is not done in MCHall, because the energy associated with the plasma potential is considered as a potential energy, only realized into kinetic energy as the electron travels into regions with lower potential. This may give the electrons an enhanced ability to penetrate into the sheaths over thruster surfaces.

Whether or not the results of MCHall agree with the work of Smith, the more important question is how they compare to experimental results with the H6. In 4.4 it was noted that in the normal, grounded configuration of the H6 approximately 10% of the electrons neutralize the beam current by grounding through the thruster pole pieces. This phenomenon is totally unobserved in MCHall, and indicates that the model is not reproducing the flux of electrons into this region accurately. Considering the energy barriers in the static plasma potential profiles over the poles, it is not clear how electrons of the temperatures measured in teh plume could be penetrating to the poles in such large numbers. It suggests that, for all the effort toward simulating collisional transport mechanisms in MCHall, some other force is at work in the near field. The main alternative is turbulent transport, to be considered in the next chapter.

[1] Reid, B. M. and Gallimore, A. D., "Langmuir Probe Measurements in the Discharge Channel of a 6-kW Hall Thruster," *44th AIAA/ASME/SAE/ASEE Joint Propulsion Conference & Exhibit*, AIAA 2008-4920, 2008.

[2] Jahn, R. G., *Physics of electric propulsion*, Dover Publications, Inc., May 2006.

[3] Koo, J. W. and Boyd, I. D., "Modeling of anomalous electron mobility in Hall thrusters," *Physics of Plasmas*, Vol. 13, No. 3, March 2006, pp. 033501–7.

[4] Chen, F. F., *Introduction to Plasma Physics and Controlled Fusion: Plasma physics*, Plenum Press, New York, Feb. 1984.

[5] Smith, A. W. and Cappelli, M. A., "Numerical investigation of electron behavior in the near-field of Hall thrusters," 43rd AIAA/ASME/SAE/ASEE Joint Propulsion Conference & Exhibit, Cincinnati, OH, AIAA 2007-5240, 2007.

[6] Fife, J. M., *Hybrid-PIC Modeling and Electrostatic Probe Survey of Hall Thrusters*, Ph.D. thesis, Massachusetts Institute of Technology, Cambridge, MA, 1998.

[7] Garrigues, L., Hagelaar, G. J. M., Boniface, C., and Boeuf, J. P., "Anomalous conductivity and secondary electron emission in Hall effect thrusters," *Journal of Applied Physics*, Vol. 100, No. 12, Dec. 2006, pp. 123301–9.

[8] Buneman, O., "Time-reversible difference procedures," *Journal of Computational Physics*, Vol. 1, No. 4, June 1967, pp. 517–535.

[9] Nickel, J. C., Imre, K., Register, D. F., and Trajmar, S., "Total electron scattering cross sections. I. He, Ne, Ar, Xe," *Journal of Physics B: Atomic and Molecular Physics*, Vol. 18, No. 1, Jan. 1985, pp. 125–133.

[10] Goebel, D. M. and Katz, I., *Fundamentals of Electric Propulsion*, John Wiley and Sons, 2008.

[11] Mikellides, I. G., Katz, I., and Hofer, R. R., "Design of a Laboratory Hall Thruster with Magnetically Shielded Channel Walls, Phase I: Numerical Simulations," *47th AIAA/ASME/SAE/ASEE Joint Propulsion Conference & Exhibit*, AIAA 2011-5809, 2011.

[12] King, L. B., "A (Re-) Examination of Electron Motion in Hall Thruster Fields," *29th International Electric Propulsion Conference*, 2005, pp. 2005–258.

[13] Mikellides, I. G., Katz, I., Hofer, R. R., and Goebel, D. M., "Hall-Effect Thruster Simulations with 2-D Electron Transport and Hydrodynamics Ions," *31st International Electric Propulsion Conference*, IEPC-2009-114, Ann Arbor, MI, 2009.

[14] Hofer, R., Mikellides, I., Katz, I., and Goebel, D., "Wall Sheath and Electron Mobility Modeling in Hybrid-PIC Hall Thruster Simulations," July 2007.

[15] Dias, T. H. V. T., Santos, F. P., Stauffer, A. D., and Conde, C. A. N., "Monte Carlo simulation of x-ray absorption and electron drift in gaseous xenon," *Physical Review A*, Vol. 48, No. 4, Oct. 1993, pp. 2887, Copyright (C) 2010 The American Physical Society; Please report any problems to prola@aps.org.

[16] Haas, J. and Gallimore, A., "Considerations on the role of the Hall current in a laboratory-model thruster," *Plasma Science, IEEE Transactions on*, Vol. 30, No. 2, 2002, pp. 687–697.

[17] Lieberman, M. A. and Lichtenberg, A. J., *Principles of plasma discharges and materials processing*, John Wiley and Sons, April 2005.

[18] Smith, A. W. and Cappelli, M. A., "Single particle simulations of electron transport in the near-field of Hall thrusters," *Journal of Physics D: Applied Physics*, Vol. 43, No. 4, 2010, pp. 045203.

[19] Jameson, K., *Investigation of Hollow Cathode Effects on Total Thruster Efficiency in a 6-kW Hall Thruster*, Ph.D. thesis, University of California Los Angeles, Los Angeles, CA, 2008.

[20] Birdsall, C. K. and Langdon, A. B., *Plasma physics via computer simulation*, IOP Publishing Ltd., Bristol, England, 2004.

[21] Hofer, R. R., Katz, I., Mikellides, I. G., Goebel, D. M., Jameson, K. K., Sullivan, R. M., and Johnson, L. K., "Efficacy of Electron Mobility Models in Hybrid-PIC Hall Thruster Simula-

tions," 44th AIAA/ASME/SAE/ASEE Joint Propulsion Conference, Hartford, CT, AIAA-2008-4924, 2008.

[22] Kushner, M., "Computational Plasma Science and Engineering Group HPEM Database," 2010.

[23] Reid, B., *The Influence of Neutral Flow Rate in the Operation of Hall Thrusters*, Ph.D. thesis, University of Michigan, Ann Arbor, MI, 2009.

[24] Birdsall, C. K., "Particle-in-cell charged-particle simulations, plus Monte Carlo collisions with neutral atoms, PIC-MCC," *IEEE Transactions on Plasma Science*, Vol. 19, No. 2, 1991, pp. 65–85.

[25] Smith, A. W. and Cappelli, M. A., "Investigation of field structure and electron behavior in near-field of Hall thrusters," 42nd AIAA/ASME/SAE/ASEE Joint Propulsion Conference and Exhibit, Sacramento, CA, AIAA 2006-4835, 2006.

[26] Hofer, R. R., Mikellides, I. G., Katz, I., and Goebel, D. M., "BPT-4000 Hall Thruster Discharge Chamber Erosion Model Comparison with Qualification Life Test Data," Florence, Italy, Sept. 2007, pp. IEPC 2007–278.

[27] Hargus, W. A., *Investigation of the Plasma Acceleration Mechanism within a Coaxial Hall Thruster*, Ph.D. thesis, Stanford University, Palo Alto, CA, 2001.

[28] Smith, A. W., "Private Communication," March 2010, Private communication.

CHAPTER V

Turbulent transport by Rotating Spoke Instabilities

"Who ordered that?"

Isidor Rabi, on the discovery of the muon, 1937

The second category of electron transport in Hall thrusters is turbulent transport, the collisionless transport of electrons by formation of drift currents across the applied magnetic field due to induced oscillations in the electric and/or magnetic field. In principle these fluctuations may take place at any frequency, and the Hall thruster is rich in candidate oscillations from ionization and transit-time related instabilities in the low kilohertz all the way up to electron cyclotron frequencies in the gigahertz range. Practically speaking a systematic study of these oscillations is best carried out ascending from low frequencies to higher, since experimental detection and verification becomes increasingly difficult with faster oscillations.

This chapter focuses on the detection, characterization and measurement of the cross-field current due to a particular low-frequency phenomenon, the rotating spoke instability. A Fourier analysis technique to describe the presence and strength of spoke modes detected in high-speed video of the Hall thruster discharge channel has been developed and applied to videos of several Hall thrusters, including the H6. Every Hall thruster imaged to date across an order of magnitude in discharge power has revealed the presence of spokes to some degree, indicating an omnipresent phenomenon in Hall thrusters. A parameter study of visible spoke amplitude and velocity at several operating conditions in the H6 shows a complex dependence on the discharge voltage and magnetic field strength.

The current hypothesis is that these visible spokes correspond to some form of ionization wave, based on the low velocity of the observed spokes of the order of the critical ionization velocity in xenon and the visible nature of the wave, corresponding to photons emitted from excited ions and neutrals. The elevated regions of visible light emission may then correspond to regions of slightly elevated electron density and/or temperature, and if there are also plasma potential fluctuations associated with the spokes it could create a "rotating highway" carrying electrons across the near-field and down the channel to the anode. Such waves would be invisible to discharge current measurements on the ring-shaped anode, so a specially designed azimuthally segmented anode (Section 3.2.1) was constructed to resolve rotation in the electron current deposition to the anode. The segmented anode demonstrates a conclusive link between electron current oscillation frequencies and the visible spoke frequencies. Based on the magnitude of the segment current oscillations, on the order of 40% of the discharge current at the anode passes through the spoke structure. Unexpectedly, the rotating spoke oscillations are far larger than breathing mode oscillations on the local level in the thruster discharge channel, indicating that the apparent dominance of the breathing mode on traditional discharge current measurements is merely an artifact of the use of a ring-shaped anode. Suggestive evidence that the rotating spoke structure extends into this near-field region is also presented, though detailed probing of plasma parameters in this region with in situ probes to determine if this mechanism can explain the Hall parameter gap is left to future work.

5.1 Observations of rotating spoke instabilities

The diagnosis of the oscillatory behavior of a Hall thruster is typically made through Fourier analysis of the discharge current signal. A pressing difficulty in the detection of azimuthal instabilities of the type suspected to contribute to turbulent transport is that they are by definition undetectable in traditional discharge current measurements, since rotating points of electron current deposition would be integrated away around the 2π azimuthal extent of the conventional ring-shaped anode.

The detection of these instabilities instead requires simultaneous information about multiple points around the thruster azimuth. This can come either from an array of in situ plasma probes, or else in recent years from high-speed cameras like those described in Section 3.3. This section demonstrates visual evidence of rotating spokes in postprocessed still frames of high-speed video from several Hall thrusters, then reviews recently developed and published quantitative video analysis techniques to quantitatively assess spoke frequency and amplitude.[2,6,11]

While the Hall thruster discharge appears steady to the naked eye and in still images as in Figure 3.2, high-speed video reveals vigorous oscillations in the plasma. Overall flickering corresponding to the Hall thruster breathing mode is readily apparent and more subtle azimuthally rotating structures in the low kilohertz are present as well, strongly evocative of the phenomenon first reported by Janes and Lowder.[5]

The discovery of clear azimuthal structure in the Hall thruster discharge channel is significant because it fits with a common picture of turbulent transport due to an azimuthal electric field component in the plasma that can drive axial drift currents. Just as the applied radial magnetic field and axial electric field cause an azimuthal

Hall current, if an azimuthal wave structure were formed due to some plasma instability then any associated azimuthal electric field components would combine with the applied radial magnetic field to induce an axial component of the $\mathbf{E} \times \mathbf{B}$ drift (see Figure 5.1). Such a drift could in principle be either axially towards or away from the anode. In particular, a wave structure would by necessity need to obey an azimuthal periodicity requirement of the form $f(\theta) = f(\theta + 2\pi)$, forcing the wave to fit an integer number of wavelengths in the circumference of the discharge channel. Additionally, in the case of static magnetic fieldsFaraday's Law $\oint \vec{E} \cdot \vec{dl} = 0$ precludes a non-zero azimuthal field component all the way around the azimuth, so any azimuthal field component must reverse polarity periodically so as to cancel out over the full 2π of the channel. This means that to produce net axial transport toward the anode, there must be an electron density perturbation associated with the field fluctuation, and it must be in phase such that regions of larger density occur where the axial drift is toward the anode, so that on average more electrons are swept toward the anode than away from it.

The fact that such wave structures are visible to the naked eye (or rather to a high-speed camera in the visible wavelengths) indicates that there is a propagating region with elevated light emission, caused by the emission of photons from ionization and excitation events between electrons and xenon neutrals in the discharge channel. The spokes reverse their direction of propagation when the magnetic field polarity is reversed, clearly linking them to electron motion since the ions are too massive to be affected by the Hall thruster magnetic field, and the spoke structures are visible through bandpass filters at both xenon neutral and ion emission lines. Elevated rates of ionization and excitation indicate regions of elevated electron temperature, electron density, neutral density, or combinations of the three. If there

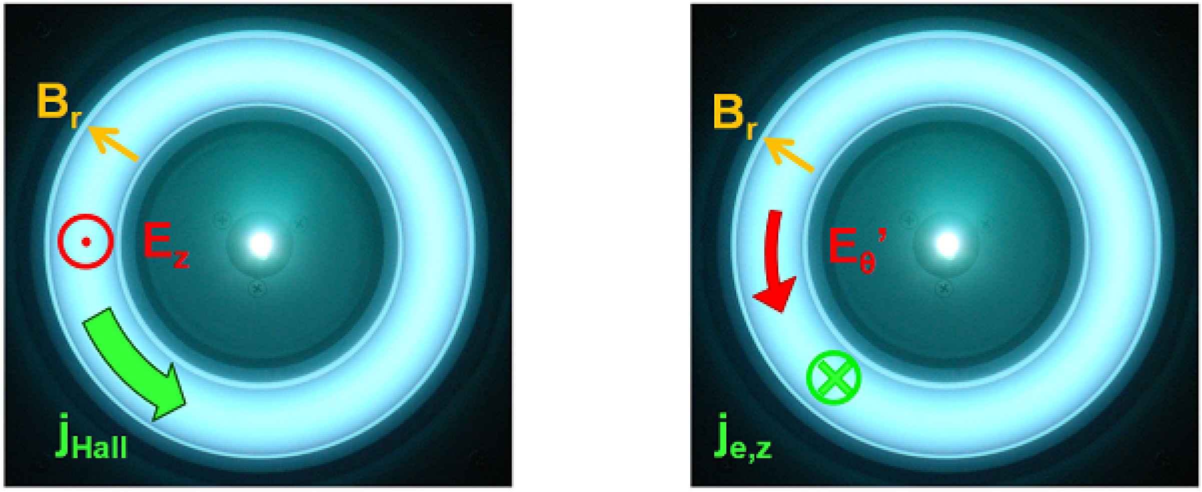

Figure 5.1. Left, the typical applied axial electric and radial magnetic fields in a Hall thruster produce an azimuthal $E \times B$ drift, the eponymous Hall current. Right, the presence of an azimuthal electric field component E'_θ, induced as part of plasma turbulence, will in concert with the radial magnetic field produce an axial drift component.

are indeed electron density fluctuations associated with the spokes, plasma potential fluctuations will follow, and if the oscillations are in phase then the spokes are a viable transport mechanism. Such measurements were first made by Janes, confirming the presence of fluctuations in potential and density in a Hall thruster and that they were in phase with sufficient amplitude to account for the bulk of the observed transport in the thruster.[5]

5.1.1 Video postprocessing for visualization of rotating spokes

The high-speed videos analyzed in this chapter are large, each with tens of thousands of frames, and it is difficult to pull a great deal of information out of them by analyzing them one frame at a time. For this reason much of this chapter will deal with discrete Fourier transforms (DFTs) of the videos to extract the main oscillatory behaviors of the videos as a whole. However, these analysis techniques are sufficiently abstract that it is worth spending some time visualize the spoke structures as best as possible in the raw video, to build a sense of familiarity for interpreting the DFTs later. This section describes how to postprocess a sequence of images to cast the underlying spokes into stark relief. A step-by-step visual description of the full process is shown in Figure 5.2.

Consider a video as a 3-dimensional matrix of pixel values, with image pixel brightness given as a function of position and time,

$$p = p\left(i, j, k\right) \tag{5.1}$$

where i and j denote the pixel column and row within a single frame and k is an index denoting the frame itself within the video as a whole. Given this 3-D matrix of pixel intensities (pixel brightness, intensity and value will be used interchangeably for the quantity represented by p) define a mean image M as

$$M\left(i, j\right) = \frac{1}{N_k} \sum_k p\left(i, j, k\right) \tag{5.2}$$

where M is a 2-D matrix of pixel values composed of the the average intensities measured at each pixel over the course of an entire video. When watching a video, it is subtly apparent to the eye that there are two types of oscillation happening – the first is an overall oscillation of the total image's brightness on each frame, and the second is a rotating effect that at times, depending on the speed of video playback, may be dismissed as simply aliasing. This second oscillation is the one we are most concerned with, the rotating spoke mode, while the overall oscillation corresponds to the discharge current's breathing mode and will later be identified as an "$m = 0$" mode. To filter out the breathing mode without affecting the spokes the mean image M is used to generate a set of normalizing factors to be applied to each video frame. We define these normalizing factors X as

$$X_k = \sum_{i,j} M\left(i, j\right) / \sum_{i,j} p\left(i, j, k\right) \tag{5.3}$$

where we recall that k is the index of the video frame, so a unique normalizing factor is generated for each frame. This factor is multiplied across the corresponding raw video frame to brighten images that are dimmer overall than average and to dim images that are brighter overall than average, generating a new "normalized" video with a perfectly removed breathing mode and normalized pixels with values given by

$$p_{norm}\left(i,j,k\right) = X_k \, p\left(i,j,k\right) \tag{5.4}$$

In terms of the 2D DFT to be discussed later, this identically zeroes out the $m = 0$ column of the 2D FFT while leaving the other modes untouched. Raw images prior to normalization are shown in the first row of Figure 5.2, while the second row shows normalized images. This has little apparent effect in the image at this stage, but greatly improves the clarity of the images in the later rows.

After normalization, the images go through several steps aimed at improving contrast. The cathode tends to be an order of magnitude brighter than the rest of the thruster, often saturating the image sensor and making it difficult to discern any detail in the channel. From row 2 to row 3 in Figure 5.2 the cathode is cropped from the images. Manual cropping is certainly possible but a more elegant solution is to automate the procedure using the circle-fitting method of Kasa[24], which is fast and relatively simple to implement. Using Kasa's least-squares minimization method we fit a circle by calculating a mean channel radius from the image and defining a channel width outside which all pixels are set to zero. The Kasa fit is only accurate when the whole channel is captured; for a discussion of more robust circle-fitting algorithms when only part of the channel can be imaged we refer the reader to a comprehensive monograph on the subject by Chernov.[14]

Even without the cathode the contrast in the channel is still poor due to the large

DC image signal, given by the mean image M. The spoke oscillations often appear with a pixel intensity amplitude $< 10\%$ of the mean pixel intensity, so AC-coupling is required to view them clearly. From row 3 to row 4 the pixel values are AC-coupled as

$$p_{norm_{AC}}\left(i,j,k\right) = p_{norm}\left(i,j,k\right) - M\left(i,j\right) \tag{5.5}$$

At this stage the spokes become clearly visible, though still in grayscale. As a final step the grayscale image is colorized, to provide the eye with contrast in both brightness and hue. This happens from from row 4 to row 5, with red indicating brighter regions than the mean image and blue indicating dimmer regions. Subjectively, the spokes in the color image are much easier to perceive with the naked eye.

The bottom row in Figure 5.2 shows what will be called an $m = 3$ spoke mode, due to the three simultaneous bright spokes rotating around the channel. Different thrusters and different operating conditions may have different numbers of spokes that will be referred to according to their mode number m, as in Figure 5.3. A parameter study in Section 5.2 will examine some potential causes for the appearance of different spoke modes under different thruster operating parameters.

5.1.2 Observations of rotating spokes in several Hall thrusters

The clear observation of spokes at several operating conditions in the H6 motivated closer inspection of high-speed video of other Hall thrusters to verify the extent of the spoke instability. To date 5 different Hall thrusters have been imaged at PEPL, and all have demonstrated spoke modes. This section shows excerpted image sequences from video of the H6 and 3 other Hall thrusters postprocessed according to Section 5.1.1: the NASA 173Mv1,[12] the dual nested channel X2 Hall

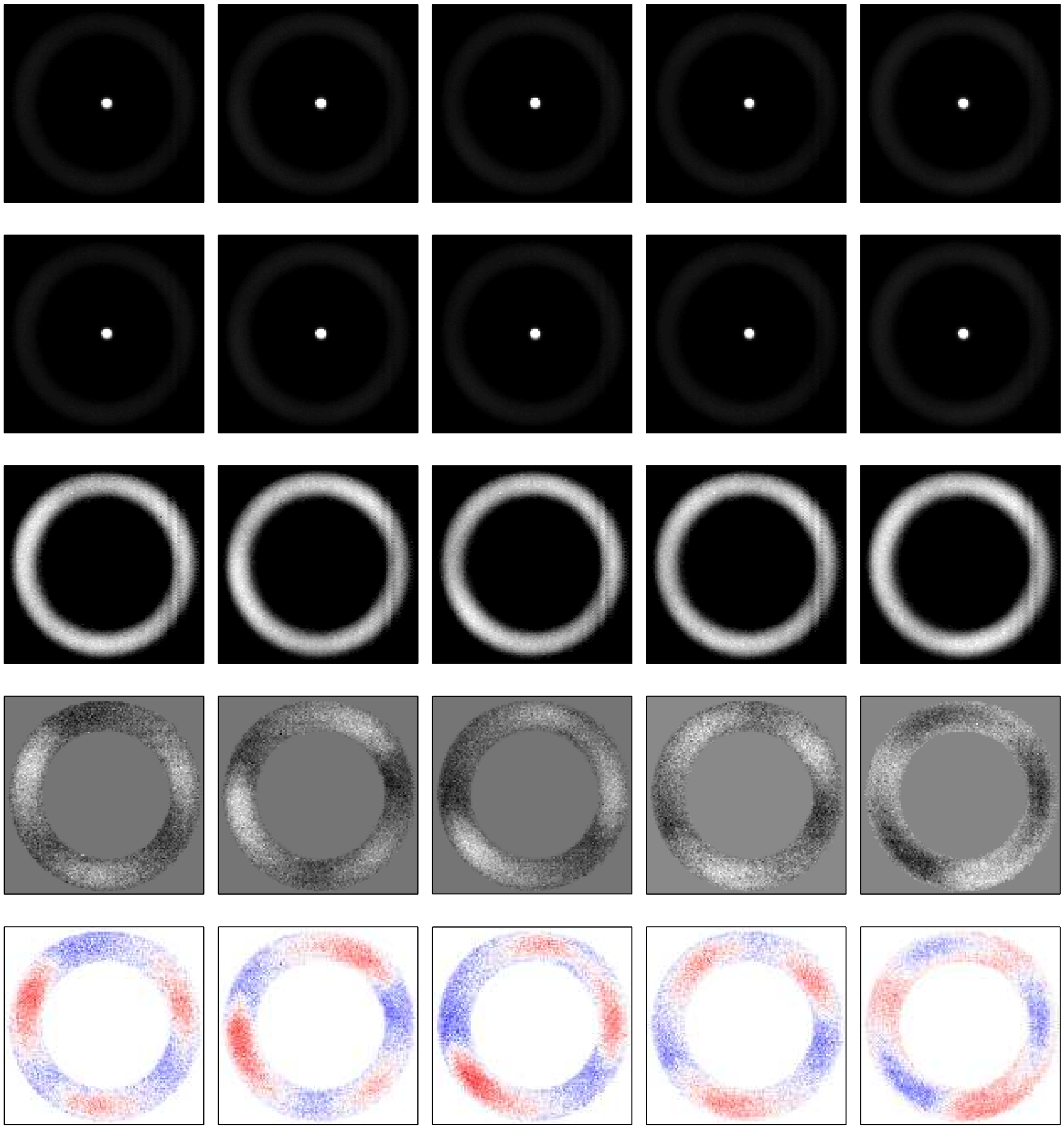

Figure 5.2. Sample images showing the high-speed video postprocessing technique used in this paper. In the top row, raw images of the H6 Hall thruster are in black and white with the central cathode as a very bright spot saturating the image. In the second row the images have been normalized relative to the mean image intensity over the whole video. In the third row the central cathode is cropped from the image, and in the fourth row the cropped image is AC-coupled by subtracting off the mean image. Both of these steps are aimed at improving contrast. Finally, the black and white AC-coupled image is converted to false color, where red indicates brighter and blue indicates dimmer regions than average. An $m = 3$ spoke mode rotating counterclockwise becomes visible in the final rows.

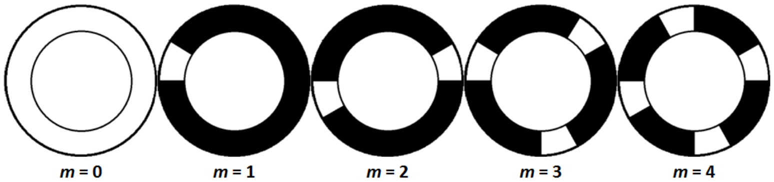

Figure 5.3. Physical meanings of the various spoke modes. White indicates luminous spokes propagating through an otherwise dark background. The mode number m indicates the number of spokes simultaneously present. For $m \geq 1$, the spokes propagate azimuthally in the $E \times B$ direction. For $m = 0$, the entire channel flashes in unison.

thruster,[7] and the Helicon Hall thruster[?] . The Busek BHT-600 has also been imaged and shows a clear $m = 1$ spoke, but since the video was taken only across a small slice of the discharge channel the spoke is difficult to make out in still images.

In addition to the imaging work of the author at PEPL, similar efforts at Princeton by Parker and Ellison have detected a spoke mode in a small cylindrical Hall thruster,[20,26] and Liu at the Air Force Institute of Technology has recorded azimuthal nonuniformities propagating at kilohertz frequencies in the Busek BHT-200.[19]. Video of the BPT-4000 also shows a low-frequency rotating spoke structure, though the exact mode number has not yet been identified.[?]

Note that the images in Figure 5.4 have purposefully been selected for their clear illustration of coherent rotation. An image sequence selected at random from a full video of tens of thousands of frames will often not display a pattern of this clarity – even with a strong spoke mode, unsteadiness in the plasma can often mask or disrupt the spoke structure. These images are shown because they are illustrative of and far more intuitive than the full detail of the 2D DFT of the spoke surface; however, for reliable spoke mode identification and strength and stability analyses the full DFT is preferred.

Across videos of several thrusters it is clear that different spoke modes may appear in the same thruster at different discharge voltages and discharge currents, and

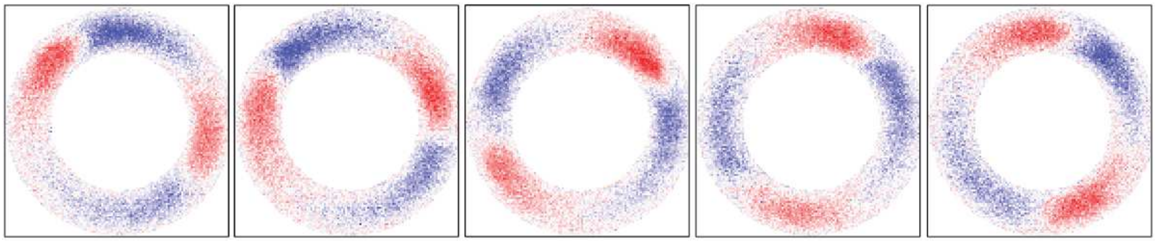

(a) H6 with a $m = 2$ mode at 300 V, 10 mg/s, 27000 fps

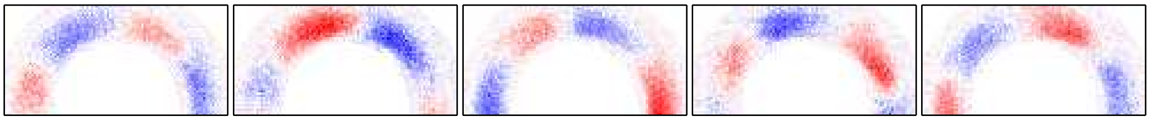

(b) NASA 173Mv1 (partial image) with a $m = 3$ mode at 300 V, 7 A, 45000 fps

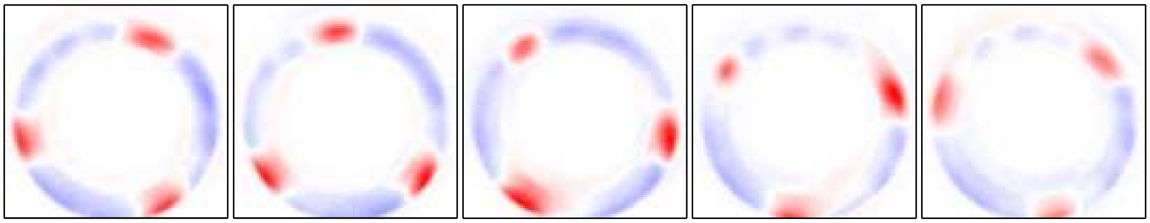

(c) Helicon Hall Thruster (HHT) with a very clearly delineated $m = 3$ mode at 200 V, 23.5 A, 162500 fps (every fourth image shown)

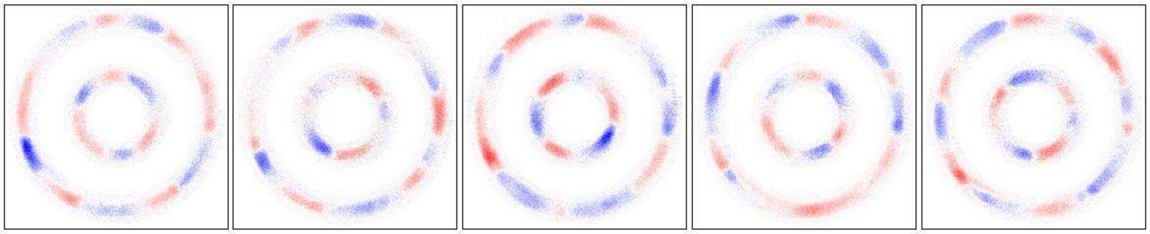

(d) X2 dual nested channel thruster with a $m = 3$ mode (inner channel) and a $m =$ 5-6 mode (outer channel) at 150 V (both channels), 6.6 A (inner channel) and 16.8 A (outer channel)

Figure 5.4. Postprocessed video frames showing rotating spokes in several Hall thrusters: (a) the H6 with a $m = 2$ spoke mode; (b) the NASA 173Mv1 with a $m = 3$ spoke mode (only part of the thruster was imaged to achieve a higher framerate with the 1024PCI camera); (c) the Helicon Hall thruster (HHT) with a very clear $m = 3$ spoke mode, imaged at 162,500 fps but with only every fourth image shown to make the rotation apparent; (d) the X2 dual nested channel Hall thruster with an $m = 3$ mode on the inner channel and a $m = 5 - 6$ mode on the outer channel. The spokes counter-rotate in the X2 due to reversed magnetic field direction between the channels, and the two channels are postprocessed into false color individually since the channels' distinct breathing mode frequencies require distinct normalizing factors in Equation 5.4.

likewise in different thrusters different spoke modes may appear even at identical discharge voltages and discharge currents. The spokes are in many cases unstable, and adjacent spoke modes may "trade off" unpredictably, such that for example an $m = 3$ mode may transition into an $m = 2$ mode and back into an $m = 3$ mode, all over a span of milliseconds. The implications of this in the Fourier spectra of the high-speed video are discussed in Section 5.1.3.2.

Higher spoke modes appear to form in physically larger thrusters; for example, in smaller thrusters such as the BHT-600 or in Princeton's CHT only an $m = 1$ mode has been observed, while in the X2 outer channel, the largest thruster yet imaged, the highest mode numbers of $m = 5 - 6$ appear. In the middle of the size range, the H6, 173Mv1 and HHT demonstrate modes between $m = 2$ and $m = 4$. The variation of spoke mode number with operating condition in the H6 is discussed in Section 5.2.

Finally, in literature on rotating instabilities the sign of m often denotes the handedness of rotation, for example positive m as rotation in the right-handed direction about a magnetic field. We denote here positive spoke modes $m \geq 1$ as rotating in the $E \times B$ direction. All modes discussed in this work are positive and rotate in the $E \times B$ direction, and as such have been observed to rotate in reversed direction when the electrical leads to the magnetic coils are switched, reversing the B-field polarity. The X2 thruster, with its reversed magnetic field polarity between the two channels, actually exhibits counterrotating spokes during normal operation due to the different opposite $E \times B$ directions between channels. While we have not observed $m < 0$ (e.g., a spoke mode rotating in the anti-$E \times B$ direction) in the H6 or any of the other Hall thrusters mentioned above, Smith has reported the detection of such a mode in the Stanford Hall thruster using floating emissive probes to measure plasma potential fluctuations.[3]

5.1.3 Fourier Analysis of High-Speed Video

The extremely large file sizes created by the high speed and high resolution of the Photron FASTCAM cameras used in this work (see Table 3.1) motivate analysis in the frequency domain. Thus, rather than detailed examination of individual images as above, for the most part later analysis will focus on power spectra derived from discrete Fourier transforms (DFTs) of the thruster discharge channel to characterize the modes and frequencies of oscillations. The DFT is calculated using the fast Fourier transform (FFT) algorithm and is also sometimes simply referred to as the FFT. The particular implementation used here is the built-in '*fft*' command in MATLAB version r2011a.

5.1.3.1 Use of the 2D discrete Fourier transform (DFT)

In general, just as the DFT of a 1-D signal like the discharge current may be shown as as a 1-D line on a coordinate grid, the full DFT of a 3-D signal like a video requires a 3-D representation. This is neither practical nor terribly informative, so we will simplify this 3-D representation in several ways. First, since this work focuses on an azimuthally propagating instability, we will consider the pixel values p from Eqn. 5.1 in polar coordinates, i.e.,

$$p = p\left(r, \theta, k\right) \tag{5.6}$$

We will furthermore restrict our analysis to a specific region, the discharge channel, where we will choose to neglect the radial dependence of pixel brightness. To accomplish this we isolate the annular region of the discharge channel in each video frame and further divide the 360 degrees of azimuthal angle into several discrete angular bins, denoted by the index b below, and deal with averaged pixel intensities $\bar{p}$ in each bin defined as

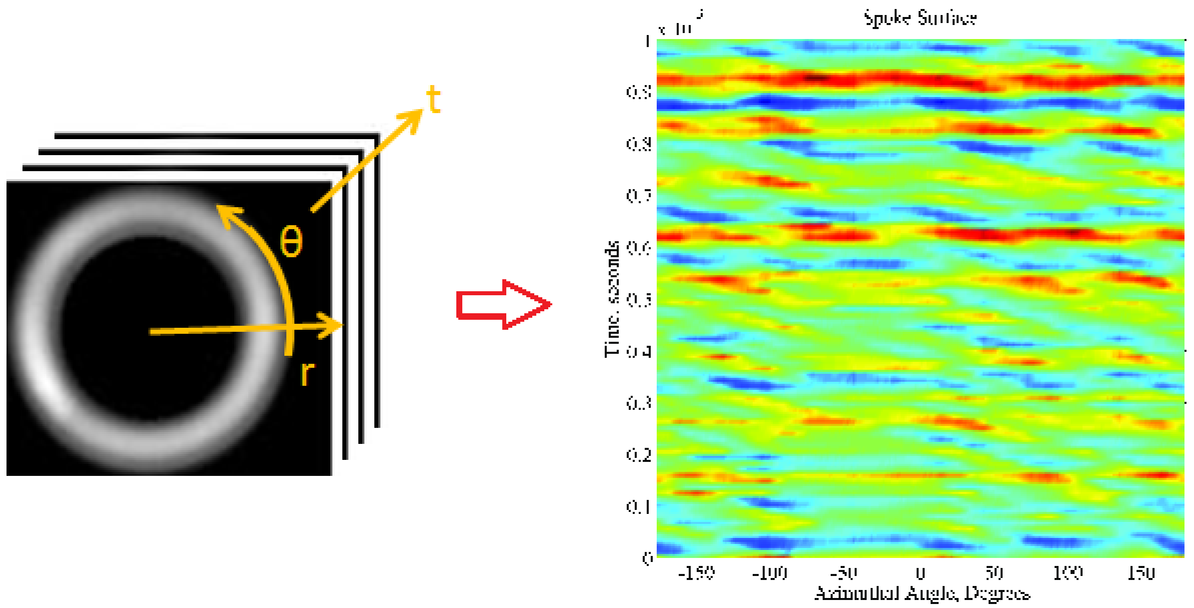

Figure 5.5. A video, represented as a 3D matrix of pixels in radius, angle and time, (left) is collapsed into a 2D spoke surface (right) by dividing the annular discharge channel into a number of discrete bins and averaging over the radial variation within each bin. The resulting spoke surface has a number of columns equal to the number of azimuthal bins and rows equal to the number of video frames. The angled parallel striations in the image correspond to spoke modes propagating azimuthally with time, while horizontal striations correspond to the breathing mode appearing in unison across the entire channel.

$$\bar{p}\left(\theta_b, k\right) = \frac{1}{N_b} \sum_{r=R_i}^{R_0} p\left(r, \theta_b, k\right)$$

where N_b is the number of pixels in the b^{th} bin. This reduces the video from a 3-D matrix of images to a 2-D plane in angle and time, dubbed the "spoke surface" (see Figure 5.5).

The spoke surface is amenable to a 2D DFT which can be physically interpreted in terms of the wave structures present in the thruster discharge. To compare, a 1D DFT breaks a 1D signal down into a finite series of sinusoidal basis functions with different amplitudes. These are necessarily functions of the single signal variable, usually time, and represent oscillations in time. By contrast, the 2D DFT breaks down a 2D signal, in the case of the spoke surface a function of time and angle, into three different kinds of oscillations: angularly constant signals that vary in time (like the $m = 0$ mode discussed later), angularly varying signals constant in time (for example, if one azimuthal location is consistently brighter throughout a video), and those oscillations that vary in both dimensions, linking time and angle. These last are waves propagating azimuthally around the discharge channel.

The DFT of the spoke surface generates a plane like the one at left in Figure 5.6. The DFT has the same dimensions as the original discrete signal, so a one second video with 100,000 images has a DFT with rows corresponding to frequencies from 1 - 99,999 Hz, with the last row reserved for DC or 0 Hz signals. Likewise, for an azimuthal resolution of 2 degrees or 180 azimuthal bins, the DFT columns correspond to sinusoids with wavelengths from (1 - 179) / 2π radians, with a column reserved for “zero” wavelength or an oscillation in unison across the entire 2π of the discharge channel.

For the high frequency-space resolution of these videos, noise in the signal can make interpretation of the DFT difficult. To filter the signal in frequency space, the set of DFT frequency components in a given frequency range are assumed to consist of a normal distribution of amplitudes. Within each of these ranges, a mean frequency and standard deviation are calculated, and both the mean and upper and lower bounds of a 95% confidence interval (i.e., 3 standard deviations on each side) are plotted. This can be seen at right in Figure 5.6, where the mean is the bold line and the confidence interval is spanned by the two lighter lines for each oscillatory mode. The exact width of the frequency range used for filtering varies depending on the dataset, but a minimum of 50 elements per range and 50 filtering ranges per DFT are enforced. For a 1 s video with 1 Hz resolution this corresponds to a minimum range of 50 Hz. By inspection in Figure 5.6 this strikes a reasonable balance between

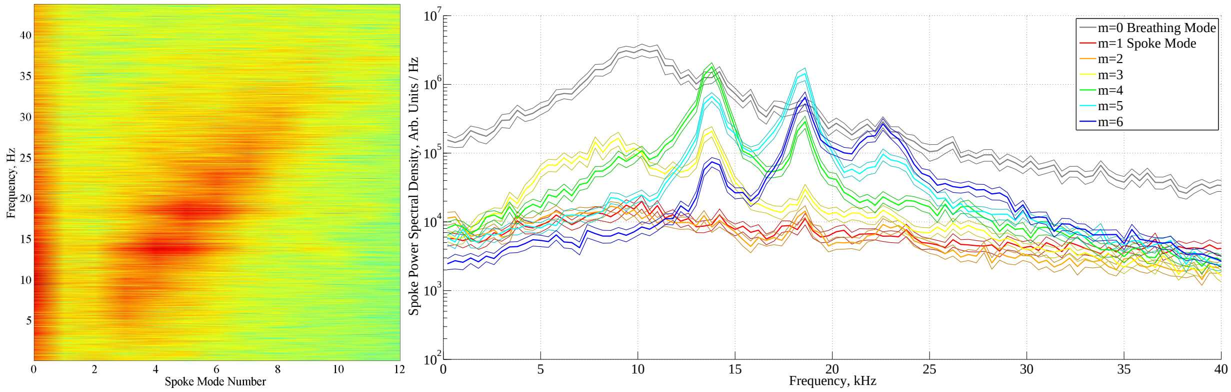

Figure 5.6. Left, the 2-D DFT of the spoke surface. Right, the strongest modes are broken out for 1-D representation. The $m = 0$ mode is dominant and appears as a vertical red stripe along the y-axis in the 2-D DFT at left and in gray at right.

smoothness and frequency resolution of the DFT.

The DFT matrix is symmetric and thus redundant across its centerline, since signals propagating clockwise at 1/4 revolution per frame are indistinguishable from those propagating counterclockwise at 3/4 revolution per frame. Only a small section of the unique quadrant of the DFT is displayed; the upper half of the frequency axis is truncated at the Nyquist frequency of the framerate, and the amplitudes of modes with wave numbers greater than about 8 are generally negligibly small.

The final Fourier representation of the thruster video, at right in Figure 5.6, labels the discrete mode numbers as $m = 0$, 1, 2 etc. These labels correspond to the number of simultaneous excitations around the channel at any one time:

$$m \equiv k_\theta R = \frac{2\pi R}{\lambda}$$

where k is the wavenumber and R is the mean radius of the discharge channel. There is some smearing of a given mode's frequency peak into the other modes, but as explained in Section 5.1.3.2 this is an optical artifact and does not mean that several different modes are propagating at the same frequency. Instead the true mode at a given frequency is the dominant one with the largest peak. Here, the $m = 0$, $m = 4$

and $m = 5$ modes are strongest.

Physically, these modes in the DFT correspond to the breathing and spoke modes. The $m = 0$ mode is a unified oscillation across all 360 azimuthal degrees simultaneously, and is an excellent representation of the breathing mode and indeed the discharge current signal as a whole, matching the discharge current DFT almost exactly. The $m = 1$ mode is a single pulse propagating azimuthally. The $m \geq 2$ modes have m simultaneous spokes propagating around the channel.

The linear velocity v_m of spoke passage around the discharge channel for a spoke mode m (that is to say, a spoke mode with m spokes simultaneously present) is given for all $m \geq 1$ by its frequency peak f_m as

$$v_m = \frac{2\pi R f_m}{m}$$

For the H6 a $m = 1$ spoke mode with $f_1 = 1$ kHz travels at an approximate velocity $v_1 = 500$ m/s. The $^1/_m$ term in the linear velocity equation is because the 2D DFT gives a local frequency at a fixed azimuthal location – if m spokes are present, the local frequency is boosted by a factor of m compared to the global rotation frequency of any single spoke. Thus, a $m = 2$ spoke mode with $f_2 = 1$ kHz in the DFT only has a linear spoke velocity of 250 m/s, compared to 500 m/s for the $m = 1$ mode with the same frequency. Put another way, the $m = 2$ mode with $f_2 = 1$ kHz is actually composed of two spokes, each propagating at 500 Hz but spaced 180 degrees around the discharge channel so together they appear as a 1 kHz propagating wave at any fixed observation point in the channel. An isolated probe in the channel cannot distinguish between modes with different global frequencies that manifest at the same local frequency, but high speed video of the full discharge channel confidently distinguishes between different spatial modes in the same frequency range.

It is important to note that in general the camera's raw pixel output does not linearly map to visible light intensity. Non-linearity of the bit depth of the camera sensor causes the pixel output to asymptote and saturate at high incident fluxes. This can be accounted for by calibration if necessary. However, for the particular cases of imaging the Hall thruster presented here, the high frame rates used are sufficient to keep the light intensity reaching the camera well inside the linear regime. The exception to this rule is the cathode, which is often an order of magnitude brighter than the discharge channel and is generally saturated in high speed video. Since the cathode portion of the frame is not used for analysis, this does not affect the results presented here.

5.1.3.2 Interpretation of the 2D DFT

To further clarify the interpretation of the 2D DFT, we examine two demonstrative cases in Figure 5.7. The left DFT of Figure 5.7 is taken for a 600 V, 10 mg/s operating condition. This is one of several regular operating points in the H6 throttling table and is described in more detail by Reid.[25] This condition has a 65% total efficiency, yet harbors the strongest, most coherent spoke mode yet observed. The $m = 3$ and $m = 2$ spoke modes are strongest, at 8 and 3 kHz, respectively, and the $m = 3$ mode peak is over an order of magnitude higher than the $m = 0$ breathing mode, typically thought of as the strongest oscillation in the Hall thruster discharge. The appearance of several smaller peaks below the $m = 3$ peak is an artifact of the Fourier decomposition of the mode's structure.

Laid out azimuthally the visible pixel intensities on video do not form perfect sine waves, able to be accurately represented by a single frequency component, and as a result the DFT of the azimuthal profile of a spoke mode may include components

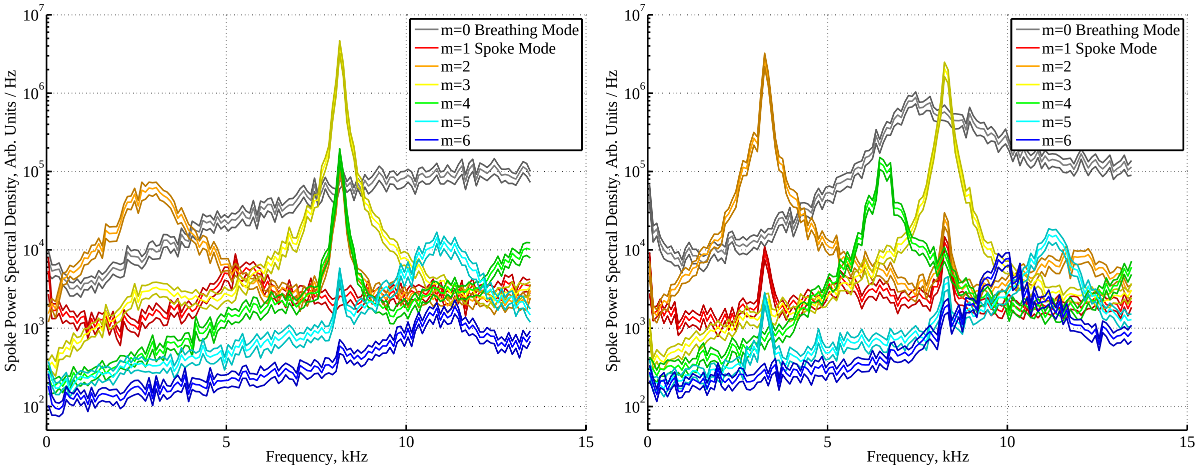

Figure 5.7. Example 2D DFTs illustrating several subtle features of mode analysis. The left DFT, taken from a 600 V, 10 mg/s operating condition with nominal magnetic field, shows a dominant $m = 3$ mode with turbulent smearing into the adjacent $m = 2$ and $m = 4$ modes. The right DFT, taken from a 300 V, 10 mg/s operating condition with slightly elevated magnetic field, shows some turbulent smearing but also beat modes and spatial harmonics of the fundamental modes.

of other spatial frequencies in order to build the experimentally observed shape. Consider the extreme case of a square wave or sawtooth, where even a structure of a single apparent frequency may have a Fourier decomposition with many frequency components in order to reproduce abrupt, non-sinusoidal edges in the wave structure. Just such abrupt edges are apparent in the high-speed video. Referring back to Figure 5.2, the bottom row of postprocessed spoke images shows much more clearly defined edges on the counterclockwise leading edges of any given spoke, corresponding to the wave front, than on the clockwise trailing edge. The same pattern can be observed in many videos. Thus, fundamental frequency peaks may “smear” into adjacent mode numbers, though the dominant peak with the highest amplitude is generally easy to spot. This plays out in the DFT on the left of Figure 5.7 as spurious $m = 2$ and $m = 4$ modes with the same frequency as the $m = 3$ mode.

The second DFT at right in Figure 5.7 is of a 300 V operating condition at 10 mg/s with a 3.2 A inner magnet current, slightly above the typical magnetic field strength for this point in the H6 throttling table. This mode illustrates several interesting features that complicate analysis of a 2D DFT. The $m = 2$ and $m = 3$ modes are still strongest, though the breathing mode is also relatively strong at this operating condition. Turbulent smearing of the $m = 2$ mode and the $m = 3$ modes is present, but several new features have crept in as well. The $m = 4$ and $m = 6$ peaks near 6.6 and 9.9 kHz are in fact the second and third spatial harmonics of the $m = 2$ mode at 3.3 kHz, while the $m = 5$ mode at 11 kHz is a beat frequency mode formed by the $m = 2$ and $m = 3$ modes – the mode number is the sum of the parent modes, while the linear velocity calculated from the frequency is the average of the parent mode linear velocities.

5.2 Influence of Operating Condition on Spoke Characteristics

Given the omnipresence of rotating spoke modes across several different thrusters and operating conditions, we next conducted a systematic parameter study to examine the spoke mode number, amplitude and propagation velocity's dependence on magnetic field strength and discharge voltage. Our examination consists of three datasets: a sweep of magnetic field strength at constant discharge voltage, a sweep of discharge voltage at constant magnetic field strength, and a sweep through discharge voltage with magnetic field settings optimized to minimize discharge current at each voltage. These three datasets are shown in the parameter space of B and V_D in Figure 5.8. Inner and outer magnet coil currents were maintained in a constant ratio throughout the study, so the shape of the magnetic field is unchanged throughout and the strength varies linearly with the coil current.

At each operating condition between one half and one full second of video was

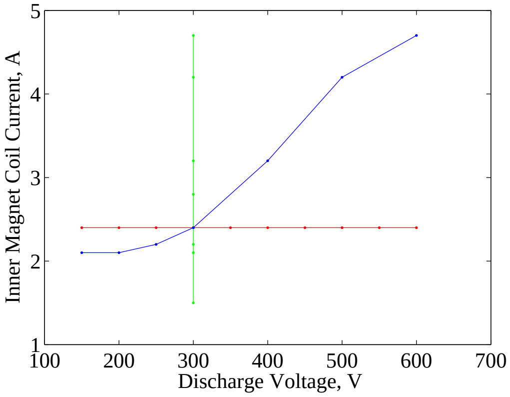

Figure 5.8. Parameter space for H6 operating regime investigation of rotating spokes. The three sweeps are designed to span the $B - V_D$ parameter space

acquired at 27,000 fps with 128x128 pixel resolution on the 1024PCI FASTCAM. These videos were in turn used to generate 2D DFTs of the high-speed video, with the results presented in Figure 5.9. Synchronous discharge current measurements were also collected for these conditions, but are not presented since in general the discharge current signal DFT is very similar to the $m = 0$ video signal DFT. The results are summarized in terms of the amplitude and frequency of the peaks for each mode. The harmonic, beat and turbulent smearing modes discussed in Section 5.1.3.2 are not included in the parameter study results, since they are artifacts of the fundamental modes introduced through the discrete Fourier decomposition.

The amplitude of the mode is given in arbitrary units, since it is a measurement of the pixel intensity signal recorded on the high-speed camera CCD. This signal is a function of thruster operating condition, camera aperture and framerate, and so in general is not directly comparable across different videos. However, for this study the camera framerate and aperture are held constant at 27,000 fps and f/2.8 to maintain comparable signal amplitudes.

5.2.1 Parameter Study Results

The results of the parameter study are presented in Figure 5.9. The results are presented in three columns corresponding to the three sweeps in parameter space shown in Figure 5.8. The first column corresponds to the vertical line (varied B), the second column to the horizontal line (varied V_D), and the third column to the diagonal representing optimized magnetic field settings at each discharge voltage.

I note before presenting the results that this assessment is intended to be more qualitative than quantitative; in particular, for many points the interval between data collection at different conditions was sufficiently brief due to test window constraints that an assumption of steady-state conditions was not rigorously verified. The low Nyquist frequency of the camera framerate (13.5 kHz for 27 kfps) also makes it difficult to identify higher spoke modes than $m = 3$ in many cases. Nevertheless, from the large selection of data we call attention to several key features:

1. **Higher spoke modes have higher frequencies and faster linear velocities.** The clearest trend in the results is that the $m = 3$ modes always travel faster than $m = 2$ at the same operating condition, and likewise where observed the $m = 4$ mode travels faster than $m = 3$. The $m = 4$ mode is at the threshold of the imaging capability of the 1024PCI camera and is only captured in a handful of cases where it drops below the Nyquist frequency of 13.5 kHz (for example, at the highest magnetic field settings in the first column of Figure 5.9).

2. **Spokes in general appear more brightly and stably at higher magnetic field strength.** A sharp, narrow peak in the DFT like the $m = 3$ mode at left in Figure 5.7 indicates a very stable, coherent mode. These sharp peaks tend

also to be the largest in magnitude, while the more broadband peaks (as for example the $m = 2$ mode in the same figure) tend to be of lower magnitude. Above about 2.5 A of magnet current, or above 300 V in the optimized-field parameter sweep, the spoke modes achieve parity or surpass the magnitude of the $m = 0$ breathing mode peak. This trend is not observed when the discharge voltage alone is increased and appears to be a function primarily of magnetic field. This is surprising since one might expect elevated electron temperatures at higher discharge voltages to increase the likelihood of visible emission from excited ions and neutrals. Since the magnetic field suppresses axial electron mobility, the spokes may instead strengthen in response to large gradients in plasma potential and plasma and neutral densities. Another possibility is that the spokes must strengthen with increased magnetic field to maintain the discharge across the magnetic barrier.

3. **Higher spoke modes m dominate at higher magnetic field strength.** This holds true in both the magnetic field sweep at constant voltage and in the optimized operating conditions, where we note from Figure 5.8 that the B-field strength increases approximately linearly with voltage. This is especially noticeable in the two highest magnetic field settings and two highest voltages with optimized magnetic field settings, where the $m = 3$ mode overtakes the $m = 2$ mode in amplitude by one to several orders of magnitude. The $m = 3$ rotational frequency falls below the breathing mode frequency at these points, perhaps suggesting that a spoke frequency below the breathing mode frequency enables strong spoke modes. The $m = 3$ spoke velocity also falls below the breathing mode at several operating conditions in the 100-300 V range as well, but at these lower voltages the spoke modes are so unstable and thus weak in

the DFT that it is hard to draw many conclusions. We will address low voltage operation further in the next section.

4. **Spoke velocity appears to decrease slightly and/or asymptote at higher magnetic fields.** This trend is clearest in the magnetic field sweep at constant voltage, but it also holds in the optimized operating conditions. The velocity is in general between several hundred and a few thousand meters per second, or between about 10-40% of the critical ionization velocity in xenon, a result consistent with previous results dating back to the initial findings by Janes and Lowder, who recorded values about 20% of the CIV. For comparison, the $E \times B$ velocity in the discharge channel is on the order of 10 km/s, so the spoke mode is much slower than the $E \times B$ drift.

The objective of this dissertation is to evaluate Hall thruster electron transport mechanisms to improve the predictive capability of models, and for the most part to that end we ignore questions of thruster performance. Nevertheless, we pause here to note that while the rotating spoke has long been associated with poorly performing operating conditions, often at low voltage operating conditions or conditions with poor ionization (i.e., mass utilization) efficiency, the operating condition with the strongest and most stable visible spokes is a 600 V, 10 mg/s 6 kW condition with a total efficiency of 65%, and spokes are also visible at nominal operation where the mass utilization efficiency has been measured at 93%. Clearly, the spoke is not necessarily a harbinger of poor performance, and there is some evidence based on this point and also the discussion of low voltage operation in Section 5.4 that spokes may be desirable for efficient thruster operation.

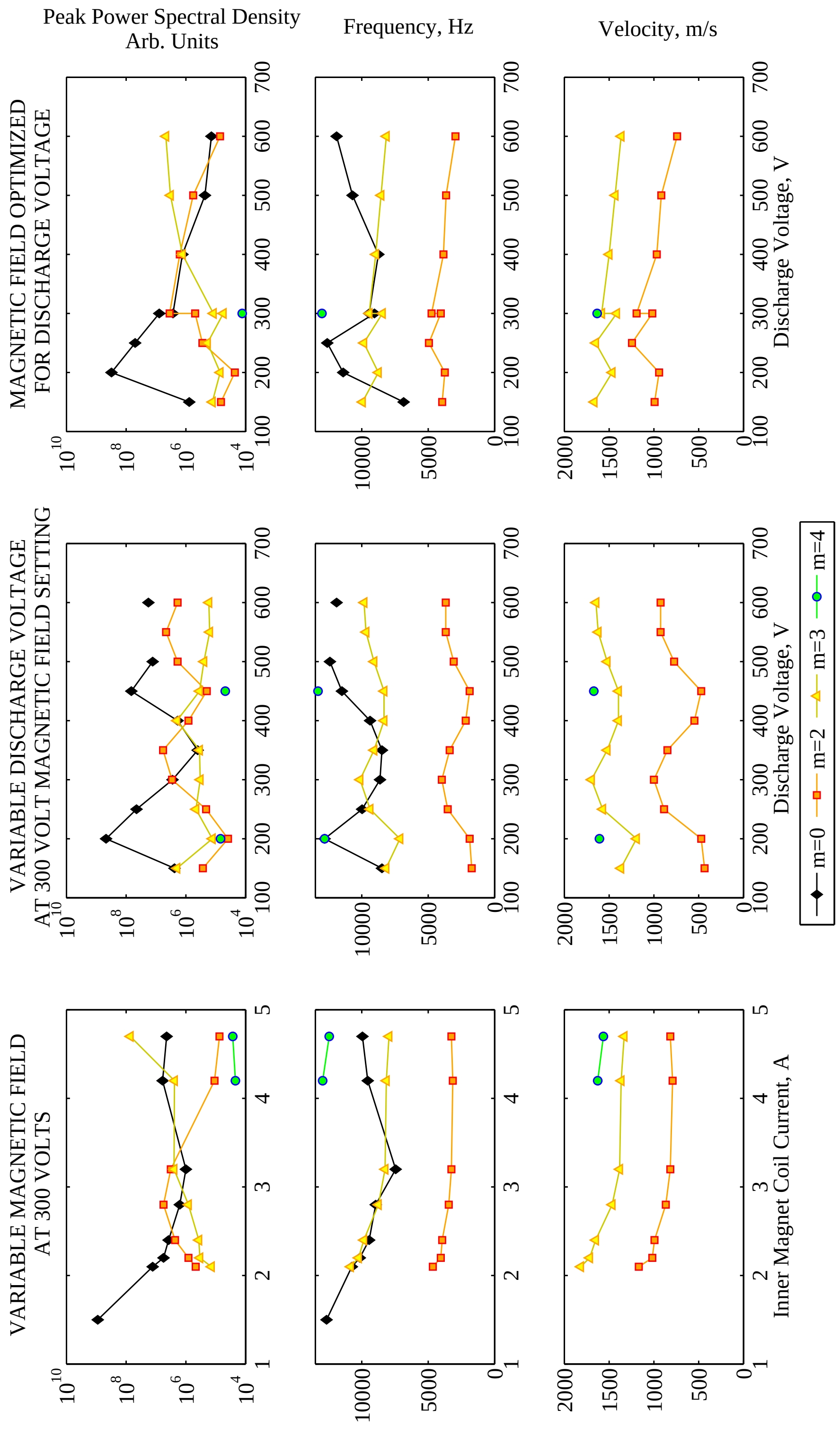

Figure 5.9. The results from a parameter study of varied magnetic field and discharge voltage are arranged in three columns, corresponding to the three sweeps through the parameter space from Figure 5.8, and three rows corresponding to the spoke power spectral density amplitude, rotational frequency and linear velocity. Salient features of the study are noted in Section 5.2.1.

5.3 Experimental Results of Operation with a Segmented Anode

The previous sections have shown the omnipresence of the visible rotating spoke instability across several Hall thrusters and several operating conditions, but they do not link it conclusively to electron transport. This requires direct measurement. Based on the similar velocity to the mode first observed by Janes, I hypothesized that these visible spokes were the optical wake of excited ions and neutrals behind a passing electron density wave, and that plasma potential fluctuations in this wave create azimuthal electric field components capable of driving an axial $E \times B$ drift current.

Since the spoke oscillations are periodic in the azimuth of the thruster channel, traditional discharge current measurements on a conventional ring-shaped anode are unlikely to detect them, as the measurement is effectively integrated over the full 2π of the Hall thruster channel. However, a segmented anode with isolated electrodes spaced azimuthally around the channel would be capable of resolving any azimuthally localized rotating points of electron current deposition. Using the theory of Yoshikawa also used by Janes, it is possible to calculate the total cross-field current carried by the spoke from the oscillation amplitude of the current on the anode segments. The following section presents this theory, the measurements of this current density, and the total calculated cross-field current due to the spokes. The measured current oscillations are linked to the visible rotating spokes by synchronous high-speed video with the current measurements.

The primary purpose of this effort is not to motivate the use of segmented anodes as a new Hall thruster design, though perhaps such an argument could be made; nor is it to claim that the exact level of cross-field current measured with a segmented anode at one operating condition means that the same level will be observed across all operating conditions or with a contiguous anode. Indeed, the introduction of a segmented anode to the H6 will inevitably disturb the operating characteristics of the thruster. Rather, the goal of the segmented anode is to demonstrate that the visible rotating spokes seen on high speed camera are more than an optical curiosity by presenting proof that the visible structures correspond to significant plasma fluctuations and that these plasma fluctuations carry an appreciable fraction of the total discharge current in parts of the Hall thruster plume. Having established this proof of concept with the segmented anode, only then will it be reasonable and prudent to invest time and resources in the further characterization of the instability throughout the plume in thrusters with conventional anodes where anomalous mobility mechanisms are known to exist.

5.3.1 Method of Calculation of Cross-field Electron Current due to Rotating Spokes

The basic principles that will be used to analyze turbulent cross-field transport follow the theoretical description of cross-field diffusion by Yoshikawa and Rose and are supported by the good agreement of this theory with the experiments of Janes and Lowder and of Meezan *et. al.*[1,5,22] Yoshikawa derived an explicit analytical description of cross-field electron transport for the case of a perturbation in plasma density with a concomitant electric field perturbation.

5.3.1.1 Basic Theory of Turbulent Transport

Consider a simple azimuthal fluctuation E_θ with an associated density fluctuation imposed on top of the typical axial E_z and radial B_r fields in the Hall thruster channel of the form

$$E_\theta = E_{\theta 0} + E_\theta^{'} sin\left(\theta\right) = E_\theta^{'} sin\left(\theta\right) \tag{5.7}$$

$$n = n_0 + n^{'} sin\left(\theta\right) \tag{5.8}$$

where $E_{\theta 0}$ is zero since Faraday's law requires $\oint \mathbf{E} \cdot d\mathbf{l}$ disappear in the absence of time-varying magnetic fields. The existence of azimuthal fields E_θ is well-documented in Hall thrusters even though they are fundamentally DC devices. The earliest and clearest demonstration of this effect is in the work of Janes and Lowder using azimuthally spaced floating emissive probes to measure plasma potential. This investigation demonstrated azimuthal electric field fluctuations E_θ' with magnitude approximately one-third of the applied axial electric field E_z ($E_\theta' = 6$ V/cm, $E_z =$ 17 V/cm).We neglect any magnetic fields induced by the Hall current, following calculations by Haas showing that these are negligible in comparison with the applied field.[16] The axial electron current density j_{ez} due to the new drift current in the axial $E_\theta \times B$ direction is given by

$$j_{ez}\left(\theta\right) = nqv_{ez} = nq\frac{E_\theta}{B} = \frac{q}{B}\left(n_0 E_\theta^{'} sin\left(\theta\right) + n^{'} E_\theta^{'} sin^2\left(\theta\right)\right) \tag{5.9}$$

where radial variation of the axial electron current density j_{ez} is ignored, e.g., $j_{ez}\left(r,\theta\right) = j_{ez}\left(\theta\right)$, and we consider the electron velocity to be guiding center motion purely in the direction of $\mathbf{E} \times \mathbf{B}$ with an axial component E_θ/B under an assumption that we are interested in timescales much longer than the electron cyclotron period. Such a set of field and density perturbations and the associated induced cross-field current are shown in Figure 5.10.

To find the average current density $\bar{j_{ez}}$ over the channel we integrate over θ from 0

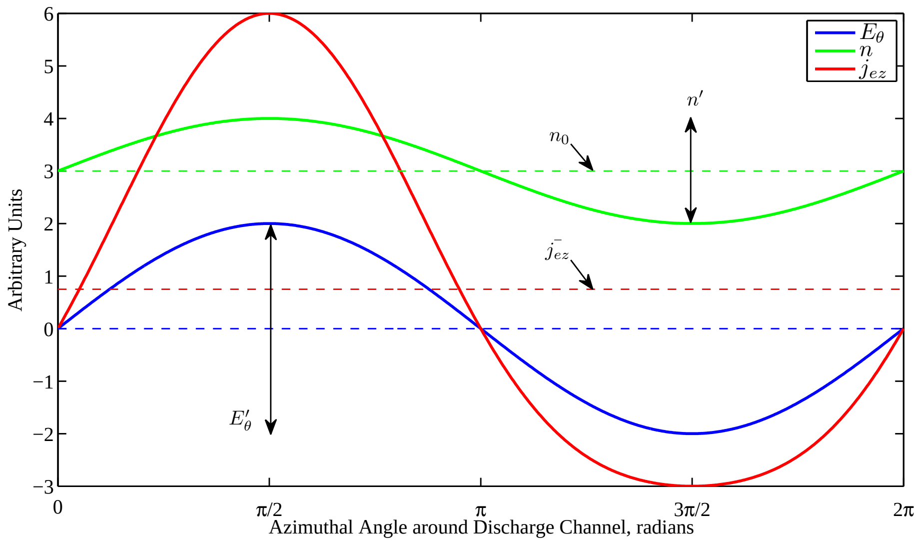

Figure 5.10. An azimuthal electric field fluctuation E_θ will couple with the applied radial electric field B_r to produce an axial E×B drift component. If there is a correlated density fluctuation $n = n_0 + n'$ associated with the electric field fluctuation, it will produce a net cross-field current j_{ez} with variable amplitude as a function of the azimuthal angle θ around the discharge channel. This example shows an $m = 1$ mode.

to 2π. The $sin\left(\theta\right)$ term on the RHS of Equation 5.9 disappears under this integration, leaving only the contribution due to the product of the two perturbed quantities:

$$\bar{j}_{ez} = \frac{1}{2\pi}\int_0^{2\pi} j_{ez}\left(\theta\right) d\theta = \frac{q}{2B} n' E'_\theta \tag{5.10}$$

The net transport across the magnetic field by this mechanism, if it exists, is then a second-order effect in the perturbed quantities. This fact is noted by both Janes and Yoshikawa. Nevertheless, the cross-field current by this mechanism may still be appreciable, for two reasons. First, the leading-order term is a sinusoid integrated over its period, so it disappears identically regardless of its amplitude, and second, that amplitude turns out to be rather large and as a result so is the product in Eqn. 5.10.

Later in Chapter V it will become apparent that multiple azimuthal modes may be present, either simultaneously or else trading off in alternating fashion. This does not affect the derivation since the expression for average current is integrated over a full period $(0, 2\pi)$. To see why, consider the derivation starting from Eqns. 5.7 and 5.8 but allowing for any number of higher modes to be present:

$$E_\theta = \sum_{m=1}^{\infty} E'_{\theta_m} sin\left(m\theta\right) \tag{5.11}$$

$$n = n_0 + \sum_{l=1}^{\infty} n'_l sin\left(l\theta\right) \tag{5.12}$$

The expressions for Eqns. 5.9 and 5.10 for $j_{ez}\left(\theta\right)$ and $\bar{j_{ez}}$ then become

$$j_{ez}\left(\theta\right) = \frac{q}{B}\left(n_0 \sum_{m=1}^{\infty} E'_{\theta_m} \sin\left(m\theta\right) + \sum_{m=1}^{\infty}\sum_{l=1}^{\infty} E'_{\theta_m} n'_l \sin\left(m\theta\right)\sin\left(l\theta\right)\right) \tag{5.13}$$

$$\bar{j_{ez}} = \frac{1}{2\pi}\int_0^{2\pi} j_{ez}\left(\theta\right) d\theta = \frac{q}{2\pi B}\int_0^{2\pi}\left(n_0 \sum_{m=1}^{\infty} E'_{\theta_m} \sin\left(m\theta\right) + \sum_{m=1}^{\infty}\sum_{l=1}^{\infty} E'_{\theta_m} n'_l \sin\left(m\theta\right)\sin\left(l\theta\right)\right) d\theta \tag{5.14}$$

The new multi-modal equation for $\bar{j_{ez}}$ is quite complex at this stage, but it simplifies extensively due to the orthogonality of the sinusoidal functions and the integration over a full period. Note that integration and summation commute, i.e.,

$$\int dx \sum_m a_m\left(x\right) = \sum_m \int a_m\left(x\right) dx$$

where $a_m\left(x\right)$ is the m^{th} term of some series of functions of the independent variable x. Recall also that because the sinusoids of different integer periods are orthogonal that the integral of their product over a full period in general disappears,

$$\int_0^{2\pi} \sin\left(m\theta\right)\sin\left(l\theta\right) d\theta = \begin{cases} \pi & l = m \\ \\ 0 & l \neq m \end{cases}$$

Given these two properties Eqn. 5.14 may be simplified as

$$\begin{aligned}
\bar{j}_{ez} &= \frac{q}{2\pi B}\left(n_0 \sum_{m=1}^{\infty} E'_{\theta_m} \int_0^{2\pi} \sin\left(m\theta\right) d\theta + \sum_{m=1}^{\infty}\sum_{l=1}^{\infty} E'_{\theta_m} n'_l \int_0^{2\pi} \sin\left(m\theta\right)\sin\left(l\theta\right) d\theta\right) \\
&= \frac{q}{2\pi B}\left(0 + \sum_{m=1}^{\infty} E'_{\theta_m} n'_m \int_0^{2\pi} \sin^2\left(m\theta\right) d\theta\right) \\
&= \frac{q}{2B} \sum_{m=1}^{\infty} E'_{\theta_m} n'_m
\end{aligned}$$

$$\bar{j}_{ez} = \frac{q}{2B} \sum_{m=1}^{\infty} E'_{\theta_m} n'_m \qquad (5.15)$$

thus revealing that the same functional form applies across one mode or several.

In the event that the peaks in the electric field and density are not perfectly in phase, i.e., $E_\theta = E'_\theta sin\left(\theta\right)$ and $n = n_0 + n' sin\left(\theta + \delta\right)$, a $cos\left(\delta\right)$ term appears in Eqn. 5.10. For approximately in phase signals the relation is still accurate to second order in δ, but if the electric field fluctuations are out of phase with the density or are randomly correlated (i.e., totally incoherent turbulence) then no net axial transport can occur. Density inhomogeneities form pressure gradients, and in the absence of a magnetic field one would expect that these could only be sustained by an electric field. Such a field would naturally be in phase with the density variation. With a magnetic field, the addition of a Lorentz force term in the momentum equation might be expected to alter this relationship. However, the experiments of Janes and Lowder found the fluctuations to be in phase, and while the fluctuations are not explicitly measured here they are also assumed to be in phase.

5.3.1.2 Yoshikawa's Relation between the Turbulent and Applied Electric Field

Yoshikawa derived an expression for the magnitude of the induced field fluctuation amplitude as a function of the density fluctuation and the applied axial field in a semi-infinite slab geometry assuming stationary ions, isothermal electrons, a pressure (really density, since $\nabla T = 0$) gradient, applied electric field, and a negligible self-magnetic field contribution due to charged particle motion.[1] Janes applied this expression to the geometry of a Hall thruster and expressed it as[5]

$$E_\theta^{'} = \frac{1}{4}\pi\frac{n^{'}}{n_0}E_z \tag{5.16}$$

The derivation of this expression is not trivial, and is given in much greater detail in Appendix A. The theory has given accurate predictions of fluctuating conditions in a Hall thruster in at least two experiments, the one by Janes mentioned above and a more recent experiment in the Stanford Hall Thruster by Meezan, also discussed in the appendix.[22]

5.3.1.3 Expression for Cross-field Current as a Function of Current Density Oscillation Amplitude

The expression for average spoke-induced cross-field current density $\bar{j_{ez}}$ and current density oscillation amplitude $j_{ez}\left(\theta\right)$ in Eqns. 5.10 and 5.7 assume knowledge of the amplitude of the induced fluctuations in azimuthal electric field E_θ' and plasma density n'. Given these induced fluctuations one can calculate both $\bar{j_{ez}}$ and $j_{ez}\left(\theta\right)$. However, the segmented anode does not directly measure either the electric field or density fluctuation. Nor is the mean current density measured by the segmented anode equal to $\bar{j_{ez}}$. Instead, instead it directly measures of the amplitude of current density oscillations at the anode $j_{ez}\left(\theta\right)$. As a result the calculation method is somewhat indirect. We postulate the existence of density and field fluctuations associated with the rotating spokes, following the findings of several previous authors.[5,8,20,26] Given the amplitude of the current density oscillations at the anode and Yoshikawa's relation between the electric field and density oscillations one can then calculate the current density $\bar{j_{ez}}$ attributable to the rotating spokes. The error bars associated with this method are significant and are discussed in Section 5.3.2.3.

Since other mechanisms including near-wall conductivity, classical transport and turbulent transport at higher frequencies unrelated to the spokes may all contribute to the total discharge current, the mean DC value of the current collected at each anode segment does not provide useful information other than to assess the overall uniformity of current deposition at the anode (discussed in Section 5.3.3.3). Only the magnitude of the current oscillations, the AC component of the segmented anode signal, is useful for cross-field current calculations.

The first step is to use Yoshikawa's expression for the azimuthal field fluctuation E'_θ in terms of the density fluctuation n' to express $\bar{j_{ez}}$ and $j_{ez}\left(\theta\right)$ in terms of only one unknown fluctuating quantity. These expressions become

$$j_{ez}\left(\theta\right) = \frac{q\pi}{4B} E_z \left(n^{'} sin\left(\theta\right) + \frac{\left(n^{'}\right)^2}{n_0} sin^2\left(\theta\right) \right) \tag{5.17}$$

$$\bar{j_{ez}} = \frac{q\pi}{8} \frac{E_z}{B} \frac{\left(n^{'}\right)^2}{n_0} \tag{5.18}$$

Note that Yoshikawa's derivation used a Cartesian slab geometry with uniform orthogonal applied fields, so the value of B referred to in the equation does not map perfectly to a cylindrical geometry with a solenoidal magnetic field. For calculation purposes, B_r will be used. In this expression the quantities n_0, E_z and B (B_r) are already known in the H6, leaving only n' as an unknown quantity. We will use Eqn. 5.17 to find $n^{'}$ and use it to calculate $\bar{j_{ez}}$ and thus the fraction of the total discharge current due to this mechanism.

Equation 5.17 is difficult to solve exactly because we do not have an analytic expression for $j_{ez}\left(\theta\right)$ – it is only evaluated every 30 degrees at the 12 discrete anode segments. The derivation of Equation 5.16 by Yoshikawa assumed that $n^{'} \ll n_0$, though Janes found excellent agreement with it even for experimental values of $n^{'}/n_0 = 0.5$.[5] Following the small perturbation assumption, we approximate

$$j_{ez}\left(\theta\right) \approx \frac{q\pi}{4B} E_z n^{'} sin\left(\theta\right) \tag{5.19}$$

where we have neglected the second term on the RHS in Eqn. 5.17. Again, since $j_{ez}\left(\theta\right)$ is a discrete function this still does not give a nice expression for n'. However, the root-mean-square (RMS) can be calculated easily for a discrete signal. Taking the RMS of both sides yields

$$\begin{aligned}
\left(j_{ez}\left(\theta\right)\right)_{RMS} &= \sqrt{\frac{1}{2\pi}\int_0^{2\pi}\left(\frac{q\pi}{4B}E_z n^{'} sin\left(\theta\right)\right)^2 d\theta} \\
&= \frac{1}{\sqrt{2}}\frac{q}{4B}E_z n^{'}\sqrt{\pi\int_0^{2\pi}\sin^2\left(\theta\right)d\theta} \\
&= \frac{1}{\sqrt{2}}\frac{q\pi}{4B}E_z n^{'}
\end{aligned}$$

$$\left(j_{ez}\left(\theta\right)\right)_{RMS} = \frac{1}{\sqrt{2}}\frac{q\pi}{4B}E_z n^{'} \tag{5.20}$$

Of the quantities in Equation 5.20, $\left(j_{ez}\left(\theta\right)\right)_{RMS}$ can be calculated from the anode segment values, the electric field E_z is known from internal plasma potential measurements in the H6 discharge channel by Reid[25], and the magnetic field magnitude B (really the value of the radial component of the magnetic field B_r) is readily obtained from finite element simulations in Infolytica's MagNet software or from direct measurement by gaussmeter in the thruster itself. With these values in hand one can calculate the density perturbation $n^{'}$ and from it the total spoke-induced cross-field electron current $\bar{j_{ez}}$ from Eqn. 5.18. Using Eqns. 5.18 and 5.20, one can see that the relation is

$$\bar{j}_{ez} = \frac{4}{q\pi}\frac{B}{E_z}\frac{1}{n_o}\left(j_{ez}\left(\theta\right)\right)^2_{RMS} \tag{5.21}$$

Note that this equation indicates that large amplitude electron current oscillations correspond to large average values of cross-field current.

The above derivation was performed for a single perturbation of a $m = 1$ sinusoid, but it is valid for a superposition of different modes, subject to the same assumption of $n'/n_0 \ll 1$. Derivation of the corresponding expression for a multitude of coexisting perturbations starts from Eqn. 5.13, reproduced here:

$$j_{ez}\left(\theta\right) = \frac{q}{B}\left(n_0\sum_{m=1}^{\infty} E'_{\theta_m}\sin\left(m\theta\right) + \sum_{m=1}^{\infty}\sum_{l=1}^{\infty} E'_{\theta_m} n'_l \sin\left(m\theta\right)\sin\left(l\theta\right)\right)$$

Substituting in for E'_θ in terms of n' from Eqn. 5.16 yields

$$j_{ez}\left(\theta\right) = \frac{q}{B}\left(\frac{\pi}{4}E_z\sum_{m=1}^{\infty} n'_m\sin\left(m\theta\right) + \frac{\pi}{4}E_z\sum_{m=1}^{\infty}\sum_{l=1}^{\infty}\frac{n'_l n'_m}{n_0}\sin\left(m\theta\right)\sin\left(l\theta\right)\right)$$

We again assume $n'/n_0 \ll 1$ and neglect the second term on the RHS:

$$j_{ez}\left(\theta\right) \approx \frac{q\pi}{4B}E_z\sum_{m=1}^{\infty} n'_m\sin\left(m\theta\right)$$

Once again taking the RMS of each side of this equation,

$$\begin{aligned}
\left(j_{ez}\left(\theta\right)\right)_{RMS} &= \sqrt{\frac{1}{2\pi}\int_0^{2\pi}\left(\frac{q\pi}{4B}E_z\sum_{m=1}^{\infty} n'_m\sin\left(m\theta\right)\right)^2 d\theta} \\
&= \frac{1}{\sqrt{2}}\frac{q}{4B}E_z\sqrt{\pi\int_0^{2\pi}\sum_{l=1}^{\infty}\sum_{m=1}^{\infty} n'_l n'_m \sin\left(l\theta\right)\sin\left(m\theta\right)d\theta} \\
&= \frac{1}{\sqrt{2}}\frac{q}{4B}E_z\sqrt{\pi\sum_{l=1}^{\infty}\sum_{m=1}^{\infty} n'_l n'_m \int_0^{2\pi}\sin\left(l\theta\right)\sin\left(m\theta\right)d\theta} \\
&= \frac{1}{\sqrt{2}}\frac{q\pi}{4B}E_z\sqrt{\sum_{m=1}^{\infty} n'^2_m}
\end{aligned}$$

$$\left(j_{ez}\left(\theta\right)\right)_{RMS} = \frac{1}{\sqrt{2}}\frac{q\pi}{4B}E_z\sqrt{\sum_{m=1}^{\infty} n_m'^2} \tag{5.22}$$

Recall Eqn. 5.15 for $\bar{j_{ez}}$ in the case of several superimposed spoke modes, reproduced here:

$$\bar{j_{ez}} = \frac{q}{2B}\sum_{m=1}^{\infty} E_{\theta_m}^{'} n_m^{'}$$

Substituting in for E_θ' in terms of n' yields:

$$\bar{j_{ez}} = \frac{q\pi}{8B}\frac{1}{n_0}E_z\sum_{m=1}^{\infty} n_m'^2 \tag{5.23}$$

Comparing Eqn. 5.23 and Eqn. 5.22, it is apparent that the same relation between the oscillation amplitudes and the average cross-field current holds from Eqn. 5.21.

5.3.2 Measurements of Discharge Current Oscillations

Because of the thermal challenges of operating the thruster with the retrofitted segmented anode, only the results from a 300 V, 10 mg/s (3 kW) operating condition are presented here. Operating at higher currents, for example the nominal 300 V, 20 mg/s 6 kW condition, or higher voltages, such as the 600 V, 10A 6 kW condition, led to premature failure of the segmented anode due to arcing or melting of current carrying lines.

The results of thruster operation at the 3 kW condition were quite successful, however, and show large amplitude current oscillations traveling in the counterclockwise or $E \times B$ direction from segment to segment, as in Figure 5.11 showing excerpts of the current signal to three adjacent segments, numbers 6-8. The anode segments

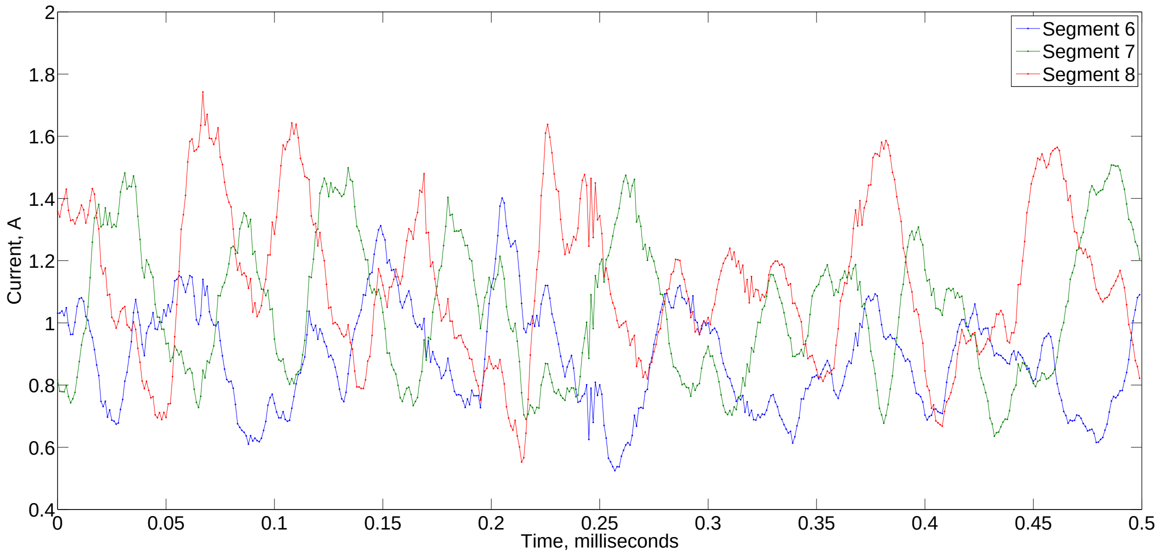

Figure 5.11. Current measured on three adjacent anode segments. The slight visible offset between signals indicates propagation of the wave structure, from segment 8 (red) toward segments 7 (green) and 6 (blue). Only three segments are shown for clarity, but all segments demonstrated large oscillations compared to the mean discharge current.

are numbered clockwise with segment 12 at the top as seen from the view of the thruster firing in Figure 3.3.

These oscillations travel at the spoke frequency calculated from high-speed video (Figure 5.12). Over all segments the current oscillation amplitude is about 30% of the average measured total current. Both the mean DC discharge current levels of each segment and the amplitude of their AC oscillations, calculated as $\sqrt{2}$ times the root-mean-square (RMS) of the AC-coupled signal, are shown in Table 5.1 and Figure 5.13.

5.3.2.1 Method for Decoupling of Breathing and Spoke Mode Oscillations

The current signal on each anode segment is due to a combination of the breathing and spoke modes, but $\left(j_{ez}\left(\theta\right)\right)_{RMS}$ must be determined from the oscillation amplitude due to the spoke modes only. Fourier analysis of the current to the anode segments later in Section 5.3.3.1 will show that the breathing mode $m = 0$ current oscillation

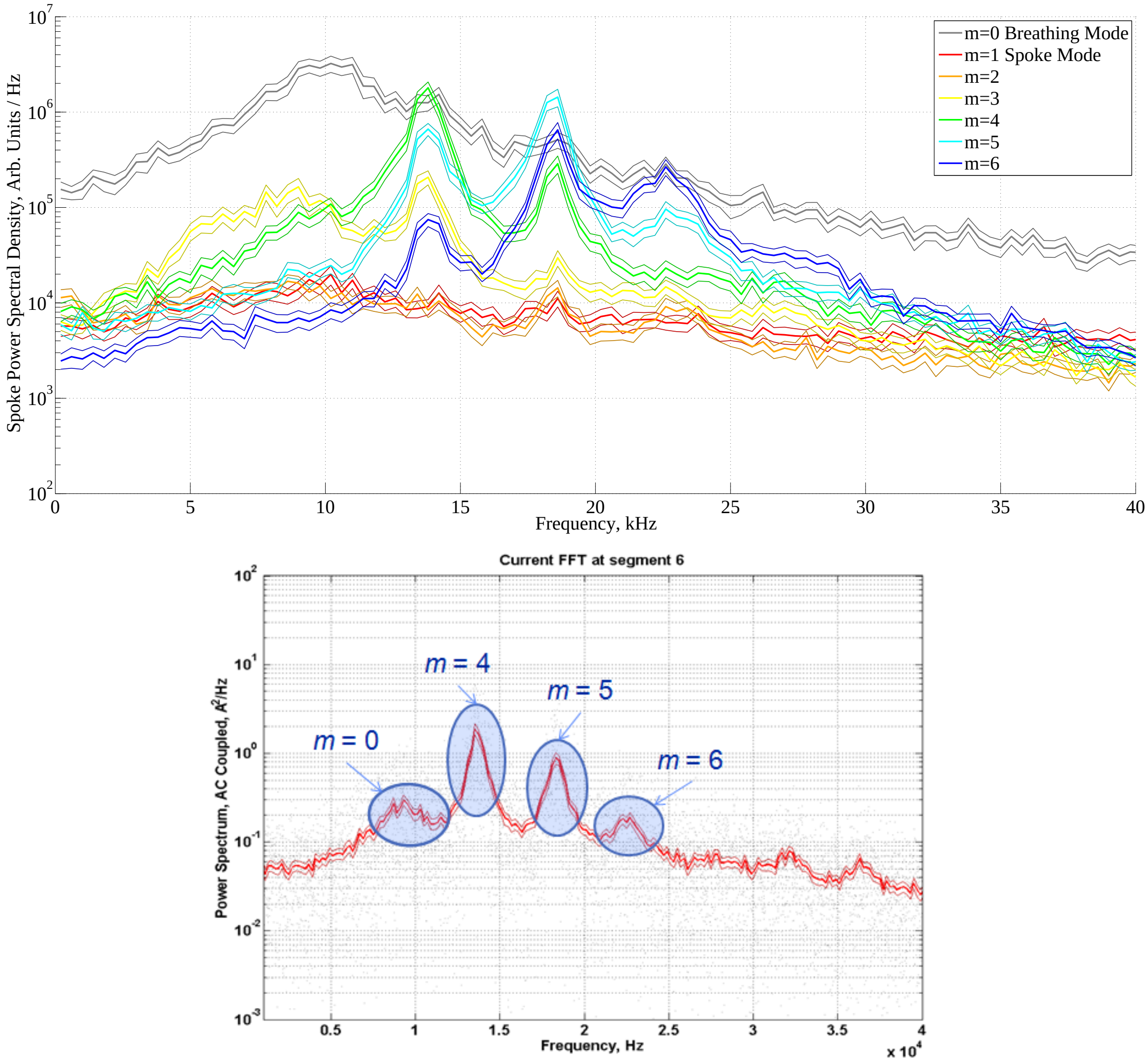

Figure 5.12. Selected modes from the high-speed video 2-D DFT showing the dominant oscillations present in the discharge. The $m = 0$ breathing mode at 10 kHz is dominant, but the $m = 4$ and $m = 5$ modes at 14 and 18 kHz are close behind. The DFT of one of the individual anode segments, segment 6, shows that the measured current oscillations are at the same frequencies as the visible spokes. Without the information from the FASTCAM, it would be impossible to distinguish between the spoke modes on the current signal. Note also the small amplitude of the 10 kHz breathing mode on the anode segment's current signal; this is discussed in more detail in Section 5.3.3.1.

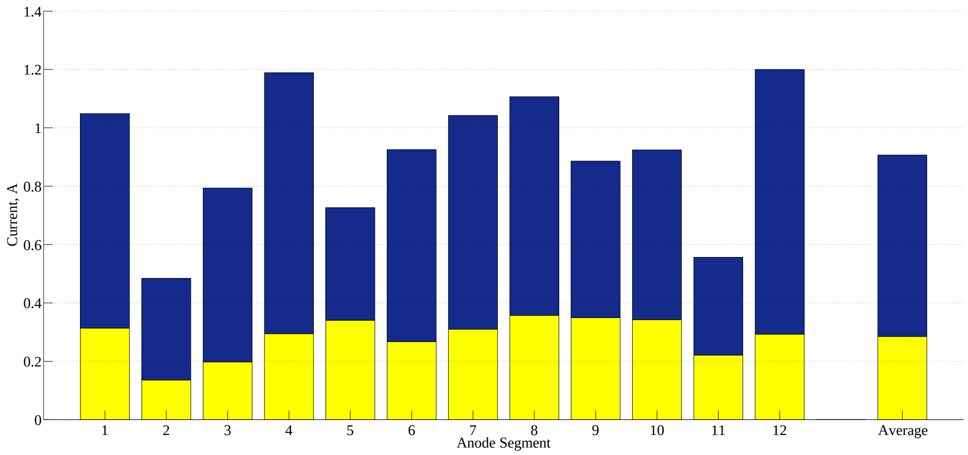

Figure 5.13. Mean discharge current (blue) and oscillation amplitudes (yellow) across the 12 anode segments. A discussion of potential causes of the azimuthal nonuniformity is given in Section 5.3.3.3.

Anode Segment	DC Amplitude, A	AC Amplitude ($\sqrt{2}\times$ RMS), A	AC/DC Ratio, %
1	1.05	0.31	30
2	0.49	0.14	28
3	0.79	0.20	25
4	1.19	0.29	25
5	0.73	0.34	47
6	0.93	0.27	29
7	1.04	0.31	30
8	1.11	0.36	32
9	0.89	0.35	39
10	0.92	0.34	37
11	0.56	0.22	40
12	1.20	0.29	24
Average	0.91 A	0.29 A	32 %

Table 5.1. Mean discharge current, oscillation amplitude and their ratio across all 12 segments, tabulated from Figure 5.13. The cause of the spread in the DC amplitude is uncertain, but the ratio of oscillation amplitude to mean local discharge current stays fairly steady across these nonuniformities.

occurs in phase across all 12 segments, while the spokes are in general not in phase from one segment to the next. To this end, I use the same normalizing technique as on the video frames in Section 5.1.1 to remove the breathing mode oscillation while leaving the spoke modes intact, essentially treating the segmented anode as an effective 12-pixel image. I define a new series of normalizing factors X_t defined at each moment of data acquisition as the ratio of the mean discharge current $\bar{I_D}$ of each segment to the instantaneous discharge current I_t on each segment

$$X_t \equiv \bar{I_D}/I_t$$

and apply this normalization to each segment to scale away the $m = 0$ oscillations and isolate the spokes more fully. This method serves well by visual inspection in video postprocessing, and it makes a small correction to the segmented anode current measurements, on average about a 4% reduction in oscillation amplitude. Considering the small amplitude of the breathing mode compared to the spoke mode on the individual segments as shown in the single segment DFT in Figure 5.12, this fraction seems reasonable. With the normalizing correction applied, the amplitude of the spoke oscillations is taken to be $\sqrt{2}$ times the RMS value of the normalized current oscillations, shown in Table 5.2.

5.3.2.2 Calculation of the Cross-field Electron Current

Calculation of the spoke-induced cross-field current density from the oscillation amplitudes in Table 5.1 requires knowledge of the properties in the H6 discharge channel. These quantities have been measured by Reid and are presented here for reference and to acknowledge where appropriate the large error bars in these measurements, notably in the ratio of E_z/B_r. Figures 5.14 - 5.18 give the plasma density V_p, radial magnetic field magnitude B_r, plasma potential V_p, axial electric field strength

Segment Index	AC Amplitude ($\sqrt{2}\times$ RMS), A	Normalized AC Amplitude, A	% Change
1	0.313	0.306	-2.3
2	0.140	0.140	0.0
3	0.198	0.177	-10.6
4	0.294	0.289	-1.9
5	0.340	0.337	-1.0
6	0.267	0.250	-6.2
7	0.310	0.292	-5.8
8	0.357	0.348	-2.6
9	0.350	0.342	-2.3
10	0.342	0.319	-6.9
11	0.221	0.211	-4.4
12	0.293	0.288	-1.6
Average	0.285	0.274	-3.8%

Table 5.2. Anode segment current oscillation amplitudes before and after normalization of the breathing mode. The correction is small, about 4% on each segment, in line with the small power spectral density of the breathing mode compared to the spoke modes.

E_z and finally the ratio of E_z/B_r on the H6 channel centerline.[4,10,25].

Recall that the expression for the cross-field current density in terms of the oscillating current density from Eqn. 5.21is

$$\bar{j_{ez}} = \frac{4}{q\pi}\frac{B}{E_z}\frac{1}{n_o}\left(j_{ez}\left(\theta\right)\right)^2_{RMS}$$

From Figure 5.14, the unperturbed plasma density n_0 at the segmented anode surface is about 1×10^{17} cm^{-3}. From Figure 5.18, the value of E_z/B_r is approximately 10^5. Knowing the area of each anode segment, approximately 8.6 cm^2, the average normalized current oscillation 0.27 A above gives a RMS spoke current density oscillation of $(j_{ez})_{RMS} = 23$ mA/cm^2. Plugging these values into the above equation,

$$\bar{j_{ez}} = 40\, mA/cm^2$$

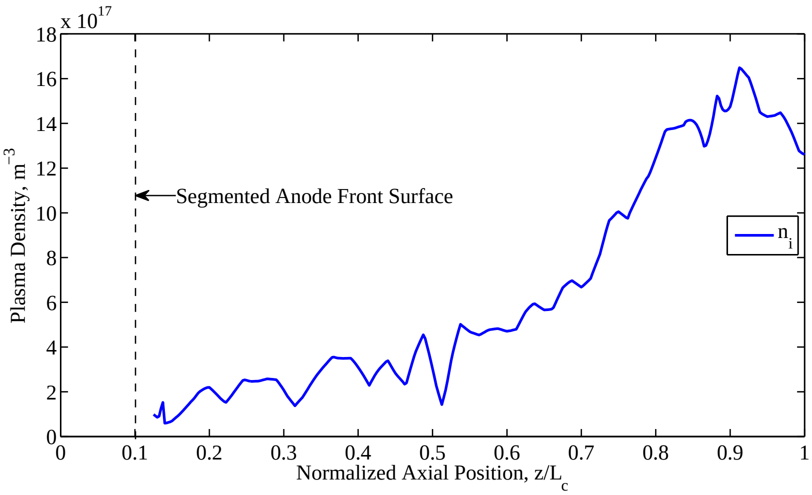

Figure 5.14. Plasma density on H6 channel centerline at 300 V, 10 mg/s. Near the segmented anode surface the density is about 1×10^{17} cm^{-3}.

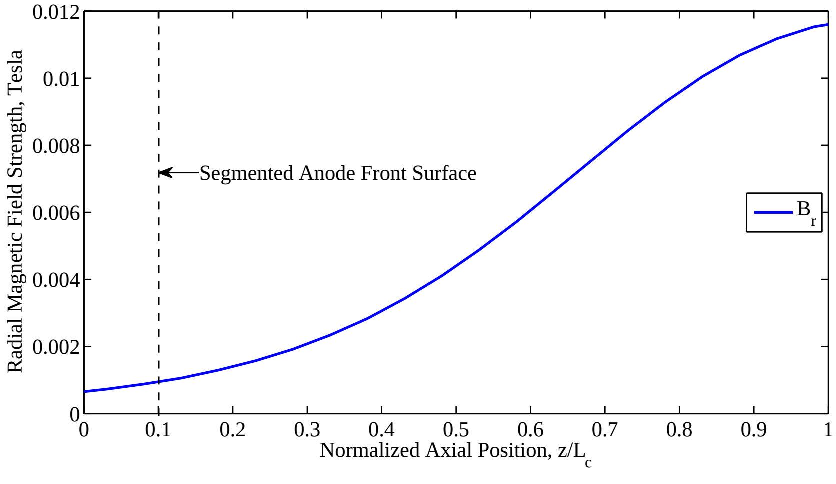

Figure 5.15. Simulated radial magnetic field strength on H6 channel centerline at 300 V, 10 mg/s, for 2.4 A inner magnet current and 2.14 A outer magnet current.

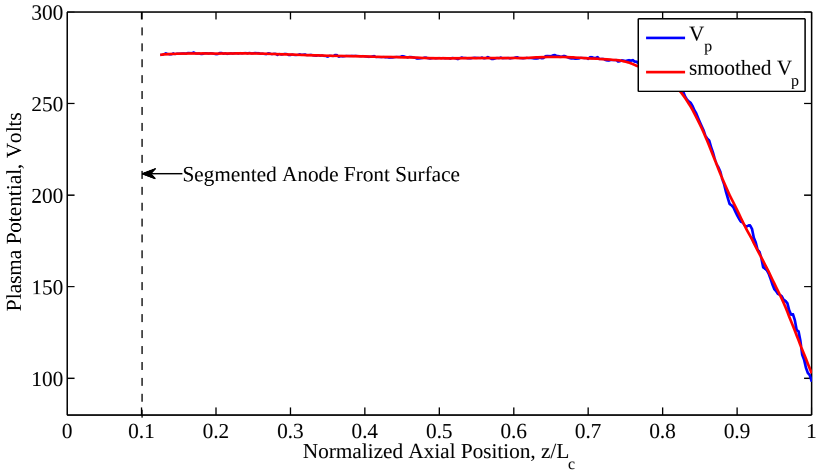

Figure 5.16. **Plasma potential on H6 channel centerline at 300 V, 10 mg/s. A smoothed plasma potential signal using a moving average filter is also shown and used in the following figures. The potential is calculated from floating emissive probe measurements corrected for electron temperature from a subsequent Langmuir probe sweep.**

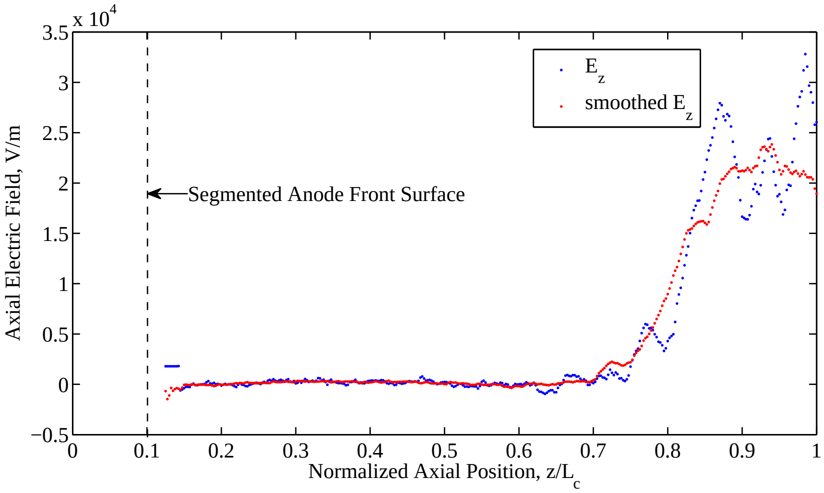

Figure 5.17. **Axial electric field strength on H6 channel centerline at 300 V, 10 mg/s. The smoothed plasma potential removes some of the noise in the signal in the flat regime near the anode. The moving average window was chosen to be large enough to smooth the signal near the anode without concern for reproducing sharp features near the exit plane.**

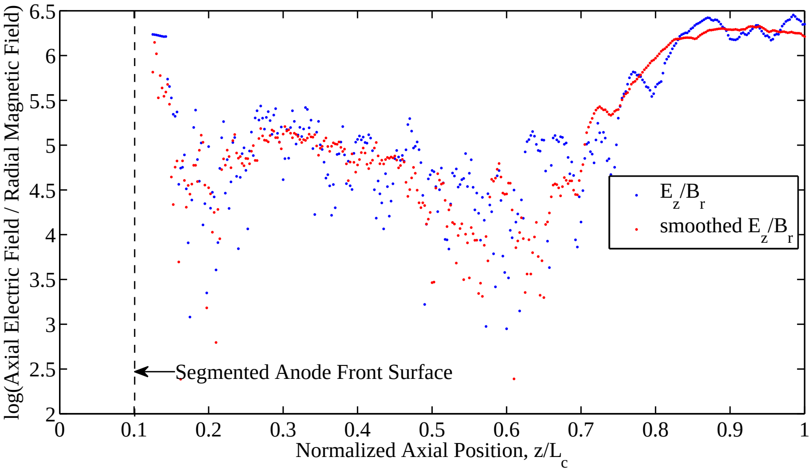

Figure 5.18. Logarithm of the ratio of axial electric field strength E_z to radial magnetic field strength B_r on H6 Channel Centerline at 300 V, 10 mg/s. Despite the low values of both fields, their ratio surprisingly falls into a relatively narrow band around 10^5. The potential error bars on this estimate are large, and any value in the range $10^{4.5}$-$10^{5.5}$ would be plausible from this figure.

Additionally, from Eqn. 5.20 the spoke perturbation density $n' = 2.5 \times 10^{16}$ cm^{-3}, for a ratio $n'/n_0 \approx 0.25$. This supports our frequent invocation of the approximation $n' \ll n_0$ in the preceding sections, though as it turns out the corrections to this approximation are small even for $n^{'}/n_0$ of order unity, and zero for $n^{'}/n_0 < 0.5$ (see next section).

Over the 12 anode segments a current density of 40 mA/cm^2 corresponds to a total spoke-induced current of 4.2 A in a discharge current of 10.9 A. Physically this means that at the anode, or in the near-anode region, a little under half of the discharge current is carried by rotating spokes! This is a staggering number, albeit with very large error bars, all the more so considering that turbulence is generally not considered to be a significant transport pathway deep in the discharge channel. The channel is generally the domain of electron-wall collisional transport in most models, and in the very near anode region even classical electron-neutral scattering alone is often sufficient to bring models into close agreement with experimental values.

Nevertheless, this experimental result is consistent with prior and contemporary experimental results, notably those of Lomas and Ellison.[5,8,20]

5.3.2.3 Sources of error

Several sources of error affect the accuracy of the calculation of cross-field electron current above. The largest is the uncertainty in the value of E_z/B_r near the segmented anode. The electric field is extremely small in this region, and the noise and uncertainty in the measurement of the plasma potential are particularly troublesome. Rather than gauge the uncertainty from the electric field and magnetic field separately, we will instead use the spread in the values of the ratio from Figure 5.18 to make an estimate of error. Since the plasma potential profile is formed self-consistently by the magnetic field in a Hall thruster, one might expect some form of proportionality between these two quantities to hold true. This does not hold across wildly different regions of the thruster plasma, for example between the near-anode region and the acceleration region, or again between the acceleration region and the near-field plume, but judging from Figure 5.18 the value of E_z/B_r does appear to hold in a band around 10^5 m/s, with substantial variation from around $10^{4.5} \approx 3\times10^4$ m/s to $10^{5.5} \approx 3 \times 10^5$ m/s. The lower extreme would correspond to a reduction of 70% of the spoke-induced cross-field current density to 12 mA/cm^2, and the upper extreme would triple it to 120 mA/cm^2. This latter case is clearly an overestimate since it would give a spoke-induced cross-field current greater than the discharge current.

Another, more easily quantifiable is the assumption in Equation 5.19 that $n^{'}/n_0 \ll 1$. If we denote the ratio of densities $n^{'}/n_0$ by ϵ then we may express 5.17 as

$$j_{ez}\left(\theta\right) \propto \left(sin\left(\theta\right) + \epsilon sin^2\left(\theta\right)\right) \tag{5.24}$$

Ignoring the term ϵ in calculating the amplitude of $j_{ez}\left(\theta\right)$ turns out not to introduce any error at all for small enough ϵ. This is because $\sin^2\left(\theta\right)$ is always positive, so for small amplitudes it shifts the peak and the trough of $\sin\left(\theta\right)$ up by the same amount. For larger amplitudes it introduces other disturbances, however. A bit of calculus shows that the amplitude of the expression is given by

$$\left(sin\left(\theta\right) + \epsilon sin^2\left(\theta\right)\right)_{amplitude} = \begin{cases} 1, & \epsilon < 1/2 \\ \frac{1}{2}\left(1 + \epsilon + \frac{1}{4\epsilon}\right), & \epsilon > 1/2 \end{cases} \tag{5.25}$$

so, for a value of $\epsilon = n'/n_0 = 0.25$ the approximation does not introduce an error.

A significant source of error is in the diagnostics of Reid. Setting aside possible differences in H6 plasma structure between the contiguous and segmented anode, both Langmuir and floating emissive probes are subject to substantial errors on their own, which Reid notes as >50% for the Langmuir probe plasma density measurements. Taking this 50% factor into account, the range of current densities extends from 20 to 80 mA/cm^2.

Taken together, the large uncertainty in the value of E_z/B_r in the anode region and the inherent uncertainty in the Langmuir probe density measurement give a potential reduction of $\bar{j_{ez}}$ to $(0.3)\,(0.5)\,40$ mA/cm^2= 6 mA/cm^2 (0.62 A total) or an increase to the full discharge current density. This corresponds to error bars on the initial estimate of 4.2 A of spoke-induced cross-field current that range from 0.62 A to 10.9 A, or 6% - 100% of the total discharge current.

In spite of the large uncertainty associated with isolating the cross-field current due to spokes, the middle of the estimated range is consistent with the much higher current density device of Lomas and the smaller, low-power device of Ellison.[8,18] It is remarkable that these spokes are still an influential electron transport mechanism in light of the substantial evolution of Hall thruster design since the 1960s when they were first detected. The large role the spoke instability plays across the widely different operating regimes and thruster geometries of these three devices indicate a robust formation mechanism in crossed field devices.

5.3.3 Other Results from the Segmented Anode

5.3.3.1 Relation between individual segment discharge currents and total discharge current

One likely reason spoke modes go so often undetected in Hall thrusters, despite their near universal presence, is their concealment in total discharge current measurements. Individual segment measurements show strong peaks at 14 and 18 kHz, which from the previous section we may confidently identify as the $m = 4$ and $m = 5$ spoke modes. However, as the current from more segments is considered in aggregate (see Figure 5.19), the relative dominance of the spoke modes in the power spectrum diminishes in comparison to the more broadly humped $m = 0$ breathing mode at 10 kHz.

The physical basis of this concealment when more segments are considered together is that the breathing mode appears weakly but in unison across all segments, while the spokes are strong but relatively out of phase from one segment to another. As the currents from more segments are added together, the contributions from the breathing mode add constructively while those from the spoke modes add destructively. The result is an aggregate signal that downplays the presence of spoke modes in the discharge by effectively integrating away the azimuthal spoke mode over the

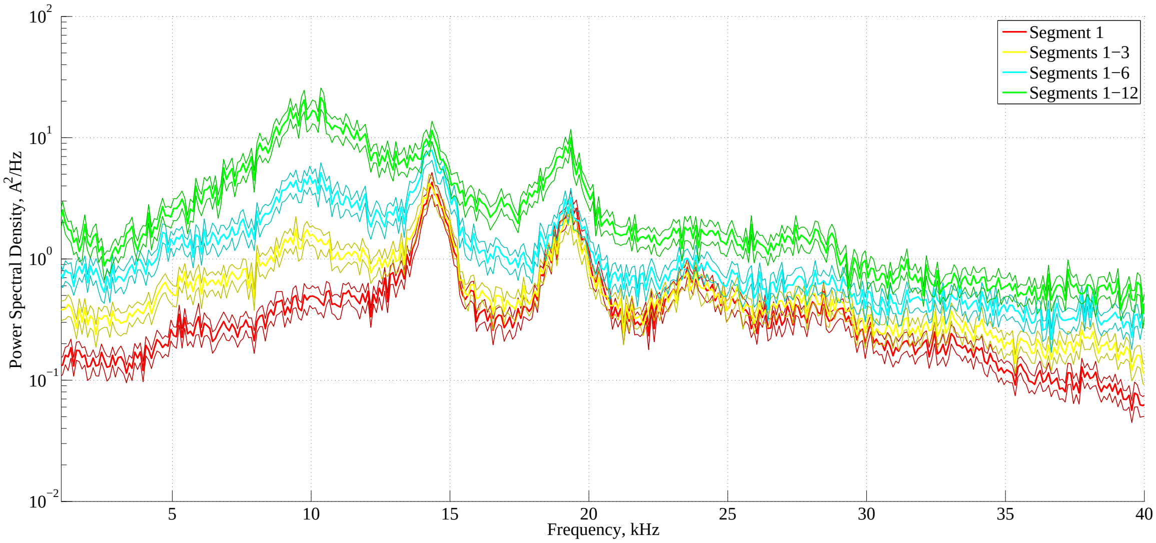

Figure 5.19. Segmented anode discharge current DFTs for individual and groups of segments. The DFT of a single segment (red) shows strong peaks corresponding to the $m = 4$ and $m = 5$ spoke modes shown in Figure 5.12, with little evidence of the $m = 0$ breathing mode at 10 kHz. However, as more segments are considered together (yellow, blue) the breathing mode grows while the spoke modes diminish in relative magnitude. Finally, when all 12 segments are combined to give the entire thruster discharge current (green) the spoke modes drop below the breathing mode. In conventional contiguous anode thrusters the spoke modes are not even visible, and it is likely that only the discrete nature of the segmented anode, chopping the electron current as it passes between segments, preserves their visibility in the total discharge current spectrum seen here.

full 2π radians of the complete set of anode segments.

The power spectrum measured from split-core Hall probes on the anode line confirm that the summation of the currents from the magnetoresistive current sensors on each segment give an accurate picture of the total discharge current oscillations.

5.3.3.2 Comparison to nominal operation without segmented anode

The segmented anode results presented in this section were during operation in a considerably different mode than normally observed during contiguous anode operation at identical discharge voltage, mass flow rate and magnet settings. Because of the quasi-pulsed operation of the H6 during this test to preserve electrical isolation of the segmented anode , it is difficult to say what portion of these differences are attributable to changes in the thruster geometry and electrode configuration versus

	Contiguous Anode	Segmented Anode
Mean Discharge Current $\bar{I_D}$	9.2 A	10.9 A
Discharge Current Oscillation Amplitude $\widetilde{I_D}$	3.8 A	0.9 A
Dominant spoke mode	$m = 2, 3$	$m = 4, 5$
Cathode keeper on?	No	Yes
Spoke frequencies visible in total I_D spectrum?	No	Yes

Table 5.3. Key feature comparison, segmented anode versus contiguous anode operation at 300 V, 10 mg/s. The segmented anode appears to seed or prime higher spoke modes than usual, and the discharge oscillations are reduced, suggesting operation with the segmented anode is actually more stable than without.

due to the outgassing from the discharge channel walls and other startup transients. The segmented anode was also fired with the cathode keeper on and drawing 1.7 A of current as a precaution in case the thruster went unstable.

Comparison of the discharge current oscillations and FASTCAM videos between segmented and contiguous anode operation show that the segmented anode shifts spoke mode oscillations to higher mode numbers (Figures 5.12 and 5.21). This may be because the discrete segments seed or prime the discharge with higher spoke modes. The $m = 2$ and $m = 3$ spoke modes are strongest in the contiguous anode configuration, though both are dwarfed by an overpowering breathing mode at 18 kHz. With the segmented anode the $m = 4$ and $m = 5$ spoke modes are dominant, and the breathing mode has been substantially reduced in both frequency and amplitude (note that the units of power spectral density are arbitrary and useful only for relative comparisons on a single figure, not across figures). Indeed, if the magnitude of the global discharge current oscillations $\widetilde{I_D}$ are taken as a measure of stability, the segmented anode is actually *more* stable than the contiguous anode (Table 5.3).

The highly elevated mean discharge current is typical for Hall thrusters before thruster bakeout is completed, as water and other gases absorbed into the boron nitride discharge channel walls during exposure to atmosphere are released and act

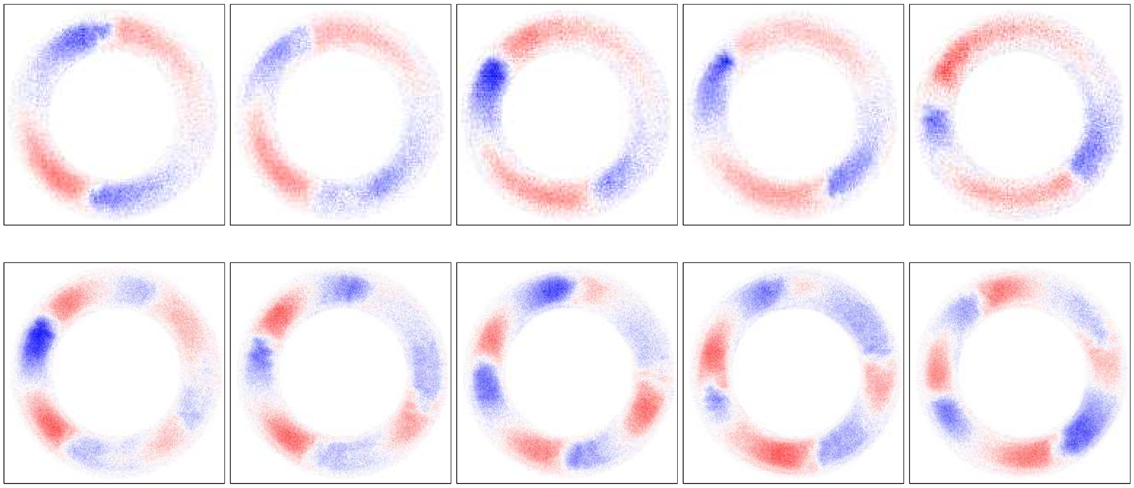

Figure 5.20. Top, postprocessed high speed images of the H6 at 300 V, 10 mg/s operation with the original contiguous anode. The $m = 2$ spoke mode is clearly visible. The video was taken at 162,750 fps, but only every fourth frame is shown to make the rotation of the spoke more apparent since the spoke velocity is much lower with the contiguous anode. Bottom, images at 87,500 fps of the H6 at the same operating condition with the segmented anode. The $m = 4$ mode is clearly visible in this case.

as an additional source of mass flow in the channel.[REF: Hargus] The value given for contiguous anode operation is for steady state after this process has been completed.

Figure 5.21 also shows that the dominant spoke mode frequencies with the contiguous anode all lie below the breathing mode frequency, which is typical of most other high speed Hall thruster videos I have acquired. The H6 with segmented anode and some cases at fairly low voltage (150 V or less) are the only Hall thruster configurations I have observed with a spoke modes at a substantially higher frequency than the breathing mode. In addition the segmented anode is the only configuration bar none where the spoke modes show up in the DFT of the total discharge current. I attribute both of these effects to the introduction of the 12 discrete boron nitride spacers that effectively chop the discharge current and seed spoke modes at higher mode numbers and frequencies than are normally stable. For example, the same basic structure of spoke frequencies is visible in both anodes in Figure 5.21, but the $m = 4$ spoke mode at 14 kHz is barely noticeable with the contiguous anode

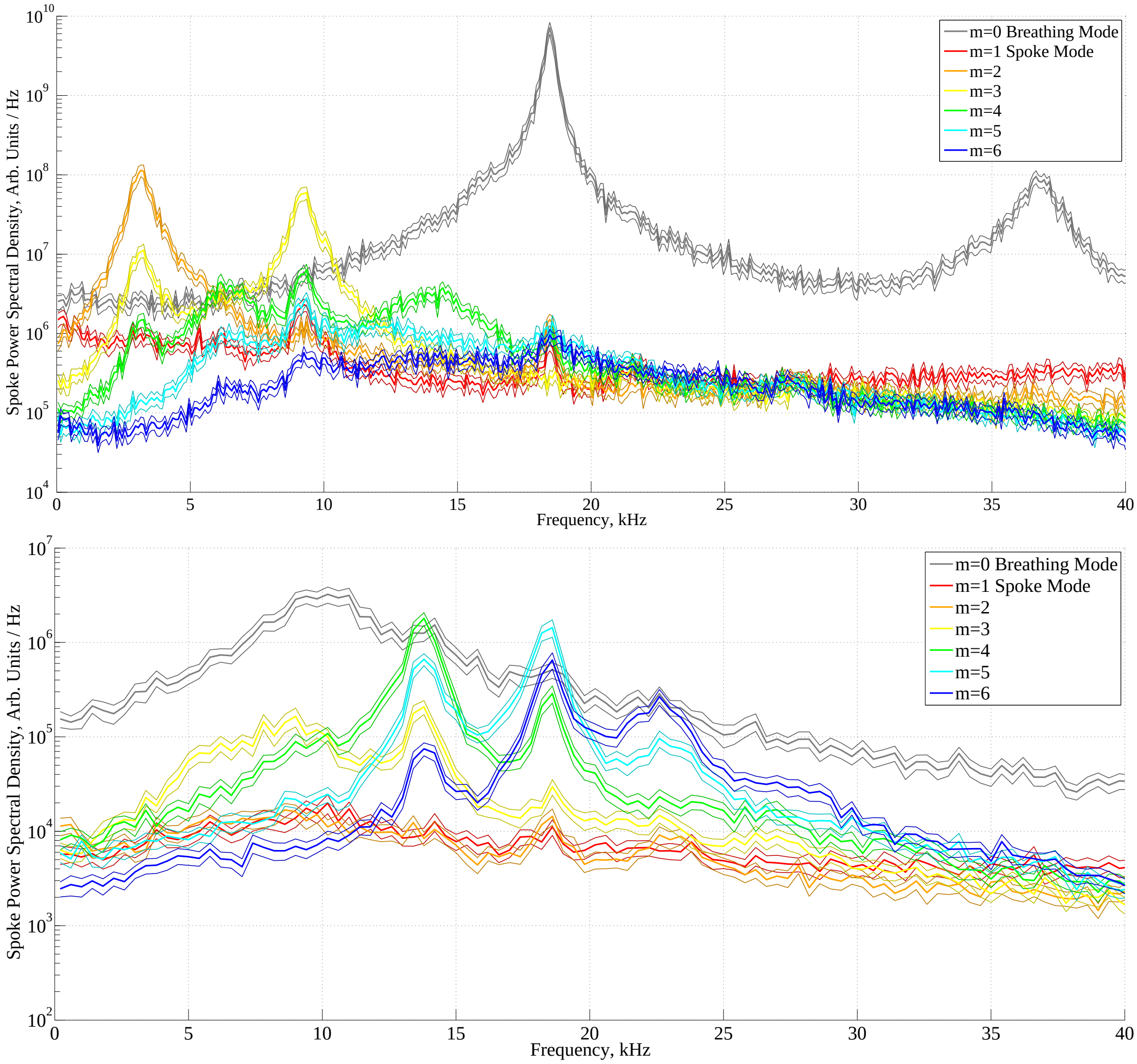

Figure 5.21. Top, 2D DFT of the spoke surface for the H6 operating at 300 V, 10 mg/s with the original contiguous anode. The most prominent spoke modes are $m = 2$ and $m = 3$, but the breathing mode is exceptionally strong at this condition and its second harmonic at 37 kHz is visible as well. Bottom, 2D DFT of the H6 at the same operating condition with the segmented anode. The $m = 4$ and $m = 5$ spoke modes are now prominent, while the breathing mode has shifted substantially lower in frequency and drastically lower in amplitude. Finally, note that the low frequencies of the spoke modes relative to the breathing mode in the top figure during contiguous anode operation are typical; the segmented anode is the only thruster configuration yet observed with dominant spoke frequencies higher than the breathing mode frequency.

while it is dominant and the $m = 2, 3$ modes are diminished with the segmented anode. Modes higher than $m = 3$ are rarely observed in the H6 across all operating conditions with the contiguous anode.

In short, while there are clear changes that the segmented anode introduces to the discharge, the primary value of this work lies less in whether the segmented anode preserves the discharge characteristics of contiguous anode and more in conclusively demonstrating that visible rotating spokes detected via high speed camera correspond to azimuthally localized electron current deposition to the anode. Given the excellent matching between FASTCAM video spoke frequencies and local current oscillation frequencies on individual segments, this point is established.

5.3.3.3 Nonuniform discharge current collection

One surprising result of the experiment was that the current to each segment is not uniform, as one might initially expect. Instead, some segments draw more than twice as much current on average as others, as for example segments 2 and 11 versus 4 and 12 in Figure 5.13. The segmented anode offers an entirely new perspective on thruster operation, so it is difficult to interpret this result – after all, it is not clear in hindsight whether the discharge current is azimuthally uniform even with a conventional anode, and this may be a normal feature of Hall thruster operation to which we are typically blind. So, while it may be premature to attribute this result to any particular design defect, as it may have already have been present previously unobserved, for completeness' sake it is worth mentioning and speculating on a few potential causes.

Some influencing factors may be: slight misalignment of the centrally mounted cathode, leading to preferential cathode coupling to some of the segments over the others; imperfections in the segmented anode mounting in the discharge channel, such that some segments sit farther forward axially and thus may “intercept” electrons that would otherwise have continued on to adjacent segments; slightly different bias voltages applied to each segment due to differences in voltage fall across the lead wires; azimuthal nonuniformity in the applied magnetic field; or possibly outgassing or other effects linked to rapid data acquisition within a few minutes of thruster ignition before full bakeout was complete.

Following up on these possibilities, the cathode orifice centerline does tend to sit slightly off thruster centerline due to imperfections in its construction and alignment, perhaps by 1-2 mm typically, but there is no simple $m = 1$ pattern visible in the current levels of Figure 5.13 as might be expected from this imperfection. It is interesting to note that if such a hypothesis were true, one would also expect substantial asymmetries with externally mounted cathodes. No evidence exists for this at present, though such asymmetries would be undetectable with a conventional contiguous anode in the discharge current measurement. It is not clear whether asymmetry in electron deposition to the anode would result in noticeable changes to gross thruster operation.

The axial position of the segments was measured to vary by approximately 1.5 mm across all segments, but this variation shows no correlation with the measured current variation. As measured at room temperature in atmosphere the line resistance of each line varies only by a few tenths of an ohm, which given the current levels on each segment should induce voltage variations only on the order of a few hundred millivolts. The eight discrete outer cores of the H6 magnetic circuit are bridged by the outer pole piece, and in the discharge channel simulations typically show negligible differences of < 1 G between points aligned with the cores versus between them.

The effects of outgassing are certainly present, as the discharge current was elevated to 10.9 amps at the time of data acquisition from the usual 9.2 amps steady state level with the contiguous anode, but it is unclear why this would give a preferential effect at one azimuthal location over any other. Ultimately, the nonuniformity of the currents to each segment is a curiosity, to be sure, but one that I consider to detract from the other results.

5.4 The Role of Rotating spokes in Low Voltage operation

For the most part this thesis deals with the mechanisms of electron transport without question of whether they bode well or ill for thruster performance. This section is an exception. Here we consider whether spokes are desirable or undesirable in a Hall thruster. The previous section showed that rotating spokes are linked to cross-field electron transport, so one might reasonably expect that thruster performance would be improved by suppressing spokes or eliminating them entirely if possible. The result would be less backstreaming electron current and a higher overall efficiency. However, recall the lesson of the "golden electron" discussed in Section 2.1: some backstreaming electron current is required to sustain the discharge, and it is difficult to say a priori what the minimum requirement is to maintain healthy thruster operation. In short, it is not so easy to categorically state whether spokes are good or bad. It may depend on both the thruster and operating condition in question. Moreover, given the omnipresence of the rotating spoke to some degree across all the H6 operating conditions noted in the parameter study, it is difficult to find a convenient operating condition for comparison between spoke and no-spoke operation.

However, Parker reported the triggering of a transition between a spoke-present mode and a spoke-absent mode in the Princeton cylindrical Hall thruster by manipulating the cathode emission current and observed the expected performance improvement with spoke suppression.[26]This transition was associated with a substantial change in discharge current, due only to the changing cathode conditions. This motivated the re-examination of a similar operating mode transition, the Brown transition reported at low voltage[17] in the H6, using the high speed camera to monitor spoke behavior during the transition. Surprisingly, exactly the opposite effect was observed – better performance was observed in the spoke-present case.

5.4.1 The Brown transition

Sharp transitions in a low-voltage operating mode in the H6 were first reported by Brown,[17,23] and have since been observed on both other copies of the H6 at the University of Michigan and Jet Propulsion Laboratory. This transition was well-characterized by Brown in the range from 100-120 V, where depending on cathode flow rate or magnetic field the discharge current of the thruster can be drastically affected in step-function fashion. These sudden shifts in discharge current are comprised largely of changes in backstreaming electron current through the plume, raising efficiency by several percent while maintaining constant thrust. Hysteresis in the thruster discharge makes it possible to operate in either mode at certain choices of cathode flow fraction or magnetic field, depending on the direction of approach. Based on consistent discharge current oscillation frequencies between modes, though with very widely different amplitudes, Brown attributed these shifts to one of several causes: rotating spoke instabilities, cathode oscillations, power supply oscillations, or the Hall thruster breathing mode. High-speed video shows that these shifts occur with the formation of a coherent rotating spoke instability.

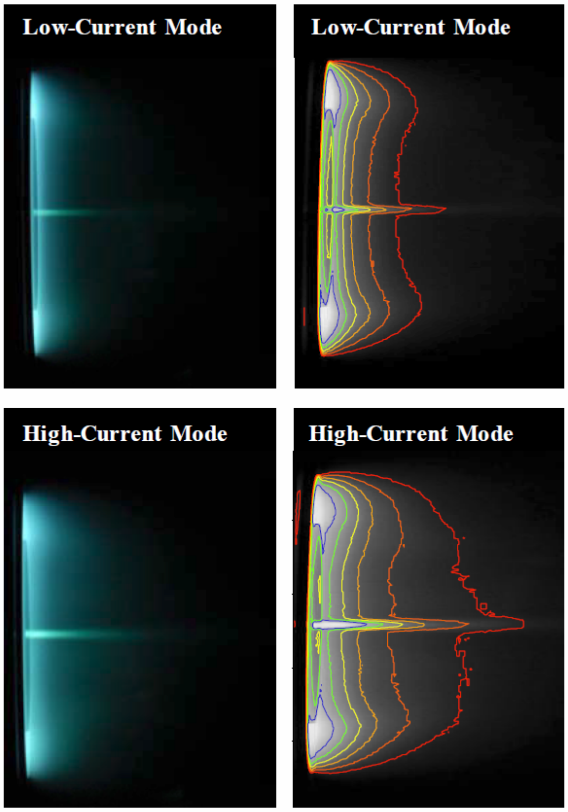

Figure 5.22. ***Figure and caption reprinted from Brown[23]:*** **Photographs of the [H6] 6-kW Hall thruster jet-mode plume structure for the low-current mode (top left) and high-current mode (bottom left) during 105-V, 20-mg/s operation. Contours of constant image intensity are shown for the low-current mode (top right) and the high-current mode (bottom right). Photos were taken with identical settings on a tripod mounted Nikon D200 DSLR using a 70- mm lens with manual focus at F/5, ISO-400, and exposure time of 1/2000 sec.**

Reproduction of a low-voltage transition similar to Brown's on the University of Michigan copy of the H6 requires a higher cathode flow fraction (CFF), about 35% CFF. This high cathode flow fraction is due to conscious choice not to use a supplemental trim coil to optimize magnetic field for low voltage as Brown did. This maintains a consistent magnetic field topology with all other operating conditions examined in this work. While this cathode flow fraction is very high, it should also be noted that Brown demonstrated the transition at 14% CFF but observed a relatively flat thruster efficiency of 33% from 14% CFF up to 26% CFF. Performance measurements were not taken during high-speed imaging, but the discharge current behavior observed clearly indicates Brown's transition.

The transition is between two modes labeled "high-current" and "low-current." The high-current mode is characterized by extremely wide oscillations in discharge current, with mean discharge current 10.6 A and peak-to-peak current oscillations on the order of 20 A. The DFT is shown at top left in Figure 5.23, where the sharp breathing mode peak at about 5 kHz and several higher harmonics are clearly visible. The low-current mode, triggered at higher cathode flow fractions, has a mean discharge current of only 9.4 A and peak-to-peak current oscillations of about 2 A. At top right in Figure 5.23, the low-current mode's breathing mode peak is at approximately the same frequency but with a power spectral density many orders of magnitude lower. This quiescent low-current mode also shows a visible change to a more focused plume structure, seen in Figure 5.22.

Variation in the spoke modes $m \geq 0$ is less evident than the drastic reduction in the dominant $m = 0$ breathing mode oscillation, but on closer examination these structures also change with the mode transition. The enlarged images at bottom in Figure 5.23 show that, while the peak power spectral density amplitude for the

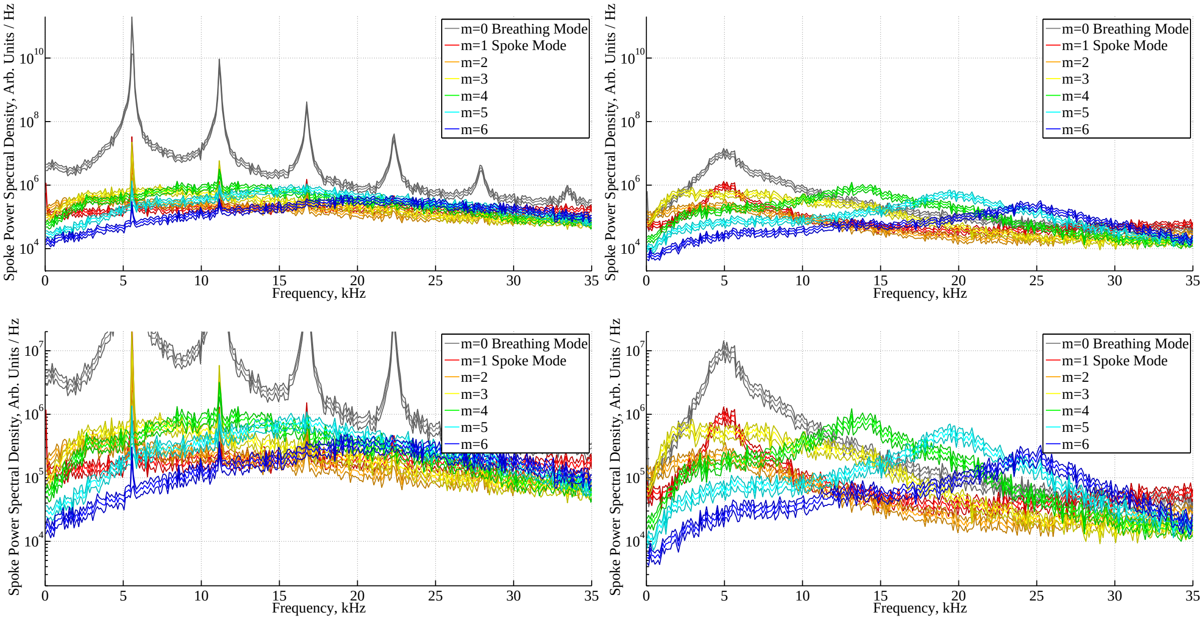

Figure 5.23. Selected 2D DFT power spectra observed in operating mode transitions at 105 V, 10 mg/s. Top left, high-current mode operation with a dominant $m = 0$ breathing mode oscillation; top right, the low-current mode showing a much more quiescent oscillation spectra. Bottom, enlarged images of both spectra show the shift in spoke mode structure from broadband frequency structures in the high-current mode to clearly peaked structures in the low-current mode, indicating the formation of more stable and coherent spokes. This transition from an exaggerated breathing mode with decoherent spokes to a quiescent discharge with more stabilized spokes corresponds to a reduction in backstreaming electron current and an improvement in thruster operating efficiency.

spoke modes does not appreciably change during the transition, the overall structure of the power spectral density does change. In particular, during the low-current mode the spoke mode frequency peaks are much more clearly defined. In the context of the 2D DFT, this means that in the low-current mode the structures are more coherent, holding together in a wave structure for longer sustained periods. In the high-current operating condition there are four-, five- and six-fold rotating structures in the discharge channel, but the wide frequency hump indicates that they are not coherent – instead, they turbulently form and reform at different points in the discharge channel, giving rise to effective discontinuous pulses of spoke behavior that are represented with this broadband frequency spread.

From this data alone it is not clear whether the change in spoke behavior causes the mode transition or is caused by it, i.e., whether the relationship is causal or merely correlated, but it does demonstrate that low-voltage operation is more efficient when more stable spokes are present. For 105 V operation Brown measured an improvement in total efficiency from 31% to 33% and in thrust to power from 79 to 86 mN/kW between the high-current and low current mode. While efficiencies in the 30% range may are not terribly impressive compared to the 60%+ efficiency at nominal operation, 105 V is on the very edge of the operating envelope of the H6. At this voltage even fixed losses like the 12 V xenon ionization potential and the 5-10 V sheath fall for ion bombardment self-heating in the cathode form relatively large efficiency penalties, and the maximization of thrust to power ratios at low voltage motivate the continued study and improvement of Hall thruster operation in this voltage range. If the rotating spoke / efficiency relationship is causal and the spoke could be triggered to improve efficiency even further, perhaps by active feedback control through a segmented anode or optimized neutral gas injection in the near-field, the payoff would have significant application in extending the Hall thruster operating envelope.

5.5 Evidence for Spoke Presence in the Near Field

5.5.1 Visual Evidence in High Speed Video

Given that rotating spokes are omnipresent across different thrusters and operating conditions and contribute significantly to cross-field electron transport in the near-anode region, it is reasonable to ask if they are a candidate electron transport mechanism outside the discharge channel as well. This possibility is certainly strongly suggested by the link between stabilized spoke structures and improved thruster efficiency due reduced backstreaming electron current in the low voltage Brown transition, discussed in Section 5.4.1 and in particular illustrated in Figure 5.23. To this end we review additional evidence that the spokes extend spatially into the near-field plume and play a role in the global electron transport picture.

High-speed imaging of the discharge channel necessarily axially integrates a signal through the entire plume from the camera's downstream viewpoint, making it difficult to gauge the axial extent of the spokes. However, this vantage point is capable in principle of resolving the radial extent of the spokes. The effort is complicated by very low visible light intensity over the inner and outer pole pieces due to the low plasma densities in this region compared with the discharge channel.

Following the visualization technique given in Section 5.1.1, we again consider a video as a 3D function for pixel intensity versus pixel row, column, and video frame i, j and k and start from the AC-coupled and normalized pixel brightness from Equation 5.5

$$p_{norm_{AC}}\left(i,j,k\right) = p_{norm}\left(i,j,k\right) - M\left(i,j\right) \tag{5.26}$$

where $p_{norm_{AC}}$ is the quantity plotted in the still frames of Figure 5.4. This normalization improved spoke visualization by removing the breathing mode oscillation signal, brightening "dim" video frames and dimming "bright" video frames such that the summed pixel intensity for each video frame is constant in the normalized video. The quantity M is a mean image composed of the average intensities of each pixel over the course of a video.

We now introduce a second normalization technique to define a new quantity, the normalized fluctuation intensity, as

$$\widetilde{p}_{norm_{AC}}\left(i,j,k\right) = \frac{p_{norm_{AC}}\left(i,j,k\right)}{p_{norm_{AC}Pk-Pk}\left(i,j\right)} \tag{5.27}$$

where the AC-coupled oscillations in each pixel are divided by the peak-to-peak oscillation amplitude on each pixel over the course of the video. While the first normalization was applied in time, to brighten dim frames and dim bright frames, this second normalization from Eqn. 5.27 is applied in space, to put the dim regions of each image over the pole pieces on an equal footing with the bright regions of each image over the discharge channel.

The result is shown in Figure 5.24 for H6 operation at 300 V and 10 mg/s with the segmented anode. The upper series of images in the figure shows the quantity $p_{norm_{AC}}$ from Eqn. 5.26, while the lower image shows $\widetilde{p}_{norm_{AC}}$ from Eqn. 5.27. Without the re-scaling relative to the local fluctuation amplitude, the regions over the inner pole are barely visible in the upper image. With re-scaling, the lower image shows a clear spoke-like structure emanating from the centrally mounted cathode and bridging across the inner pole to the discharge channel. Since the absolute amplitudes of

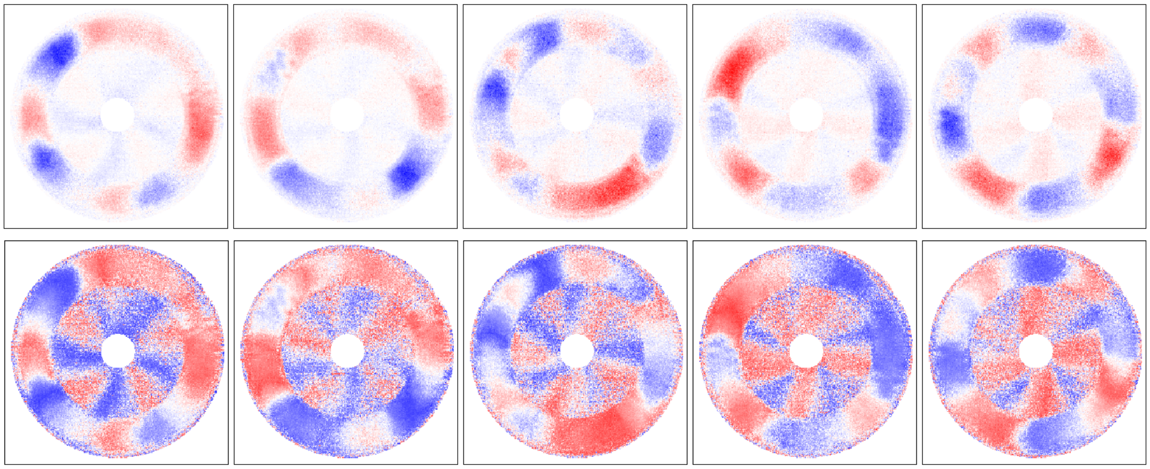

Figure 5.24. Top, a postprocessed set of still frames show the H6 operating at 300 V, 10 mg/s with the segmented anode, imaged at 87.5 kfps. Bottom, the same frames are plotted but showing the normalized fluctuation amplitude in Eqn. 5.27. This rescaling of the visible signal based on the peak-to-peak oscillation amplitude of each pixel makes the radial extent of the spoke structure visible even in the very dim regions over the inner pole, and show that the spokes can form a bridge between the cathode and the exit plane across the near field. Note that the central cathode is still cropped from both image series, since the bright cathode discharge saturates the camera sensor and oscillations are not discernible over the saturated pixel signal.

the oscillation over the pole are small, they appear to discontinuously cut off and shift azimuthally at the discharge channel inner radius. However, this appearance is consistent with a continuous structure bridging the cathode to discharge channel projected onto the plane of the image, where the faint portion of the bridge in the plume over the discharge channel could be washed out by the bright anode end of the spoke structure in the discharge channel.

Not every Hall thruster video shows this clear presence of spoke structures over the inner pole; indeed, this case is one of only a very few times they are so clearly visible. Nevertheless, the fact that such structures can be observed visually *at all*, especially given the low signal to noise ratio in this region, is highly motivating for direct investigation with electrostatic probes as spoke structure may be present in this region even in cases where it is not so clearly visible.

5.5.2 Experimental evidence in prior work

There is already some such evidence for rotating instabilities extending out into the plume in this frequency range. Smith observed helical rotating structures in the plasma potential at about 25 kHz (using a small thruster where higher frequencies are expected for km/s type velocities) extending out into the plume in the Stanford Hall thruster[3], and time-resolved Langmuir probe investigations by Lobbia several thruster diameters downstream of the BHT-600 have also shown unexplained kilohertz-level oscillations in plasma density and potential not associated with the breathing mode that may be evidence of rotating spokes.[21] Finally, while not out in the near-field plume proper, in his investigation of the transition between spoke and no-spoke conditions in the Princeton CHT, Parker detected coherent spoke oscillations near the exit plane with about 2/3 the amplitude of the oscillations observed near the anode.[26]

5.6 Discussion

From the previous sections, we have the following pieces of information: rotating spokes are omnipresent in the Hall thruster discharge, they appear even at highly efficient operating conditions, they account for a substantial level of electron current in the near-anode region, and there is very suggestive evidence from video as well as prior work using in situ probes that suggests they may extend throughout the plume, radially bridging the cathode to exit plane across the near field and extending axially downstream as well.

A theoretical framework for how spokes affect overall thruster operation and in particular how they interact with the axial Hall thruster breathing mode is likely necessary to fit all of these pieces together. This thesis does not attempt analytical modeling or theory of turbulent transport, focusing instead on creating a solid foundation of empirical observations justifying the rotating spoke instability as worthy of such attention in the future by the wider community. Nevertheless, in this section I outline a pair of physical hypotheses on the spoke / breathing mode interaction and the critical region of spoke formation based on these empirical observations, in the hope it may prove illuminating or inspiring for the future development of such models or theories. Ultimately, these are hypotheses in the full sense of the word: attempts to explain observed physical phenomena that will require further testing to be confirmed or, quite possibly, rejected. As Choueiri notes in his overview of Hall thruster oscillations, "*the detailed physics of this [rotating spoke] mode in the Hall thruster plasma remain largely unexplored*,"[15] and the thoughts below are intended as fruit for discussion and motivation for further exploration.

5.6.1 On the relation between thruster size, power level and spoke behavior

A central contradiction a suitable spoke hypothesis should resolve is the difference in early results observed with spokes, where they generally were observed more prominently at low voltage and at inefficient operating conditions, compared with the bulk of the present results that document spoke omnipresence and in fact dominance at high voltage, high efficiency operating conditions.

I suggest that the difference in results is due to the difference in power level and more fundamentally the difference in physical size between the H6 and the thrusters of previous studies. In particular, I hypothesize that in general the spoke mode is neutral or beneficial to Hall thruster operation when it can propagate at a frequency at or below the Hall thruster breathing mode frequency, while it tends to be detrimental to thruster operation in cases where it can only exist at higher frequencies.

Consider the scaling of three important quantities: the thruster channel radius, which generally scales together with thruster power; the breathing mode frequency, which is relatively constant in the 5-35 kHz range across most thruster power levels and sizes, though it tends to increase with discharge voltage; and the spoke frequency $f = v/2\pi r$, which due to the small observed variation of spoke velocity across a wide range of operating parameters mainly scales as the inverse of the thruster radius. Since the spoke travels in a narrow velocity range, and since spoke velocity rises with the spoke mode number, it stands to reason that in thrusters with a small radius even the slowest mode $m = 1$ may propagate at such high frequency that it exceeds the breathing mode frequency. The spoke clearly creates an ionization and excitation front as it travels around the channel, hence the visible emission detected on the high speed camera, and if this ionization front travels azimuthally faster than the neutral replenishment rate, there is the potential for one mode to starve the other of neutrals, though how to decide which mode survives and which is starved is not clear.

As an example of one extreme, a dominant breathing mode with practically no spoke mode takes place in the H6 at the 105 V high-current mode operating condition where the Brown transition is observed. The spoke modes that appear most prominently in the DFT all have frequencies greater than the 5 kHz breathing mode frequency, and the breathing mode completely takes over the discharge, oscillating with enormous amplitude. When the higher frequency spokes are stabilized by a large cathode flow fraction (by an admittedly unclear mechanism), thruster efficiency improves and the breathing mode is tempered significantly from a 20 A oscillation to only about 2 A. This high-current condition is the closest to a no-spokes condition

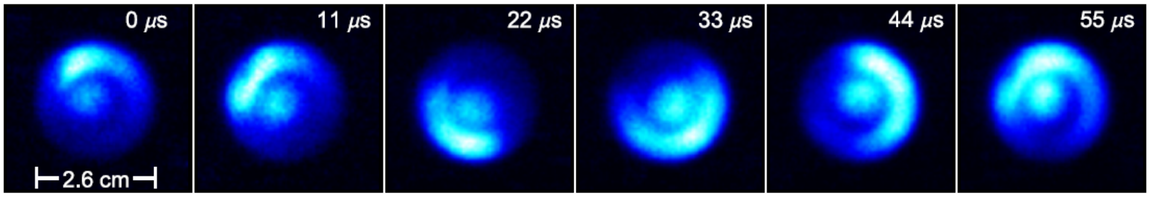

Figure 5.25. A sequence of still images showing the $m = 1$ spoke in the Princeton CHT. The spoke is of a qualitatively different character than the one in the H6, existing by itself without any superimposed $m = 0$ breathing mode. Figure from Ref.[26].

observed in the H6, and the very large breathing mode is reminiscent of SPT-100 operation. At the other extreme, the highest voltage conditions with optimized magnetic field in the parameter study where the spoke modes grew very strong and existed well under the breathing mode are the highest performance conditions in terms of overall efficiency observed in the H6.

Some support for this hypothesis lies in the difference between the Brown transition and the transition observed by Parker in the Princeton CHT. Parker's transition is of a decidedly different character from Brown's and indeed from the rest of the spectral data on the spoke and breathing modes in the H6 presented in this chapter. When the $m = 1$ spoke appears in the CHT, it is at the expense of the rest of the discharge – the spoke constitutes the entire visible plasma in the high-speed image sequences, to the detriment of the rest of the channel (Figure 5.25). In contrast, different modes in the H6 may trade dominance but the spoke and breathing modes coexist (hence the need to normalize away the breathing mode to visualize the spokes in Figure 5.2), and the case of the Brown transition is no exception. The frequencies of the modes in the CHT support the hypothesis; the spoke frequency is in the 15-35 kHz range while the breathing mode is cited as only about 10 kHz.

5.6.2 The cathode region as a potential source of the rotating spoke instability

To date most investigations of the rotating spoke have focused on the near-anode region, especially recently through the use of the segmented anode by myself and Ellison.[2,11,20] However, while the spoke is present and easily detectable in this region, several factors suggest that it may originate or be critically dependent upon conditions at the cathode. First, the changes in Hall thruster operation associated with the Brown transition at low voltage are associated with conditions near the cathode induced by increased neutral density flowing either directly through the cathode as an increased cathode flow fraction or indirectly through auxiliary flow injected around the cathode.[23] For that matter, the Parker transition is also associated with changes in cathode conditions, albeit to opposite effect. Second, the images in Figure 5.24 visibly show spokes emanating from (or admittedly perhaps extending into) the cathode. This shows that at least at some operating conditions that spokes exist in this region, though it is not conclusive that they are always present or sourced from here.

The third and perhaps most compelling piece of evidence linking spoke formation to the cathode or near-cathode region is an early work in a Hall accelerator by Allario that isolated the formation of a rotating spoke instability to the behavior of magnetic field in a critical region near a tungsten filament cathode.[13] Allario's thruster used a circular tungsten filament extending aximuthally all the way around the annular discharge channel as a cathode. By balancing the applied radial magnetic field with the self-field created by the heating current in the tungsten filament, Allario located a critical region close to the cathode where the cancellation of the two magnetic fields triggered the suppression of the spoke instability, which otherwise formed in the usual $E \times B$ direction with the highest plasma density near the cathode. This work also postulated a link with earlier work by Simon relating the criteria for spoke formation to the applied electric field and axial density gradient.[9]

The geometry of a modern Hall thruster is quite different from the arrangement of Allario, since for a centrally mounted cathode the cathode current is ejected axially along the magnetic field, and the magnetic field has in general both radial and axial components and is only purely radial in a narrow region of the discharge channel near the exit plane. As a result the cathode self-field and the applied field do not cancel, and instead are for the most part mutually orthogonal in the cathode region. Nevertheless, the behavior is similar to observations by Brown that, in addition to cathode flow variation, magnetic field variation can also trigger mode transitions. While transitions triggered by magnetic field variation were not explicitly studied for spoke behavior with the high-speed camera, the work of Brown shows them to be similar in every respect to transitions triggered by cathode flow variation, and it seems plausible to assume that they are also correlated with the forced stabilization of spoke modes.

Taken together these different pieces suggest that the cathode may be the source region of the spoke instability, but they are not yet conclusive. Again, I express the hope that the extensive present characterization of the importance of this instability will motivate its deeper investigation, to reveal its underlying physics and, perhaps, ultimately allow its manipulation for the improvement of Hall thruster stability and performance and its incorporation into thruster models.

[1] Yoshikawa, S. and Rose, D. J., "Anomalous Diffusion of a Plasma across a Magnetic Field," *Physics of Fluids*, Vol. 5, 1962, pp. 334.

[2] McDonald, M. and Gallimore, A., "Parametric Investigation of the Rotating Spoke Instability in Hall Thrusters," *32nd International Electric Propulsion Conference*, IEPC 2011-242, Wiesbaden, Germany, 2011.

[3] Smith, A. W. and Cappelli, M. A., "Time and space-correlated plasma potential measurements in the near field of a coaxial Hall plasma discharge," *Physics of Plasmas*, Vol. 16, No. 7, 2009, pp. 073504–11.

[4] Reid, B. M. and Gallimore, A. D., "Langmuir Probe Measurements in the Discharge Channel of a 6-kW Hall Thruster," *44th AIAA/ASME/SAE/ASEE Joint Propulsion Conference & Exhibit*, AIAA 2008-4920, 2008.

[5] Janes, G. S. and Lowder, R. S., "Anomalous Electron Diffusion and Ion Acceleration in a Low-Density Plasma," *Physics of Fluids*, Vol. 9, 1966, pp. 1115.

[6] McDonald, M. S. and Gallimore, A. D., "Rotating Spoke Instabilities in Hall Thrusters," *IEEE Transactions on Plasma Science (to be published)*, 2011.

[7] Liang, R. and Gallimore, A., "Far-Field Plume Measurements of a Nested-Channel Hall-Effect Thruster," *49th AIAA Aerospace Sciences Meeting*, AIAA-2011-1016, Jan. 2011.

[8] Lomas, P. J. and Kilkenny, J. D., "Electrothermal instabilities in a Hall accelerator," *Plasma Physics*, Vol. 19, No. 4, 1977, pp. 329–341.

[9] Simon, A., "Instability of a Partially Ionized Plasma in Crossed Electric and Magnetic Fields," *Physics of Fluids*, Vol. 6, No. 3, 1963, pp. 382.

[10] Reid, B. M. and Gallimore, A. D., "Plasma Potential Measurements in the Discharge Channel of a 6-kW Hall Thruster," *44th AIAA/ASME/SAE/ASEE Joint Propulsion Conference & Exhibit*, AIAA 2008-5185, 2008.

[11] McDonald, M. S. and Gallimore, A. D., "Measurement of Cross-Field Electron Current in a Hall Thruster Due to Rotating Spoke Instabilities," *47th AIAA/ASME/SAE/ASEE Joint Propulsion Conference & Exhibit*, AIAA 2011-5810, 2011.

[12] Hofer, R. R., *Development and Characterization of High-Efficiency, High-Specific Impulse Xenon Hall Thrusters*, Ph.D. thesis, University of Michigan, 2004.

[13] Allario, F., Hess, R. V., and Sidney, B. D., "Onset of rotating disturbance in linear Hall-current accelerator," *AIAA Journal*, Vol. 8, No. 6, June 1970, pp. 1117–1120.

[14] Chernov, N., *Circular and Linear Regression: Fitting Circles and Lines by Least Squares*, CRC Press, Taylor & Francis Group, Boca Raton, FL, 1st ed., 2011.

[15] Choueiri, E. Y., "Plasma oscillations in Hall thrusters," *Physics of Plasmas*, Vol. 8, No. 4, 2001, pp. 1411.

[16] Haas, J. and Gallimore, A., "Considerations on the role of the Hall current in a laboratory-model thruster," *Plasma Science, IEEE Transactions on*, Vol. 30, No. 2, 2002, pp. 687–697.

[17] Brown, D. and Gallimore, A., "Investigation of Low Discharge Voltage Hall Thruster Operating Modes and Ionization Processes," *31st International Electric Propulsion Conference*, IEPC 2009-074, Ann Arbor, MI, 2009.

[18] Ellison, C. L., Raitses, Y., and Fisch, N. J., "Cross-field electron transport induced by a rotating spoke in a cylindrical Hall thruster," *Physics of Plasmas*, Vol. 19, No. 1, Jan. 2012, pp. 013503–013503–7.

[19] Hofer, R. R., "Private Communication," Aug. 2011, Private communication.

[20] Ellison, L., Raitses, Y., and Fisch, N. J., "Cross-field Current through a Rotating Spoke," *53rd Annual Meeting of the American Physical Society Division of Plasma Physics*, Poster Presentation, 2010.

[21] Lobbia, R. B., *A Time-Resolved Investigation of the Hall Thruster Breathing Mode*, Ph.D. thesis, University of Michigan, Ann Arbor, MI, 2010.

[22] Meezan, N. B., Hargus Jr, W. A., and Cappelli, M. A., "Anomalous electron mobility in a coaxial Hall discharge plasma," *Physical Review E*, Vol. 63, No. 2, 2001, pp. 26410.

[23] Brown, D., *Investigation of Low Discharge Voltage Hall Thruster Characteristics and Evaluation of Loss Mechanisms*, Ph.D. thesis, University of Michigan, Ann Arbor, MI, 2009.

[24] Kasa, I., "A circle fitting procedure and its error analysis," *IEEE Transactions on Instrumentation and Measurement*, Vol. 25, No. 1, 1976, pp. 8–14.

[25] Reid, B., *The Influence of Neutral Flow Rate in the Operation of Hall Thrusters*, Ph.D. thesis, University of Michigan, Ann Arbor, MI, 2009.

[26] Parker, J. B., Raitses, Y., and Fisch, N. J., "Transition in electron transport in a cylindrical Hall thruster," *Applied Physics Letters*, Vol. 97, No. 9, 2010, pp. 091501.

CHAPTER VI

Conclusions

> *"The dimmed outlines of phenomenal things all merge into one another unless we put on the focussing glass of theory and screw it up sometimes to one pitch of definition, and sometimes to another, so as to see down into different depths through the great millstone of the world."*
>
> James Clerk Maxwell

6.1 Summary

This thesis set out to examine two types of anomalous electron transport mechanisms in the Hall thruster near-field on a the highly efficient H6 6-kW class Hall thruster. Presently the verdict from electron trajectory modeling is that in static (time-averaged) electromagnetic fields, collisional transport mechanisms including thruster surface collisions and binary plume collisions do not seem to have much effect in this region. This differs from previous results using this modeling technique and may be due to differences in thrusters or simulation domain size, among other factors, but the result is borne out experimentally by the lack of sensitivity of hte thruster discharge to gross changes in the potential applied to the thruster pole pieces. More complete experimental maps of plasma conditions in the plume may reveal further transport due to collisions with ions, which are not explicitly considered in the MCHall modeling code, but a sensitivity study artificially inflating the collision frequency in the plume in an attempt to conservatively account for potential electron-ion collisions also did not significantly change the simulation results.

All modeling results were for time-averaged fields, which is emphatically not a complete picture of a Hall thruster's plume. The devices are rich in oscillatory structure, both the well-known breathing mode and associated plasma fluctuations and also the rotating spokes that were explored through much of this thesis. The model results may be significantly different in the presence of field fluctuations able to impart sufficient energy to electrons to penetrate the steep sheath over the thruster surfaces, or to transiently raise electron temperatures sufficiently to alter collision cross-sections and alter the number and type of reactions taking place.

Turbulent transport in the form of rotating spoke instabilities at present appears to be the more promising avenue for investigation of anomalous transport mechanisms. While experimental quantification of the cross-field current due to this mechanism using a segmented anode was limited to the discharge channel and subject to large uncertainties, an estimated 40% of the discharge current was estimated to pass through the rotating spoke structure at a 300 V, 10 mg/s operating point. Rotating spokes were also shown to be omnipresent with varying amplitude and stability in every operating condition examined in the H6. Further investigation with other thrusters has detected rotating spokes in every additional Hall thruster that has been imaged, ranging over an order of magnitude in power from the BHT-600 600 W thruster to the X2 9-kW class nested Hall thruster.

Finally, step changes in Hall thruster operation at low voltage associated with the formation of a coherent rotating spoke structure suggest a link between the rotating spoke structure and the global electron transport picture. This link is supported by images showing a spoke structure linking the cathode to the discharge channel, a visual clue that the rotating spoke instability may bridge the near-field gap and motivating future work.

6.2 Future Work

Based on these results, I recommend that future investigation into electron transport in Hall thrusters focus on the following, in order of priority:

1. **Obtain high spatial resolution 2D, time-resolved, synchronous maps of V_p and n_e in the H6 plume**. This is the highest priority for continued analysis of both collisional and turbulent transport. On the collisional side, the low axial resolution of the present plume maps used in MCHall is a serious limitation, especially in the cathode region, and as mentioned in the previous section time-resolved maps would enable inclusion of any coupling of fields created by turbulence into the collisional transport model as well. For turbulent transport, such a map would enable calculation of the spatial extent of the spokes and the magnitude of their contribution to the cross-field current throughout the plume. Such a measurement would require a high-speed motion stage to interrogate the very near-field without probe ablation. For the best frequency response a unswept probe array consisting of an emissive probe to measure V_p (or pair of emissive probes, to calculate E_θ with reduced error) and a measurement of plasma density using either a single Langmuir probe in ion saturation or an unswept triple or quadruple Langmuir probe. A swept Langmuir probe at sufficiently high frequency might be able to provide all of these quantities from a single diagnostic, but the challenges of sweeping a probe at

such frequencies are significant.

2. **Investigate the rotating spoke instability analytically.** The literature on anomalous transport in Hall thrusters is well-stocked with theoretical papers describing transport according to various plasma waves, but to this point it has been pragmatic to wait for experimental proof that the rotating spoke was important to electron transport before investing time in describing its underlying physics. In the wake of the segmented anode results, the importance of this phenomenon is now clear and a better idea of the driving physical parameters behind spoke amplitude, speed and ultimately electron transport effects would be relevant and most welcome. Such an analytical description is also required if this mode is to be included in new Hall thruster models.

6.3 Final Thoughts

A few years ago, it would have been difficult to find many recent papers examining the rotating spoke instability either theoretically or experimentally. In that respect this investigation appears timely, as it coincided with similar high-speed imaging by Parker and Ellison on the Cylindrical Hall Thruster at Princeton, the discovery of a helical rotating plasma potential wave in the Stanford Hall Thruster by Smith at spoke-like frequencies, and most recently has even seen a renewed attention theoretically by Escobar.[1–4]

This work has for the most part eschewed theoretical investigation of the spoke mode, focusing instead on characterizing it across a wide range of operating conditions and in many thrusters to assert its omnipresence. The hope was that, if the phenomenon were indeed general, it would attract its own attention and produce far more rapid results from the wider community than any one individual could achieve.

In retrospect, it appears this hope has some modest prospect for success. It is an exciting time to be working on Hall thrusters – more power is becoming available in space, high-power thruster designs like the nested Hall thruster are coming into vogue, and there is even talk of "immortal" Hall thrusters in hushed tones. If rotating spokes turn out to be significant across the plume, as it appears they are from the evidence accumulated so far, perhaps even the electron transport problem will begin to seem more tractable. In any case the next few years look promising for new discoveries in this field, and with it for the missions that Hall thrusters may one day enable.

[1] Smith, A. W. and Cappelli, M. A., "Time and space-correlated plasma potential measurements in the near field of a coaxial Hall plasma discharge," *Physics of Plasmas*, Vol. 16, No. 7, 2009, pp. 073504–11.

[2] Ellison, C. L., Raitses, Y., and Fisch, N. J., "Cross-field electron transport induced by a rotating spoke in a cylindrical Hall thruster," *Physics of Plasmas*, Vol. 19, No. 1, Jan. 2012, pp. 013503–013503–7.

[3] Parker, J. B., Raitses, Y., and Fisch, N. J., "Transition in electron transport in a cylindrical Hall thruster," *Applied Physics Letters*, Vol. 97, No. 9, 2010, pp. 091501.

[4] Escobar, D. and Ahedo, E., "Ionization-induced azimuthal oscillation in Hall Effect Thrusters," *32nd International Electric Propulsion Conference*, IEPC 2011-196, Wiesbaden, Germany, 2011.

APPENDICES

APPENDIX A

The Application of Yoshikawa's Theory of Turbulent Field Fluctuations

In 1962 S. Yoshikawa and D. J. Rose published a paper in Physics of Fluids entitled "Anomalous Diffusion of a Plasma across a Magnetic Field".[?] The paper described first a theoretical expression for the anomalous diffusion coefficient α_B in Bohm's expression for Bohm mobility,

$$D_B \equiv \alpha_B \frac{k_B T}{eB}$$

then compared the result with an experiment with reasonably good agreement. In 1966, G. S. Janes and R. S. Lowder at the Avco Everett Research Laboratory applied Yoshikawa's theory to the problem of anomalous electron mobility in a Hall thruster in order to calculate the plasma potential and density fluctuations associated with a rotating spoke instability observed in the thruster discharge channel.[?] These theoretical calculations agreed well with experimental measurements using Langmuir probes and floating emissive probes azimuthally spaced in the discharge channel. Much later, in 2001 Meezan, Hargus and Cappelli compared the predicted cross-field electron diffusion coefficient from Yoshikawa's theory to values observed in the Stanford Hall thruster and also found excellent agreement.[?]

A.1 Derivation

Yoshikawa's theory begins from several assumptions:

1. A Cartesian geometry is assumed with an axial magnetic field $\mathbf{B} = B\hat{\mathbf{z}}$
2. The electrons are isothermal ($\nabla T_e = 0$)
3. Ions are immobile
4. Under perturbation, magnetic field fluctuations will be neglected, on the basis of a low ratio β of the kinetic pressure $p_k = nk_BT$ to the magnetic pressure $p_B = B^2/2\mu_0$ in the plasma

For reference, Yoshikawa notes that the derivation proceeds along similar lines to Herring's derivation of the magnetoresistance in solids[?] , and more generally owes to the theory of homogeneous turbulence explained by Batchelor.[?] Given the above assumptions, Yoshikawa uses the MHD electron momentum equation to examine the forces on the electrons. The MHD equations apply over long length scales compared to the Debye length and Larmor radius, and over long times compared to cyclotron period. They assume Maxwellian particle distributions, so the plasma must be strongly collisional. Finally they assume a small resistivity so that the time scale of interest must be much less than the magnetic diffusion time.

The electron momentum equation is

$$k_BT_e\nabla n + enE + e\left(\Gamma_e \times B\right) = -m_e\nu_c\Gamma_e \tag{A.1}$$

where Γ_e is the electron flux density, ν_c is the collision frequency and the other symbols have their usual meaning. The electron inertia term in the momentum equation has been neglected because the electron drift velocity is less than the thermal velocity. This corresponds to a statement that

$$T_e \gg \frac{m_e v_{E\times B}^2}{3e}$$

where T_e is in eV. This statement is true in a Hall thruster. Typical conditions in the acceleration zone are $E \sim 10^4$ V/m and $B \sim 0.01$ T, giving an $E \times B$ velocity corresponding to about 2 eV. The measured temperatures in this region are often 30-40 eV. Farther out in the plume typical values are $E \sim 10^2$ V/m and $B \sim 10^{-3}$ T, corresponding to a drift temperature of about 0.02 eV. Temperatures in this region are generally around 3-5 eV.

Assuming some form of perturbation to these quantities

$$\begin{aligned} E &\rightarrow E_0 + E' \\ \Gamma &\rightarrow \Gamma_0 + \Gamma' \\ n &\rightarrow n_0 + n' \\ \nu &\rightarrow \nu_0 + \nu' \end{aligned}$$

then Eqn. A.1 can be perturbed to find the linear response of the plasma. In the unperturbed condition, the equation is satisfied by

$$k_B T_e \nabla n_0 + e n_0 E_0 + e\left(\Gamma_0 \times B\right) = -m_e \nu_0 \Gamma_0 \tag{A.2}$$

After the perturbation, the new perturbed state must also satisfy the equation:

$$k_B T_e \nabla\left(n_0 + n'\right) + e\left(n_0 + n'\right)\left(E_0 + E'\right) + e\left(\left(\Gamma_0 + \Gamma'\right) \times B\right) = -m_e\left(\nu_0 + \nu'\right)\left(\Gamma_0 + \Gamma'\right) \tag{A.3}$$

Subtracting Eqn. A.2 from Eqn. A.3 and ignoring terms second order in the perturbed quantities yields:

$$k_B T_e \nabla n' + en_0 \mathbf{E}' + en' \mathbf{E}_0 + e\left(\mathbf{\Gamma}' \times \mathbf{B}\right) = -m_e \nu_0 \mathbf{\Gamma}' - m_e \nu' \mathbf{\Gamma}_0 \tag{A.4}$$

Since the collision frequency is defined as $\nu \equiv n\sigma v$, the perturbed collision frequency can be expressed in terms of the density perturbation as $\nu' = \nu_0 \left(n'/n_0\right)$. Yoshikawa also chooses to define an effective electric field ε as

$$\varepsilon \equiv \mathbf{E}_0 + \frac{k_B T_e}{e} \frac{\nabla n'}{n'}$$

to express Eqn. A.4 in a slightly simplified form as

$$en'\varepsilon + en_0 \mathbf{E}' + e\left(\mathbf{\Gamma}' \times \mathbf{B}\right) = -m_e \nu_0 \mathbf{\Gamma}' - m_e \nu_0 \frac{n'}{n_0} \mathbf{\Gamma}_0 \tag{A.5}$$

Typically this technique of linearization is used with momentum and energy equations to find dispersion relations for wave propagation. In this situation the standard procedure is to assume a wave form for the perturbation

$$x' = x' \exp\left(i\left(\mathbf{k} \cdot \mathbf{r} - \omega t\right)\right)$$

Given the time and space derivatives in the momentum and energy equations, the imaginary terms cancel out or multiply to -1 and a purely real disperion relation falls out. However, Yoshikawa's derivation of the Bohm diffusion constant and of the cross-field electron flux proceeds with only the momentum equation. This would normally be expected to produce an unaccompanied imaginary factor i in the equation due to the gradient operator in the kinetic pressure term, but it does not. Yoshikawa initially defines the density perturbation as $n = n_0 + n' = n_0\left(1 + s_x x\right)$, which seems to be an approximation to the perturbation near $x = 0$. He then expresses the effective electric field ε as

$$\varepsilon \equiv \mathbf{E}_0 + \frac{k_B T_e}{e}\mathbf{s}$$

Once this form is derived, the later calculations use a perturbation form

$$\begin{aligned} \mathbf{E}' &= \textstyle\sum_k \mathbf{E}_k \exp\left(i\mathbf{k}\cdot\mathbf{r}\right) \\ \mathbf{\Gamma}' &= \textstyle\sum_k \mathbf{\Gamma}_k \exp\left(i\mathbf{k}\cdot\mathbf{r}\right) \\ n' &= \textstyle\sum_k n_k \exp\left(i\mathbf{k}\cdot\mathbf{r}\right) \end{aligned} \tag{A.6}$$

The exact form for the effective electric field does not appear to play a role in the subsequent derivation, and at the end the effective electric field is expressed back in terms of the gradient of a density again (Eqn. [33] in Yoshikawa's paper), so it is unclear what role the initial linear density perturbation plays.

Once the expressions for the perturbations in Eqn. A.6 are established, the basic procedure is to solve the individual equations for each value k in the Fourier decomposition, as well as the $k = 0$ term, and to break the vector equations into their component parts along x, y and z. These equations are algebraically quite involved and so are not repeated here. Assuming isotropic turbulence, i.e., the amplitude of each Fourier component for the density is a function only of its wavelength $n_k = f\left(|k|\right)$, and assuming a large Hall parameter ω_{ce}/ν, the cross-field flux is shown to be (Yoshikawa Eqn. [31]):

$$\Gamma_{ez} = -\frac{\pi}{4}\frac{\varepsilon}{B}\frac{n'^2}{n_0} \tag{A.7}$$

and the anomalous Bohm diffusion coefficient α_B is given by

$$\alpha_B = \frac{\pi}{4} \frac{\left\langle (n - n_0)^2 \right\rangle_{avg}}{n_0^2} \tag{A.8}$$

or, in the case of a sinusoidal perturbation $n = n_0 + n' \sin(\theta)$,

$$\alpha_B = \frac{\pi}{8} \left(\frac{n'}{n_0} \right)^2$$

This form for the Bohm diffusion constant does not by itself solve the electron transport problem, since it gives no way to predict the value of the density perturbation. It is a phenomenological form that says that, if one knows the ratio of the density perturbation amplitude to the unperturbed density, one can calculate α_B or Γ_{ez}. A number of assumptions go into this derivation and the treatment of the density perturbation is mathematically ambiguous; nevertheless, the accuracy of the predictions of this formula have been verified in Hall thrusters in separate experiments.

A.2 Experimental Verification

A.2.1 Janes and Lowder

The first experimental check on Eqns. A.7 and A.8 was performed by Janes and Lowder in 1966.[?] Janes used a pair of azimuthally spaced floating emissive probes to measure azimuthal electric field and a Langmuir probe in ion saturation to measure plasma density. All probes were mounted inside the discharge channel of the thruster, and the probe spacing was varied to confirm the correlation between observed electric field and density fluctuations (Figure A.1).

Given Eqn. A.7, Janes derived an expression for the azimuthal field fluctuation amplitude E'_θ in terms of the density fluctuation n' and the applied field E_z using the following equations (Eqn. [3] and [6] in their paper):

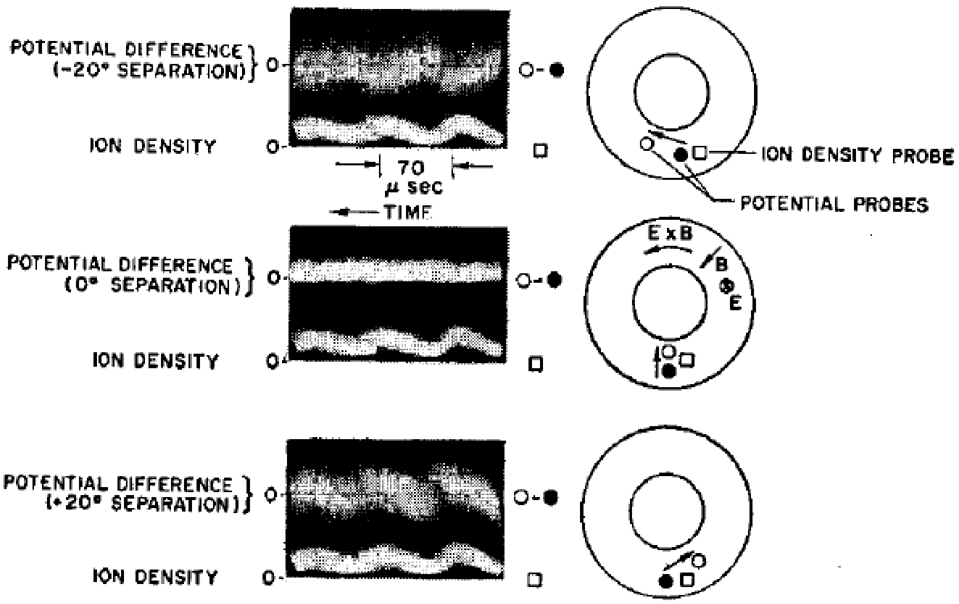

FIG. 6. Measurements illustrating correlation between the fluctuating azimuthal electric fields and the density fluctuations. The azimuthal electric field is determined from the difference signal between two heated potential probes arranged with azimuthal separation as shown in the sketches. The density measurements were obtained with a negatively biased Langmuir probe located as shown in the sketches.

Figure A.1. Figure and caption from Janes and Lowder.[?]

$$j_{e\theta} = en_0 \frac{E_z}{B_r} \tag{A.9}$$

$$\frac{1}{(\omega_{ce}\tau_e)_{eff}} \equiv \frac{\bar{j}_{ez}}{\bar{j}_{e\theta}} = \frac{1}{2}\frac{n' E'_\theta}{n_0 E_z} \tag{A.10}$$

With these expressions Janes solved for E'_θ as

$$\begin{aligned}
q\Gamma_{ez} &= j_{ez} \\
-\frac{q\pi}{4}\frac{\varepsilon}{B}\frac{n'^2}{n_0} &= \frac{j_{ez}}{j_{e\theta}} j_{e\theta} \\
-\frac{q\pi}{4}\frac{\varepsilon}{B}\frac{n'^2}{n_0} &= \left(\frac{1}{2}\frac{n' E'_\theta}{n_0 E_z}\right)\left(en_0\frac{E_z}{B_r}\right) \\
-\frac{\pi}{4}\varepsilon n' &= n_0 E'_\theta
\end{aligned}$$

At this point, ε is still the effective electric field strength from Yoshikawa's derivation, including a piece due to the electron pressure gradient. Nevertheless, Janes considers $\varepsilon = E_z$, and as we shall see, obtains good results. The negative sign is immaterial since we are solving for the amplitude of the fluctuation. Janes' final expression is (Eqn. [7] in that paper)

$$E'_\theta = \frac{\pi}{4}\frac{n'}{n_0}E_z \tag{A.11}$$

Using the measured values of $n'/n_0 = 0.5$ measured with the Langmuir probe in ion saturation and using the known applied axial field strength in the thruster (also from floating emissive probes) of 17 V/cm yields a predicted azimuthal field of 6.6 V/cm in Janes' and Lowder's thruster. The measured peak azimuthal field E'_θ was 6 V/cm, for an error of 10%.

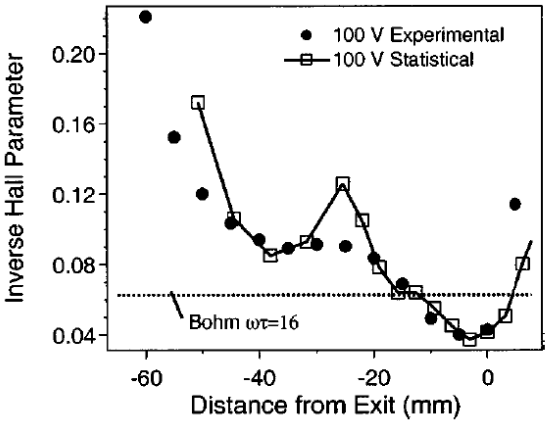

FIG. 13. Comparison of statistical fluctuation analysis to experimental inverse Hall parameter profile at 100 V operation.

Figure A.2. Figure and caption from Meezan *et. al.*? The values predicted by Yoshikawa's theory are the "statistical" data set.

A.2.2 Meezan, Hargus and Cappelli

Meezan *et. al.* characterized the Stanford Hall Thruster (SHT) using floating emissive probes, Faraday probes ("guarded ion probe"), Langmuir probes and laser-induced fluorescence velocimetry. With data from these probes Meezan was able to calculate an effective Hall parameter in the discharge channel of the SHT and compare this value to the one predicted from Yoshikawa's expression for α_B – the diffusion coefficient α_B is inversely proportional to the effective Hall parameter. While noting the large error bars in the estimate of the effective Hall parameter, over a large range of the discharge channel the value predicted from Yoshikawa's theory was in excellent agreement with the data.